Computational physics of relativistic laser-matter interaction

Inaugural-Dissertation

zur

Erlangung des Doktorgrades der
Mathematisch-Naturwissenschaftlichen Fakultät
der Heinrich-Heine-Universität Düsseldorf

vorgelegt von

Sergey Kiselev
aus Kovrov

Düsseldorf
2005

Gedrukt mit der Genehmigung der Mathematisch-Naturwissenschaftlichen
Fakultät der Heinrich-Heine-Universität Düsseldorf

Referent:	Prof. Dr. A. Pukhov, Düsseldorf
Korreferent:	Prof. Dr. Oswald Willi, Düsseldorf

Tag der mündlichen Prüfung: 20 Juni 2005

Computational physics
of relativistic laser-matter interaction

Sergey Kiselev

Dissertation for the degree of Doctor in Philosophy
at the University of Duesseldorf, Germany

Duesseldorf
2005

Printed with permission of the Faculty of Mathematics and Natural Sciences of Heinhrich-Heine University of Duesseldorf

Referee:	Prof. Dr. A. Pukhov
Co-referee:	Prof. Dr. Oswald Willi

The day of public defence: 20 June 2005

Contents

To my Grandmother,
who passed away on December 31, 2003.

Chapter 1

Introduction

Ever since the invention of a microscope, one of the greatest trends of modern science has been toward resolving ever-finer detail in the study of matter. Since small objects generally move quickly (which simply follows from the dependence of inertia on mass), high spatial resolution alone is not sufficient to image such objects (for example, to take a magnified photograph of them with a camera). A short-duration flash of light (or fast shutter) is also necessary to prevent blurring of the image. While the millisecond duration of an ordinary camera is sufficient to freeze the action of a person running (meter-scale length), a strobe light with ultrashort pulse duration (1 femtosecond or 10^{-15} s) is required in order to resolve a moving atom (10^{-10}-m-scale length).

For this reason, the study of ultrafast molecular dynamics did not begin until the development of femtosecond-duration optical lasers in the late 1970s. However, direct time-domain measurements with femtosecond temporal resolution could be made only with micrometer-scale spatial resolution because of the relatively long wavelength ($\sim$ 1 micrometer) of optical light. Alternatively, direct measurements with atomic-scale spatial resolution could be made with x-rays from synchrotrons, but with only nanosecond temporal resolution, because of the relatively long duration of these sources. Now, with the development of a new generation of tabletop-size laser systems, it is feasible to generate femtosecond-duration x-ray pulses [Kiselev et al., 2004, Rousse et al., 2004], which will allow high resolution to be achieved simultaneously in both space and time.

1.1 Laser-driven x-ray sources

What makes lasers so promising is that they can deliver both short pulses and high peak power. Because power is energy divided by time, when only a joule of energy is released over femtoseconds, it can produce a terawatt of power. This power can produce the highest light intensities on Earth, 10^{21} W/cm^2, by focusing the light to a spot size of the laser wavelength. The largest electric and magnetic fields ever produced of the order of 10^{12} V/cm and 10^5 tesla (10^9 gauss), respectively are associated with these extreme power densities. What permits solid-state lasers to generate fields of that order is the chirped-pulse-amplification technique, invented in 1987. In order to prevent damage to the amplifiers, the laser light is first stretched in time, then amplified as a pulse with long duration, and thus with lower power, and finally compressed to a short duration after the energy has been increased. Fields of this high strength can accelerate electrons to relativistic energies, which can be used to convert light to short pulses of x-rays.

1.1.1 Electron motion in laser fields

Light is a wave with transverse electric and magnetic fields oscillating at the same frequency. At low laser power, electrons oscillate along the light's electric field $\mathbf{E}$ with a velocity $\mathbf{v}$ which is always very small compared to the speed of light (Fig. 1.1a). This motion is described by the equation

$$\frac{d\mathbf{p}}{dt} = -e\mathbf{E},$$

where m is the electron mass and e is the magnitude of its charge. At higher laser intensities, the electron velocity in a laser focus can approach close the speed of light c and relativistic mass m increases. In this relativistic regime, one must also include an additional term in the equation of motion, which then becomes

$$\frac{d\mathbf{p}}{dt} = -e[\mathbf{E} + (\mathbf{v}/c) \times \mathbf{B}].$$

Thus, the light's magnetic field **B** will act to bend the electrons in the direction of light propagation, perpendicular to both **E** and **B** (Fig. 1.1b). Due to the magnetic force, the electron traces a figure-8, oscillating twice in the direction of the light wave for every single oscillation along the polarization direction (along **E**). This oscillating motion is then superimposed upon a steady drift in the direction of the light wave. Thus the motion is increasingly longitudinal as the light intensity is increased.

1.1.2 Laser focusing on solid targets

One way to make x-rays is by focusing an intense laser onto a solid target. When the relativistic electrons collide with the ions of the solid, they rapidly accelerate, causing the emission of bremsstrahlung radiation in the x-ray spectral region. This is just like a conventional x-ray tube, such as found in a dentist's office, except it is the laser's short-duration electromagnetic field that accelerates the electrons instead of the continuous electrostatic field between the anode and cathode of the x-ray tube. One of the problems with these x-rays is that they are produced in all directions simultaneously (4π steradians), and so their intensity decreases with the square of the distance from the source. They are also incoherent and deliver relatively long pulses, picoseconds in duration. However, because of the simplicity of the method used to produce them, these x-rays have been used to study picoseconds processes such as shock formation or melting by means of either x-ray absorption or diffraction.

1.1.3 Laser focusing on gaseous targets

Another way to make x-rays is to focus an intense laser onto a gaseous-density target. The highly nonlinear but periodic motion discussed above

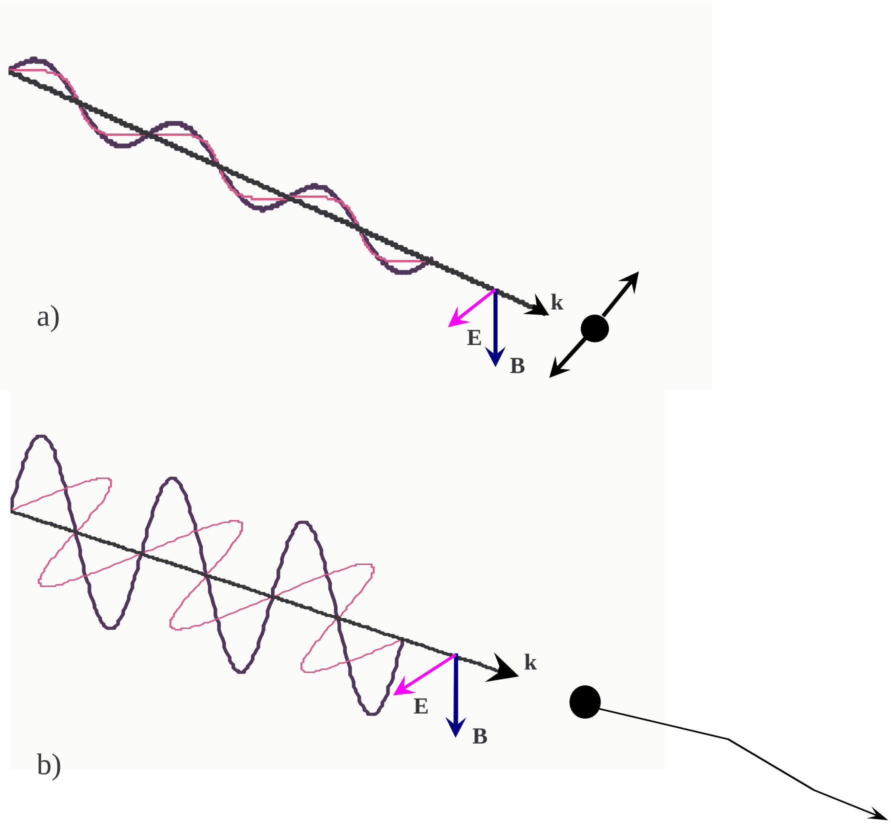

Figure 1.1: Motion of an electron in a light wave. (a) In classical optics, the amplitude of the light wave is small, electrons oscillate in the direction of the electric field **E**, at the light's frequency, and there is no displacement along the light's propagation direction **k**. Only the electric field acts on the electron, and the electron-oscillation velocity is very small compared with the speed of light. (b) In relativistic optics, the amplitude of the light wave is very large, the light's magnetic field becomes important, and the combined action of the electric and magnetic fields pushes the electron forward. In this case, the electron velocity becomes close to the speed of light.

results in nonlinear scattering. For instance, when the strength of the light field approaches the Coulomb field binding electrons to nuclei, extremely high order harmonics can be observed, culminating in the recent observation of the 501st harmonic of 800-nanometer laser light. The mechanism responsible for this is recombination of the energetic e^-. At larger light field strengths, the atoms become ionized, producing plasma, which disrupts phase matching and prevents the efficient generation of higher harmonics. In even larger fields, the electron will no longer even collide with the nucleus due to acceleration in the direction of the light wave. But when the field is increased yet further, the free electrons in the plasma begin to oscillate with relativistic velocities, and the nonlinear motion (discussed above) can produce harmonics. The usefulness of this nonlinearly Thomson scattered light, however, is limited, owing to the fact that the harmonics are scattered at large angles. Also, because the oscillation frequency is reduced, so too is the scattering efficiency into high harmonics.

Fortunately, at high laser intensities a directed beam of relativistic electrons is also produced in the direction of the laser light by laser-driven plasma waves. Lasers have been shown to accelerate greater than 10^{10} electrons to energies well above 1 MeV in low-divergence ($< 10^\circ$ angle) beams at repetition rates of 10 Hz. The acceleration gradient is greater than 1 GeV/cm, 104 times greater than that of conventional radio-frequency accelerators. Recent experiments have shown that Compton scattering by such a co-propagating electron beam produces a collimated beam of high-order harmonics, also in the direction of the laser light (Fig. 1.2). Unlike Thomson scattering from low-velocity electrons, which produces only harmonics, Compton scattering from relativistic electron beams also results in a Doppler shift, which (in the case of counterpropagating beams) can further upshift the energy of the scattered light to the hard x-ray region of the spectrum. For example, electrons with only 100 MeV energy can boost a 1 eV energy photon to 50 keV. This opens up the possibility of an all-optically-driven "tabletop" hard x-ray source, which is of interest not only as a probe

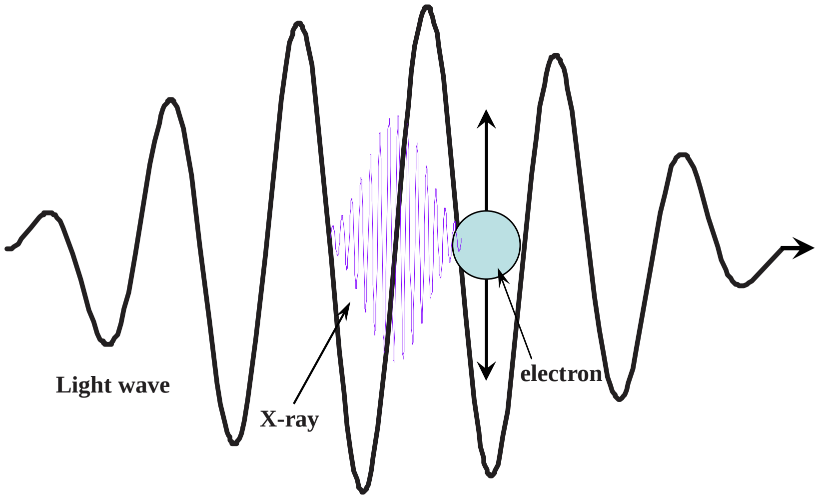

Figure 1.2: Process whereby harmonic generation and a relativistic Doppler effect can upshift the frequency of visible radiation from a laser that Compton-scatters from an energetic electron beam to the x-ray region of the spectrum. Colliding a laser with 100-MeV-energy electron beams from a tabletop laser accelerator can produce 50-keV x-rays.

with atomic-scale spatial resolution but also as a medical diagnostic tool because of the large penetration of such energetic light through matter.

1.1.4 Other x-ray sources

There exist other means to generate x-ray sources, such as synchrotrons and free-electron lasers. They rely on conventional (radio-frequency) accelerators to generate an electron beam, but because of their low field gradients (0.1 MeV/cm) they are usually quite large (tens to hundreds of meters in length). Long sets of magnets (tens of meters) are required to wiggle the electrons. Laser-Compton sources, by contrast, accelerate electrons in millimeter distances, and the electrons are wiggled in a millimeter-long interaction region by the magnetic field of the laser pulse. Consequently, laser-Compton sources will be much more affordable, thus potentially permitting their operation at university, industrial, and hospital laboratories. They also provide better temporal resolution (femtoseconds instead of tens of picoseconds). There are proposals to build a short-pulse x-ray free-electron laser, but this will require a 50-GeV-energy electron beam conventionally accelerated in a 3-km-long (2-mi) tunnel to be passed through a 50-m-long (150-ft) set of wiggler magnets. Free-electron lasers do have the advantage over Compton sources that the electrons become tightly bunched, improving coherence and x-ray power.

Another laser-driven x-ray source is an x-ray laser, which is driven by electronic transitions in highly stripped ions. X-rays lasers do have the best coherence properties and are currently the brightest monochromatic sources in the extreme-ultraviolet region of the spectrum, but they do not scale to the hard x-ray regime. Although they produce shorter pulses than synchrotrons, their pulses, several picoseconds in duration, are still relatively long compared with laser- Compton sources.

1.2 Electron acceleration

One of the promising schemes is the high-gradient laser wake field acceleration (LWFA) of charged particles in plasmas [Esarey et al., 1996]. Hereinafter we consider this scheme. When a laser pulse propagates through underdense plasma, it excites a running plasma wave oscillating with the frequency

$$\omega_p/\sqrt{\gamma}, \tag{1.1}$$

where

$$\omega_p = \left(4\pi e^2 n_0/m\right)^{1/2} \tag{1.2}$$

is the nonrelativistic electron plasma frequency, e, m, and n_0 denote charge, mass, and density of electrons, respectively; γ is the average electron relativistic factor. The wave trails the laser pulse with phase velocity set by the laser pulse group velocity

$$v_{ph}^{wake} = v_0 \simeq c[1 - \omega_p^2/(2\gamma\omega^2)], \tag{1.3}$$

where ω is the laser frequency. A relativistic electron can ride this plasma wave, staying in-phase with the longitudinal electric field and be accelerated to high energies [Pukhov et al., 2003].

The laser pulse can excite the plasma wave in different ways [Pukhov, 2003]. The excitation is most efficient when the laser pulse duration is of the order of the plasma wavelength

$$\lambda_p = 2\pi\sqrt{\gamma}c/\omega_p. \tag{1.4}$$

Taking a plane laser pulse with the normalized intensity profile

$$a^2 = a_0^2 \cos^2 \pi\zeta/2L \tag{1.5}$$

for

$$-L < \zeta = z - ct < L, \tag{1.6}$$

one finds that the wake field reaches the maximum

$$E_{\max}/E_0 = a_0^2/(2 + 2a_0^2), \tag{1.7}$$

when the laser pulse full width at half maximum (FWHM) is

$$L = \lambda_p/2 \tag{1.8}$$

[Esarey et al., 1996]. Here

$$E_0 = mc\omega_p/e \tag{1.9}$$

normalizes the electric field of the plasma wave, and

$$a_0 = eA_0/mc^2 \tag{1.10}$$

is the dimensionless amplitude of the laser vector potential. The pattern of wake field excitation differs significantly for laser pulses longer and shorter than the plasma period. The long laser pulse gets self-modulated with the plasma period, and the resonance between this self modulation and the plasma frequency leads to an efficient wake field excitation. The corresponding regime is called self-modulated laser wake field acceleration

(SM-LWFA) [Andreev et al., 1992]. Long laser pulses, however, experience not only the one-dimensional self-modulation, but get self-focused and form relativistic channels in the plasma [Pukhov and Meyer-ter-Vehn, 1996, Pukhov et al., 1999]. Trapping of electrons in the plasma waves is a key issue for LWFA. Injection and acceleration of external beams has been demonstrated experimentally [Amiranoff et al., 1998b]. Creation of trapped electrons inside the wave bucket has been proposed with the application of supplementary laser pulses [Esarey et al., 1997, Umstadter et al., 1996b]. The wavebreaking can also lead to self-trapping and acceleration of electrons by the plasma wave [Malka et al., 2002, Modena et al., 1995, Santala et al., 2001].

1.2.1 Applications

Laser-driven ultrafast x-rays can provide the required temporal resolution for the study of ultrafast processes such as conformational changes in ultrafast biology and chemistry, innershell electronic processes in atomic systems, and phase transitions in materials science. One problem they might help solve is the determination of protein structure. They are also useful in the study of photo-initiated processes, such as photosynthesis, because in this case the optical pump and x-ray probe are absolutely synchronized with each other, being derived from the same laser. Also, significant absorption of the x-ray probe pulse (such as occurs in the in vitro imaging of live biological cells) can destroy a sample or at least cause it to move. Thus, in order to acquire an image before the occurrence of blurring from this heat-induced motion, a single-shot pump-probe measurement with ultrashort-duration and high-peak-power x-rays is required. Low-repetition-rate, laser-produced x-ray sources are also best suited for studies of processes that are irreversible, and in which the sample must be moved between shots. Tunable x-rays that have energy near 50 keV can also be used in medicine for applications such as either differential absorption or phase-contrast imaging.

Chapter 2

Electron Acceleration in the "Bubble" Regime

2.1 Phenomenological theory and 3D PIC simulation of laser-plasma interaction in the "bubble" regime

2.1.1 Introduction

Here, we focus on laser-plasma interaction in the "bubble" regime recently proposed by [Pukhov and Meyer-ter-Vehn, 2002]. It has been observed in 3D Particle-In-Cell (PIC) simulations for ultra-relativistically intense laser pulses shorter than λ_p (1.4). These laser pulses are intense enough to break the plasma wave already after the first oscillation. The main features of the "bubble" regime are the following:

(i) a cavity free from cold plasma electrons is formed behind the laser pulse instead of a periodic plasma wave,

(ii) a dense bunch of relativistic electrons with a monoenergetic spectrum is self-generated,

(iii) the laser pulse propagates many Rayleigh lengths in the homogeneous plasma without a significant spreading.

These features are absent in the weakly relativistic regime of laser wake field acceleration [Esarey et al., 1996].

We discuss here numerical 3D PIC simulation of laser-plasma interaction in the “bubble” regime and develop a phenomenological theory of this regime. The electron dynamics is defined by the laser ponderomotive force and the electromagnetic fields pertinent to the “bubble” density patterns. It is seen from Fig. 2.1 that there are roughly three patterns:

(i) the electron plasma cavity with the large ion charge,

(ii) the electron sheath around the cavity forming the “bubble” boundary,

(iii) the bunch of accelerated electrons growing behind the laser pulse in the cavity.

The density of the electron sheath peaks at the head of the laser pulse and at the base of the cavity. These density peaks are formed by the relativistic electrons with $v \simeq v_0$, where v_0 is the “bubble” velocity. The “bubble” base is the source of electrons, which get trapped and accelerated to $\gamma \gg \gamma_0$, where $\gamma_0 = (1 - v_0^2/c^2)^{-1/2}$ is the relativistic gamma-factor of the bubble.

2.1.2 Numerical simulation parameters

For the simulations, we use the fully electromagnetic 3D PIC code Virtual Laser-Plasma Laboratory [Pukhov, 1999]. The incident laser pulse is circularly polarized, has the Gaussian envelope

$$a(t, r) = a_0 \exp(-r_\perp^2/r_L^2 - t^2/T_L^2), \tag{2.1}$$

The parameters of the laser pulse are

$$\begin{aligned} \lambda &= 0.82\mu m & \qquad r_L &= 10\lambda \\ cT_L &= 4\lambda & \qquad a_0 &= 10. \end{aligned} \tag{2.2}$$

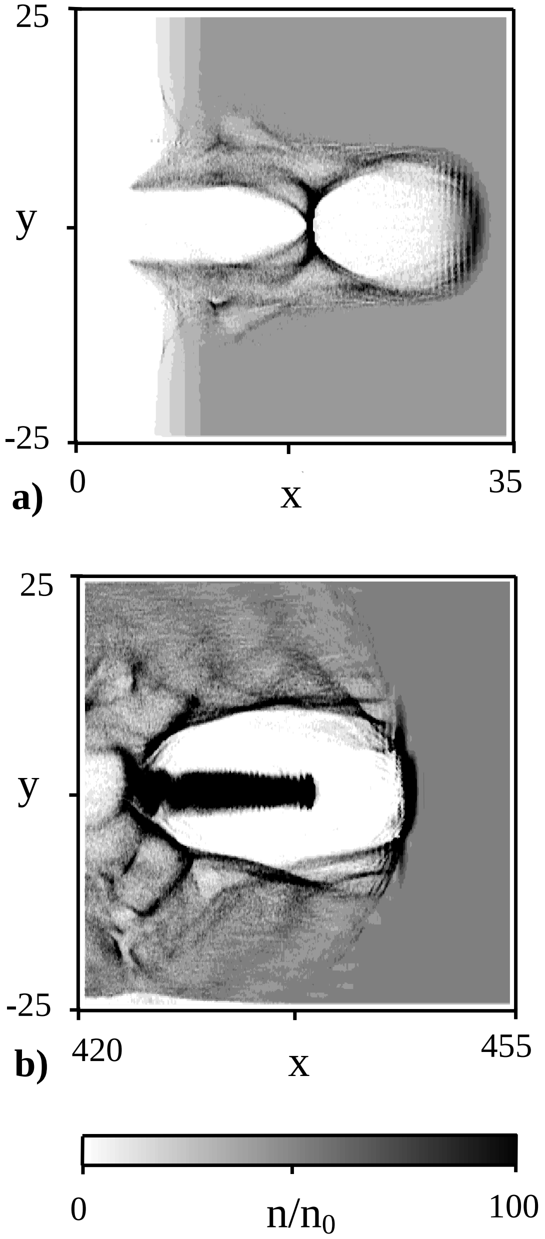

Figure 2.1: On-axis cuts of the electron density n in the $x-y$ plane from the PIC simulation at the times when the laser pulse passed about (a) $l_{int} = 25c/\omega_p \simeq 50\lambda$ and (b) $l_{int} = 442c/\omega_p \simeq 900\lambda$, where λ is a laser wavelength. The coordinates are given in c/ω_p.

The pulse propagates in a plasma with the density $n_0 = 6.1 \times 10^{-3} n_c$, where

$$n_c = \left(m\omega^2/4\pi e^2\right)^{1/2} \tag{2.3}$$

is the critical density.

The plasma density distribution observed in the simulation is shown in Fig. 2.1 at two instants of time:

(a) when the laser pulse has passed $l_{int} = 25c/\omega_p \simeq 50\lambda$

(b) $l_{int} = 442c/\omega_p \simeq 900\lambda$

in plasma. These density distributions are very typical for the "bubble" regime. It is seen from Fig. 2.1 that the wake behind the laser pulse takes the form of a solitary cavity, which is free from plasma electrons. The cavity is surrounded by a high density sheath of the compressed electron fluid. At later times, Fig. 2.1(b), a beam of accelerated electrons grows from the "bubble" base. Simultaneously, the "bubble" size increases.

2.1.3 Fields inside relativistic cavern

Before considering the relativistic cavity moving in plasma we summarize the results for fields within an ionic sphere either at rest, or relativistically moving. The electromagnetic field of the uniformly charged sphere at rest is purely electrostatic. The electric field and the scalar potential inside the sphere with radius R and with the charge density $|e|n_0$ are [Landau and Lifshits, 1982]

$$\mathbf{E} = \frac{\mathbf{r}}{3}, \quad \mathbf{B} = 0, \quad \varphi = 1 + \frac{R^2}{6} - \frac{r^2}{6}, \tag{2.4}$$

where we choose that the potential is equal to unity at the sphere boundary. We use dimensionless units, normalizing the time to ω_p^{-1}, the lengths to c/ω_p, the velocity to c, the electromagnetic fields to $mc\omega_p/|e|$, and the electron density, n, to the background density n_0.

If the ionic sphere runs with the relativistic velocity $v_0 \simeq 1$ along x-axis then the fields inside the sphere are

$$E_x = 0, \quad E_y = B_z = \frac{y}{2}, \tag{2.5}$$

$$B_x = 0, \quad E_z = -B_y = \frac{z}{2}, \tag{2.6}$$

where the terms, which are proportional to $\gamma_0^{-2} = 1 - v_0^2 \ll 1$, are neglected. The Lorentz force on the relativistic electron moving inside the sphere with velocity $\mathbf{v} = -\mathbf{v}_0 = -\mathbf{e}_x$ is

$$F_x = 0, \quad F_y = -E_y - B_z = -y, \tag{2.7}$$

$$F_z = -E_z + B_y = -z, \tag{2.8}$$

while it is negligible for the electron with $\mathbf{v} = \mathbf{v}_0 = \mathbf{e}_x$ because of relativistic compensation of the electrostatic force by the self-magnetic force [Davidson, 2001].

Now we are interested in the question what are the fields inside a spherical electron cavity moving in plasma. This cavity is similar to the hole in semiconductor physics [Smith, 1959]. Contrary to the case discussed above, the ions are now immobile in the cavity while the cavity runs with the relativistic velocity $v_0 \simeq 1$ along x-axis. The ion dynamics is neglected because the cavity radius is assumed to be smaller than the ion response length $\simeq c/\omega_{pi}$, where $\omega_{pi} = (4\pi e^2 n_0/M)$ is the ion plasma frequency and M is the ion mass. To calculate the fields we rewrite the Maxwell equations in terms of potentials using the following convenient gauge

$$A_x = -\varphi. \tag{2.9}$$

We get

$$\begin{aligned}\triangle\Phi &= 1 - n\left(1 - \frac{p_x}{\gamma}\right) + \left(\frac{\partial}{\partial t} + \frac{\partial}{\partial x}\right)(\nabla \cdot \mathbf{A}) \\ &+ \frac{1}{2}\frac{\partial}{\partial t}\left(\frac{\partial}{\partial t} - \frac{\partial}{\partial x}\right)\Phi,\end{aligned} \tag{2.10}$$

$$\nabla \times \nabla \times \mathbf{A} + n\frac{\mathbf{p}}{\gamma} + \frac{\partial}{\partial t}\left(\frac{\partial \mathbf{A}}{\partial t} - \frac{\nabla \Phi}{2}\right) = 0. \tag{2.11}$$

Here we use the wake field potential $\Phi = A_x - \varphi$ instead of the scalar one, n is the electron density and $\mathbf{p}$ is the electron momentum.

Then we use a quasistatic approximation assuming that all quantities depend on $\zeta = x - v_0 t$ instead of x and t. The Maxwell equations reduce to the form

$$\triangle \Phi = \frac{3}{2}(1-n) + n\frac{p_x}{\gamma} - \frac{1}{2}\frac{\partial}{\partial \xi}\left(\nabla_\perp \cdot \mathbf{A}_\perp\right) \tag{2.12}$$

$$\triangle_\perp \mathbf{A}_\perp - \nabla_\perp\left(\nabla_\perp \cdot \mathbf{A}_\perp\right) = n\frac{\mathbf{p}_\perp}{\gamma} + \frac{1}{2}\nabla_\perp \frac{\partial \Phi}{\partial \xi}, \tag{2.13}$$

where the terms proportional to $\gamma_0^{-2} \ll 1$, are neglected. Inside the cavity $(n = 0)$ we get

$$\triangle \Phi = \frac{3}{2} - \frac{1}{2}\frac{\partial}{\partial \xi}\left(\nabla_\perp \cdot \mathbf{A}_\perp\right), \tag{2.14}$$

$$\triangle_\perp \mathbf{A}_\perp - \nabla_\perp\left(\nabla_\perp \cdot \mathbf{A}_\perp\right) = \frac{1}{2}\nabla_\perp \frac{\partial \Phi}{\partial \xi}. \tag{2.15}$$

The solution of Eqs. (2.14) and (2.15) with spherical symmetry is

$$\Phi = 1 - \frac{R^2}{4} + \frac{r^2}{4}, \quad A_x = -\varphi = \frac{\Phi}{2}, \quad \mathbf{A}_\perp = 0, \tag{2.16}$$

where R is the radius of the cavity, $r^2 = \xi^2 + y^2 + z^2$, and the constant of integration is chosen so that $\Phi(R) = 1$.

The electromagnetic fields inside the relativistic cavity are

$$\begin{aligned} E_x &= \xi/2, \quad E_y = -B_z = y/4, \\ B_x &= 0 \quad E_z = B_y = z/4. \end{aligned} \tag{2.17}$$

The calculated distribution of electromagnetic fields is close to the one observed in the 3D PIC simulation (see Fig. 2.2). The small deviation from the analytically calculated field distribution is because the cavity shape is not exactly a sphere. It is easy to see that the fields (2.16) satisfy the Maxwell equations.

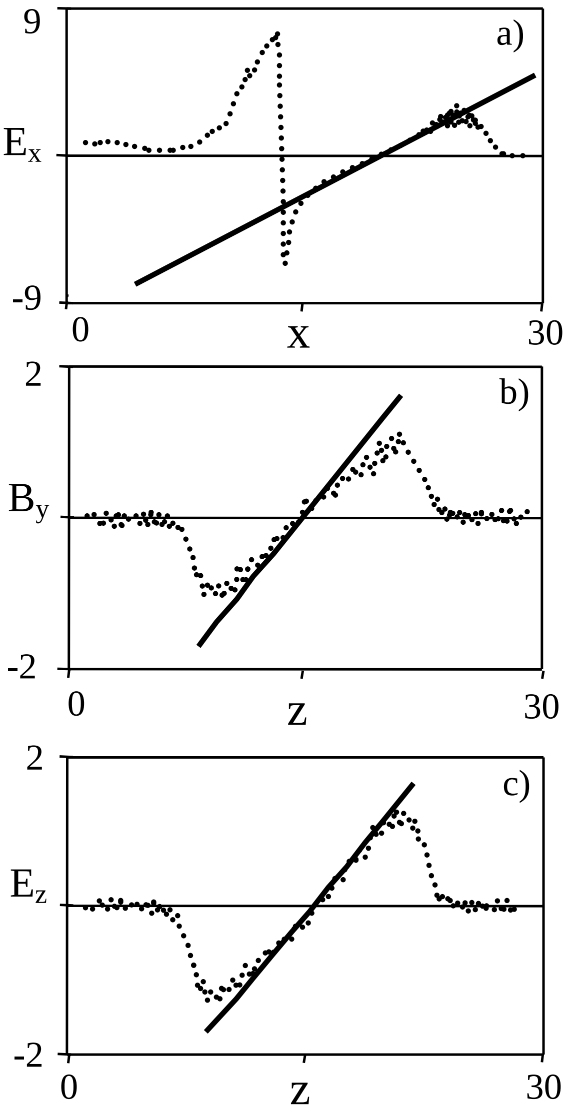

Figure 2.2: Space distribution of the electromagnetic fields normalized to $mc\omega_p/|e|$ at the time instance when the laser pulse has passed $25c/\omega_p$: (a) E_x as a function of x; (b) B_y as a function of z; (c) E_z as a function of z. The PIC simulation results are shown by dashed lines while the analytical results are shown by solid lines. The coordinates are given in c/ω_p.

The Lorentz force acting on a relativistic electron with $v_x = 1$ inside the cavity is

$$F_x = -\frac{\partial \Phi}{\partial \xi} = -E_x = -\frac{\xi}{2}, \tag{2.18}$$

$$F_y = -\frac{\partial \Phi}{\partial y} = -E_y + B_z = -\frac{y}{2}, \tag{2.19}$$

$$F_z = -\frac{\partial \Phi}{\partial z} = -E_z - B_y = -\frac{z}{2}. \tag{2.20}$$

The wake potential, Φ, can be considered as the potential of the Lorentz force on the electron with $v_x = 1$. The Lorentz force peaks for the electron with $v_x = v_0 = 1$ while it is zero for the electron with $v_x = -1$ because of the relativistic compensation of the electrostatic force by the self-magnetic force. Notice that this effect is opposite to that of the relativistically moving ionic sphere. This is because the displacement current in the cavity is opposite to the ion current in the relativistically moving ion sphere.

2.1.4 Shape of the “bubble”

In this section we discuss the cavity shape. It is seen from Fig. 2.1 that the “bubble” and the electron bunch inside the cavity grow with time. At the beginning of the interaction there is no bunch yet and the cavity shape is determined only by ponderomotive potential of the laser pulse. The transverse size of the cavity reaches a maximum near the middle plane, which passes through the cavity center. At the positions, where this plane cuts the boundary of the “bubble”, the electron sheath contains a return current carried by weakly relativistic electrons. These electrons feel the Lorentz force (2.17) which is nearly balanced by the laser ponderomotive force. The transverse radius R of the cavity can thus be estimated from the equation

$$\frac{R}{4}(1 - v_x) \simeq \frac{R}{4} \simeq F_{pond} \simeq \frac{\partial}{\partial R}\sqrt{1 + a^2(R)}, \tag{2.21}$$

where the spherical symmetry for the ion cavity is assumed. The ponderomotive force is written for a laser pulse which is spherical and circularly polarized [Quesnel and Mora, 1998]. The electron kinetic energy is neglected as compared with the ponderomotive potential. For the laser-plasma parameters used in our 3D PIC simulation (Sec. 2.1.2) we find from Eq. (2.21) $R \simeq 6$ that is close to the "bubble" radius observed in the simulation (see Fig. 2.1a).

When the force from the bunch becomes stronger than the ponderomotive one, then the cavity shape is determined by the bunch. Because the bunch density n_b is much higher than the plasma density, we can refer to the theory of relativistic electron beam in plasma in the ion-focused regime [Whittum, 1992] and use it to estimate the "bubble" transverse radius. The equilibrium at the interface near the middle plain is provided by the balance between the Lorentz forces from the cavity (2.16) and from the bunch electrons. The transverse radius of the cavity in this bunch dominated regime is

$$r_b\sqrt{n_b} < R < r_b\sqrt{2n_b}, \tag{2.22}$$

where the lower limit corresponds to a bunch with the weak current $n_b\pi r_b^2 \ll 1$, while the upper limit occurs for the strong current $n_b\pi r_b^2 \gg 1$. Plasma electrons flow along the interface in the direction, which is opposite to the laser pulse propagation and form the return current sheath. If the bunch current is weak, then the width of the return current sheath is about c/ω_p and the electron energy in the return current sheath is small $\gamma \simeq 1$. In the opposite limit, $n_b\pi r_b^2 \gg 1$, the sheath electrons gain relativistic energies, $\gamma > 1$, and the sheath width increases, $\sim \sqrt{\gamma}c/\omega_p$. For $r_b \simeq 2$ and $n_b \simeq 10$ observed in the simulation at $l_{int} = 442$ the bunch current is strong and the cavity radius is defined by upper limit of the inequality 2.22). Using Eq. (2.21) we get $R \simeq 9$ that is close to the value observed in the simulation (see Fig. 2.1b). The length of the cavity is of the order of R at the beginning of interaction. When the bunch becomes large, then the cavity strongly elongates and its length is determined by the bunch.

2.1.5 Electron trapping by the “bubble”

We assume that the laser field is circularly polarized and the azimuthal motion of plasma electrons is neglected. For simplicity we assume that the electron trajectory lies in the plane $z = 0$. The group velocity of the laser pulse, v_0, is assumed to be close to the speed of light so that $\gamma_0^{-2} = 1 - v_0^2 \ll 1$. The laser pulse propagates along the x-axis. The averaged motion of an electron in the laser field and in the slowly varying electromagnetic fields of the “bubble” is defined by the averaged Hamiltonian [Bauer et al., 1995, Quesnel and Mora, 1998, Dodin and Fisch, 2003]

$$H = \sqrt{1 + (\mathbf{P} + \mathbf{A})^2 + a^2} - \varphi, \tag{2.23}$$

where $\mathbf{P}$ is the canonical momentum of the electron, a is the vector potential of the laser field, $\mathbf{A}$ and φ are the slowly varying vector and scalar potentials, respectively. In this description the fast electron oscillations in the laser field are averaged out and only the ponderomotive force remains.

We change variables in the Hamiltonian (2.23) from x and P_x to $\xi = x - v_0 t$ and $P_\xi = P_x$ by a canonical transformation with the generating function $S = (x - v_0 t)P_\xi$. The Hamiltonian in the new variables takes the form

$$\begin{aligned} H &= \gamma - v_0 P_x - \varphi \\ &= \sqrt{1 + (\mathbf{P} + \mathbf{A})^2 + a^2} - v_0 P_x - \varphi. \end{aligned} \tag{2.24}$$

The Hamilton equations of motion are given by

$$\frac{dP_x}{dt} = -v_x \frac{\partial A_x}{\partial \xi} - v_y \frac{\partial A_y}{\partial \xi} + \frac{\partial \varphi}{\partial \xi}, \tag{2.25}$$

$$\frac{dP_y}{dt} = -v_x \frac{\partial A_x}{\partial y} - v_y \frac{\partial A_y}{\partial y} + \frac{\partial \varphi}{\partial y}, \tag{2.26}$$

$$\frac{d\xi}{dt} = \frac{p_x}{\gamma} - v_0 = v_x - v_0, \tag{2.27}$$

$$\frac{dy}{dt} = \frac{p_y}{\gamma} = v_y. \tag{2.28}$$

The laser pulse, the cavity and the electron sheath run with the velocity v_0. At the same time, the relativistic gamma-factor of the electron bunch is much higher: $\gamma_b \gg \gamma_0$. The potentials in the Hamiltonian (2.24) depend on the ξ and also slowly change with x and t due to the ultra-relativistic electron bunch. If we neglect the time-dependent corrections of the order of $t(v_b - v_0) \simeq t\gamma_0^{-2}/2 \ll 1$ then the Hamiltonian (2.24) is the integral of motion, where $v_b \approx 1 - 1/2\gamma_b^2$ is the bunch velocity. It follows from the 3D PIC simulations that the electron capture takes a time of the order the cavity size, during which the time-dependent corrections are negligibly small.

The necessary condition for electron trapping in the cavity is the existence of the point of return where $d\xi/dt = 0$. It follows from Eq. (2.27) that at this point

$$p_x = v_0\gamma. \tag{2.29}$$

The integral of motion (2.24) can be rewritten as follows

$$H = \gamma - v_0 p_x - \Phi = 0, \tag{2.30}$$

where the initial conditions $\mathbf{p} = \mathbf{A}_\perp = a = 0$ and $\Phi = 1$ are applied. The relations (2.29) and (2.30) can be expressed at the return point in the form

$$p_x = v_0\gamma_0\gamma_\perp = v_0\gamma_0^2\Phi, \tag{2.31}$$

where $\gamma_\perp^2 = 1 + p_y^2 + a^2$. The domain in the phase space, where the electron is trapped, can be defined as

$$p_x \geq v_0\gamma_0\gamma_\perp = v_0\gamma_0^2\Phi. \tag{2.32}$$

Eq. (2.31) gives the boundary of the domain. The trapping occurs most likely at the boundary of the domain, where the electron becomes trapped with the lowest energy. The laser field can be neglected in the trapping process, because the trapping occurs well behind the laser pulse where the laser field is small.

To obtain analytical results on the trapping, we approximate the "bubble" by a sphere. The electron sheath around the cavity screens the ion field in the surrounding plasma. We model the radial Lorentz force acting on a relativistic electron from this structure as

$$F = rS\left(r-R\right) = -\frac{r}{4}\left(\tanh\frac{r-R}{d} - 1\right), \tag{2.33}$$

where $r^2 = \xi^2 + y^2 + z^2$, R is the sphere radius and d is the width of the electron sheath. This force is close to the one observed in the 3D PIC simulation. The potential of this structure is

$$\begin{aligned}\Phi &= 1 + \frac{r^2}{4} - \frac{d^2\pi^2}{48} - \frac{1}{4} r d \ln\left(1 + \exp\frac{2r}{d}\right) \\ &\quad -\frac{1}{8}\mathrm{Li}_2\left(-\exp\frac{2r}{d}\right),\end{aligned} \tag{2.34}$$

where

$$Li_2(z) = \int_z^0 \frac{\ln(1-t)}{t} dt \tag{2.35}$$

is the dilogarithm function [Abramowitz and Stegun, 1972]. In the limit $d \to 0$ function $S\left(r\right)$ reduces to the step function and Eq. (2.34) reduces to Eq. (2.16).

It follows from Eq. (2.31) that the trapping most likely occurs on the sphere surface, where $\Phi \simeq \Phi_{\min} = 1$. The trapping condition takes the form

$$\frac{p_x}{v_0\gamma_0} = \gamma_\perp \simeq \gamma_0. \tag{2.36}$$

To be trapped the electron must be accelerated so that $p_\perp \simeq \gamma_0$ and $p_x \simeq \gamma_0^2$. Integrating numerically the Hamilton equations (2.25)-(2.28) for the potential (2.34) we find (see Fig. 2.3a) that the cavity can trap electrons, which have been initially at rest, if

$$R > \gamma_0. \tag{2.37}$$

It is seen from Fig. 2.1 that the velocity of the cavity base is smaller than that of the cavity front because the sheath electrons near the cavity base are collected by the bunch. Notice that the the PIC simulation window presented in Fig. 2.1 moves with the speed of light. The velocity of the cavity front is equal to the group velocity of the laser pulse, which corresponds to $\gamma_0 \simeq 13$.

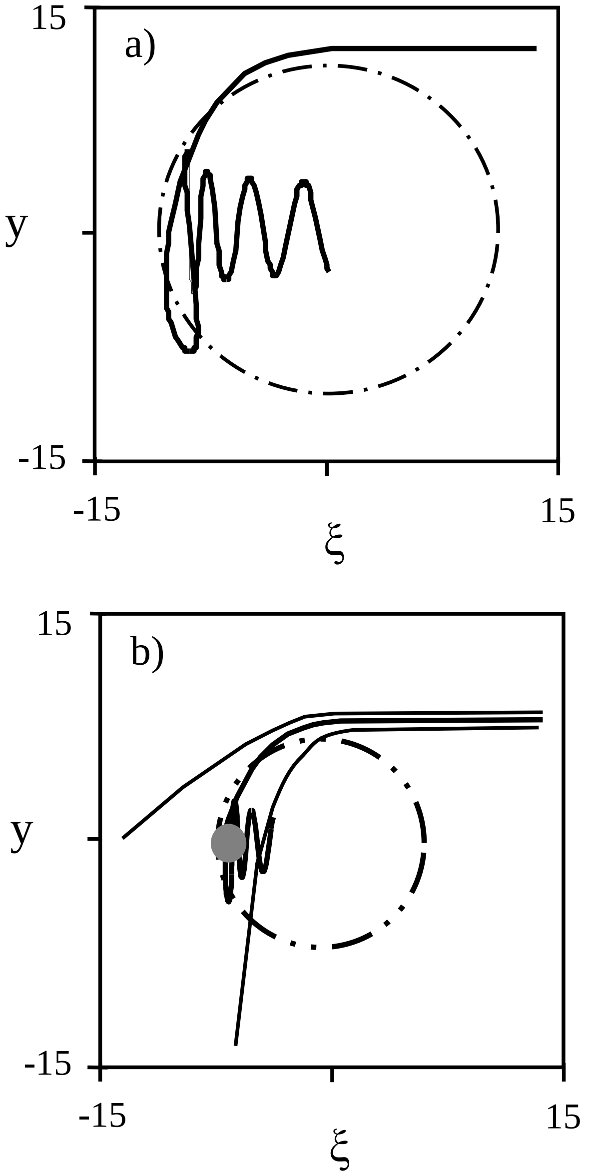

Figure 2.3: Electron trajectories in the plane $z = 0$ calculated by numerical integration of Eqs. (2.25)-(2.28) for $\gamma_0 = 9$ and potential (2.34) with $d = 0.5$ and the "bubble" radius (a) $R = 10.7$; (b) $R = 6$. The gray circle is the region where $0 < \Phi < 1$. The coordinates are given in c/ω_p.

The relativistic gamma-factor of the cavity center can be estimated from Fig. 2.1 as $\gamma_0 \simeq 9$. Hence, the cavity fields defined by the potential (2.34) with radius $R > 9$ and $\gamma_0 = 9$ can trap plasma electrons. Notice that electron, which have been initially at rest, cannot be trapped by the one-dimensional nonlinear plasma wave if $\Phi > 1$. The one-dimensional plasma wave can trap plasma electrons when wavebreaking occurs, i.e., when $\Phi_{\min} = \gamma_0^{-1} < 1$ [Esarey and Pilloff, 1995].

2.1.6 Electron trapping cross-section

We observed in the PIC simulation that at the beginning of the interaction the cavity with 40% less radius than it follows from condition (2.37) can trap the plasma electrons. The reason is that a more accurate distribution of Φ should be used to describe the electron trapping. In the previous section we use the simplified model of the "bubble" with spherically symmetric distribution of the electrons in the sheath. The wake potential in the "bubble" is also spherically symmetric in this model and is given by Eq. (2.34). However it is seen from Fig. 2.4a that the electron density in the sheath strongly peaks at the "bubble" base. The spatial distribution of Φ observed in the 3D PIC simulation at $l_{int} = 25$ is shown in Fig. 2.4. The wake potential has a minimum at the electron density peak and $0 < \Phi_{\min} < 1$. Moreover the wavebreaking occurs in this region, because $v_x > v_0$ here. Like in the one-dimensional model [Teychenne et al., 1993, Sprangle et al., 1990] the highest density is in the wavebreaking region. Because it is shown in the previous section that the electron trapping most likely occurs in the region where $\Phi \approx \Phi_{\min}$ we should describe the wavebreaking region more accurately.

To model the wavebreaking region, where $0 < \Phi < 1$, we add a potential of the Gaussian form

$$\Phi_p = \Phi_0 \exp\left[-\frac{(\xi - \xi_0)^2 + y^2 + z^2}{r_p^2}\right] \tag{2.38}$$

to the "bubble" potential (2.34). Taking $R = 7$, $\xi_0 = -6.5$, and $\Phi_0 = -1.5$ we get the minimum of the total potential $\Phi_{min} \simeq 0.25$. A numerical integration of the Hamilton equations (2.25)-(2.28) for the total potential demonstrates that electron can be trapped already by a “bubble” with the radius $R \simeq 7$ (see Fig. 2.3b).

It can be seen from Fig. 2.3 that only the electrons whose trajectories run through the wavebreaking region become trapped. Therefore only a small portion of electrons which are initially located in the electron sheath near the middle plain and whose trajectory runs through the wavebreaking region get trapped. We introduce the trajectory divergence η that is defined as follows. If initially the distance between two electrons in the sheath near the middle plain is $\delta\rho$ then it becomes $\eta\delta\rho$ in the wavebreaking region. Hence electrons in a very narrow layer with the width $D/\eta \ll c/\omega_p$ located inside the electron sheath become trapped. Then the cross-section σ for the electron trapping can be estimated as

$$\sigma \sim 2\pi R n_s \frac{D}{\eta}, \tag{2.39}$$

where n_s is the electron density in the sheath.

The bulk of the plasma electrons, which collide with the laser pulse, enter the sheath with width d. The sheath density can be estimated as the ratio between the area of the circle with radius R and that of the ring with radius R and width d

$$n_s \simeq \frac{R}{2d}, \tag{2.40}$$

where $\gamma \simeq 1$ in the sheath is assumed.

Making use of Eqs. (A.3), (2.39), (2.40) and (B.10) we finally obtain the estimates for the trapping cross-section as a function of the cavity radius:

$$\sigma \simeq \frac{\pi}{d}\left(\ln\frac{R}{2\sqrt{2}}\right)^{-1}. \tag{2.41}$$

For the cavity radius $d \simeq 2$, $R \simeq 7$ at $l_{int} = 25$ we get $\sigma \sim 1.5$, which is close to the value found in the PIC simulation $\sigma \sim 2$.

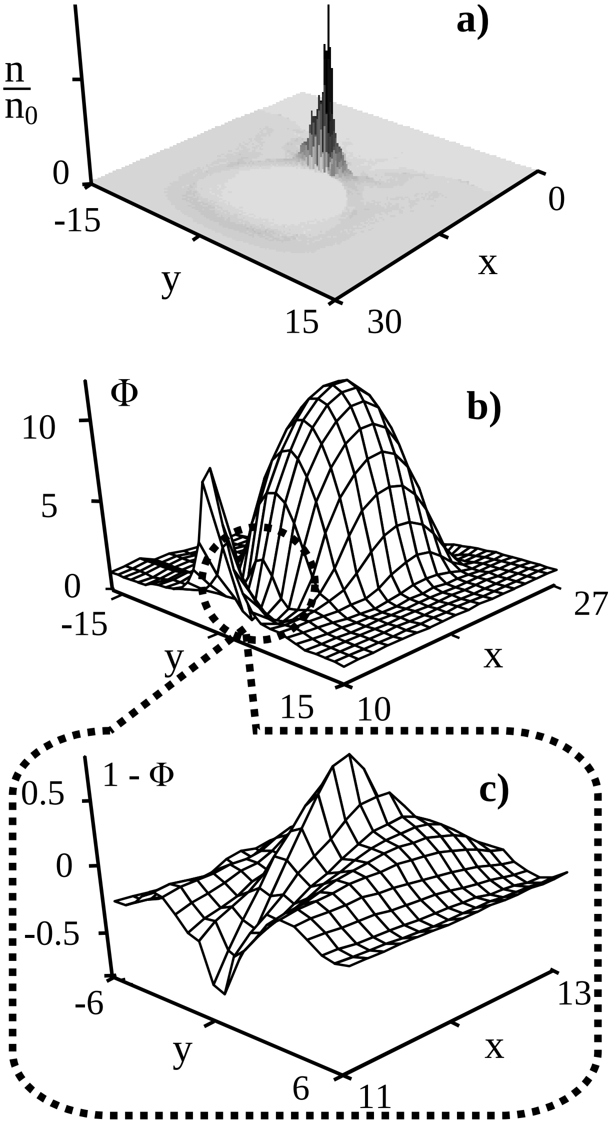

Figure 2.4: Results of the PIC simulation when the laser pulse has passed about $25c/\omega_p$. Distributions in the plane $z = 0$ of (a) potential Φ; (b) potential $1 - \Phi$ in the wavebreaking region (zoomed); (c) normalized electron density n/n_0. The coordinates are given in c/ω_p.

2.1.7 Electron acceleration

It follows from Eq. (2.31) that the energy of the trapped electron is large, $\gamma \gg \gamma_0$, and the transverse momentum is much smaller than the longitudinal one. The Hamiltonian (2.24) can be split into two parts by expanding it in powers of p_y^2. The first part determines the longitudinal motion and the second one determines the transversal motion. In the zeroth order we obtain the longitudinal Hamiltonian

$$H_{\|} = \sqrt{1+p_x^2} - v_0 p_x - \Phi \simeq 0. \tag{2.42}$$

For simplicity we assume that the cavity is an ion sphere with the radius R. Then Eq. (2.42) reduces to

$$H_{\|} \simeq \frac{p_x}{2\gamma_0^2} + \frac{\xi^2}{4} \simeq 1 + \frac{R^2}{4}. \tag{2.43}$$

The solution of the Hamilton equations is

$$\xi \propto -\frac{t}{2\gamma_0^2}, \quad p_x \propto -\frac{t^2}{4\gamma_0^2}. \tag{2.44}$$

The maximum energy of the accelerated electrons peaks at the cavity center

$$\gamma_{\max} \simeq 2\gamma_0^2 \left(1 + \frac{R^2}{4}\right) \simeq \frac{1}{2}\gamma_0^2 R^2. \tag{2.45}$$

For $\gamma_0 \simeq 9$ and $R \simeq 7$ we obtain that $\gamma_{\max} \simeq 2 \times 10^3$ that is about two times larger than $\gamma_{\max}$ observed in the PIC simulation. The difference is caused by the cavity growth and elongation (see Fig. 2.1). As the cavity elongates the potential maximum shifts down to the bunch head. The maximum energy of electrons in the bunch head reduces, because the potential difference between the bunch head and the cavity center decreases.

The transversal part of the Hamiltonian can be obtained by retaining the first order expansion terms in the Hamiltonian (2.24):

$$H_{\perp} = \frac{p_y^2}{2p_x} + \frac{y^2}{4}. \tag{2.46}$$

The Hamilton equations of motion can be then rewritten as

$$\frac{d^2 p_y}{d\xi^2} + p_y \frac{4\gamma_0^2}{r_b^2 - \xi^2} = 0. \tag{2.47}$$

Here we have used Eqs. (2.43) and (2.44). Equation (2.47) describes the transversal betatron oscillations of relativistic electrons in the bunch. Its solution can be expressed in terms of Hypergeometric functions [Abramowitz and Stegun, 1972]. However, we use the Wentzel-Kramers-Brillouin (WKB) method [Lifshitz and Landau, 1981] to find an approximate solution. Eq. (2.47) is the oscillator equation with the betatron frequency

$$\Omega(\xi) = \frac{1}{\sqrt{2p_x}} = \frac{2\gamma_0}{\sqrt{r_b^2 - \xi^2}}. \tag{2.48}$$

Since the betatron frequency $\Omega(\xi)$ is a slowly varying function,

$$\Omega^{-2} d\Omega/d\xi \simeq (2\gamma_0)^{-1} \ll 1, \tag{2.49}$$

there exists the adiabatic invariance that is the conservation of the area enclosed in the transverse phase space

$$I = \oint p_y dy = H_\perp/\Omega = const. \tag{2.50}$$

This allows us to use the WKB approximation:

$$p_y \simeq \frac{I}{\sqrt{\Omega(\xi)}} \cos\left[\int \Omega(\xi) d\xi\right], \tag{2.51}$$

$$y \simeq I\sqrt{\Omega(\xi)} \sin\left[\int \Omega(\xi) d\xi\right]. \tag{2.52}$$

It follows from Eqs. (2.51) and (2.52) that the amplitude of the transverse momentum increases and the amplitude of betatron oscillation decreases as the electron approaches the cavity center. It is seen from Fig. 2.1b that the bunch gets tightly focused toward the cavity center.

Making use of $\sqrt{1 + p_x^2 + a^2}$ instead of p_x in Eq. (2.48) we can estimate the bunch radius r_b:

$$r_b \simeq R\sqrt{\frac{\Omega}{\Omega_0}} \simeq R\left(\frac{a_0}{p_x}\right)^{1/4} \simeq \left(\frac{2a_0 R^2}{\gamma_0^2}\right)^{1/4}. \tag{2.53}$$

Having the expression for the electron trapping cross-section (2.41), one can estimate the electron bunch density. By definition of σ, all electrons entering the cross-section σ with velocity $v_0 \simeq 1$ in the frame of the cavity, become trapped. The trapped electrons form the bunch, which moves with the velocity $v \simeq 1/(2\gamma_0^2)$ in the cavity frame, as it follows from Eq. (2.44). Then the bunch density n_b can be estimated to be

$$n_b \simeq \frac{2\sigma\gamma_0^2}{\pi r_b^2}. \tag{2.54}$$

Taking $\gamma_0 \simeq 9$ and $R \simeq 7$ one find $r_b \simeq 1.9$ and $n_b \simeq 21$ that is in a fairly good agreement with the 3D PIC simulation results: $r_b \simeq 2$ and $n_b \simeq 10$.

2.2 Comparison with an experiment

2.2.1 The Laboratoire d'Optique Appliquée (LOA) experiment

The experiment was done by J. Faure, J.-P. Rousseau, and V. Malka. The generation of intense accelerating fields in plasmas has been demonstrated in many experiments [Kitagawa et al., 1992, Clayton et al., 1985, Amiranoff et al., 1992]. Proof-of-principle experiments have shown the feasibility of externally injecting electrons from a conventional accelerator into the laser-driven plasma accelerating structure [Kitagawa et al., 1992, Everett et al., 1994, Amiranoff et al., 1998a]. However, the output beam quality has been poor: the electron energy distribution has had a 100% energy spread. Until now, the most widespread method for producing electron beams from plasmas has relied on the self-modulated laser wakefield accelerator [Andreev et al., 1992, Sprangle et al., 1992, Antonsen and Mora, 1992]. Under the influence of the selfmodulation instability, its envelope modulates at the plasma frequency and resonantly excites a plasma wave. Numerous experiments have produced electron beams with nC charge and divergence varying from a few degrees to tens of degrees and maxwellian energy distributions [Modena et al., 1995, Umstadter et al., 1996a, Moore et al., 1997].

More recently, several groups [Malka et al., 2002, Gahn et al., 1999, Malka et al., 2001, Leemans et al., 2002] have demonstrated that more compact lasers can be used to efficiently generate high-repetition-rate (10Hz) electron sources, which could be used for applications. However, these beams still have very large energy spreads and a low number of electrons at high energy (typically $< 1pC$ at $200 \pm 10MeV$). Previous experiments inherently produced poor-quality beams: wave-breaking occurred under the laser pulse envelope and the accelerated electrons were also under the influence of the ultraintense laser field. Direct laser acceleration [Gahn et al., 1999, Pukhov et al., 1999] by transverse laser field caused the spatial beam quality to deteriorate, causing emittance growth.

The comparison with theory of the generation of high-quality electron beams from ultraintense laserplasma acceleration presented here. Extremely collimated beams with $10mrad$ divergence and $0.5 \pm 0.2nC$ of charge at $170 \pm 20MeV$ have been produced. Contrary to all previous results obtained from laserplasma accelerators, the electron energy distribution is quasi-monoenergetic.

The experiment was performed by focusing ultraintense laser pulse generated in a titanium-doped sapphire, chirped pulse amplification laser system [Strickland and Mourou, 1985, Pittman et al., 2002] onto a helium gas jet (Fig. 2.5). The laser pulse had a $33 \pm 2fs$ duration (FWHM), and contained $1J$ of laser energy at central wavelength $820nm$. It was focused onto the edge of a 3-mm-long supersonic helium gas jet using a $f/18$ off-axis parabola. The diffraction-limited focal spot had a diameter of $r_0 \pm 21\mu m$ at FWHM, producing a vacuum-focused laser intensity of $I = 3.2 \times 10^{18} W cm^{-2}$, for which the corresponding normalized potential vector is $a0 = eA/(mc^2) = 1.3$ (A is the laser vector potential, e and m are respectively the charge and mass of the electron). For these high laser intensities, the helium gas was fully ionized by the foot of the laser pulse and ionization did not play a role in the interaction.

Figure 2.6a shows a picture of the electron beam when no magnetic field is applied. The electron beam is very well collimated, with a $10mrad$ divergence (full-width at half-maximum, FWHM); to our knowledge, this is the smallest divergence ever measured for a beam emerging from a plasma accelerator. Figure 2.6b shows the deviation of the beam when a magnetic field is applied. The image shows a narrow peak around 170MeV, indicating efficient monoenergetic acceleration. For comparison, Fig. 2.6c shows an image obtained at higher electron density in the plasma ($ne = 2 \times 10^{19} cm^{-3}$). Here, electrons are randomly accelerated to all energies and the number of high-energy electrons is low. In addition, the beam divergence is much larger than in Fig. 2.6b. Figure 2.9 shows an electron spectrum after deconvolution. The distribution is clearly quasimonoenergetic and peaks at $170MeV$, with a 24% energy spread (corresponding to the spectrometer resolution).

Finally, the charge contained in this beam can be inferred using an integrating current transformer: the whole beam contains $2 \pm 0.5nC$, and the charge at $170 \pm 20MeV$ is $0.5 \pm 0.2nC$. From the above, we can deduce that the electron beam energy was $100mJ$. Thus, the energy conversion from the laser to the electron beam was 10%.

Experimentally, this regime could be reached in a narrow range of parameters: stretching the pulse duration above $50fs$ was sufficient to lose the peaked energy distribution. Similarly, when the electron density was increased from $6 \times 10^{18} cm^{-3}$ to $7.5 \times 10^{18} cm^{-3}$, the energy distribution became a broad plateau, similar to previous results [Malka et al., 2002]. Above $10^{19} cm^{-3}$, the electron distribution was maxwellian-like with very few electrons accelerated at high energy. Below $6 \times 10^{18} cm^{-3}$, the number of accelerated electrons decreased dramatically, although the distribution was still monoenergetic. The evolution of electron spectra with experimental parameters indicates that using laser pulses shorter than the plasma period is beneficial for high-quality and monoenergetic electron acceleration.

We use three-dimensional (3D) particle-in-cell (PIC) simulations (Virtual Laser Plasma Laboratory [Pukhov, 1999]). The simulation parameters corresponded to the optimal experimental case: the plasma electron density

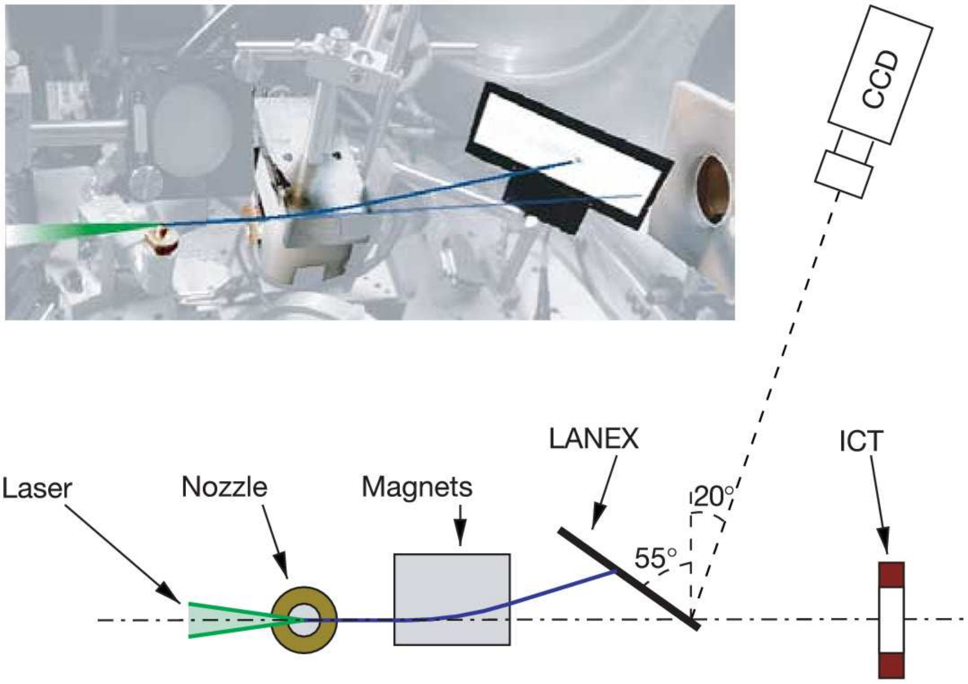

Figure 2.5: Experimental setup (taken from [Faure et al., 2004]). Top represents the picture of the experiment. The setup diagram is shown at the bottom. An ultrashort and ultraintense laser pulse is focused onto a $3mm$ supersonic gas jet and produces a highly collimated $170MeV$ electron beam. LANEX is a phosphor screen; CCD is charge-coupled device camera; ICT is integrating current transformer. The maximum strength parameter attainable on target is $a_0 = 5.6$.

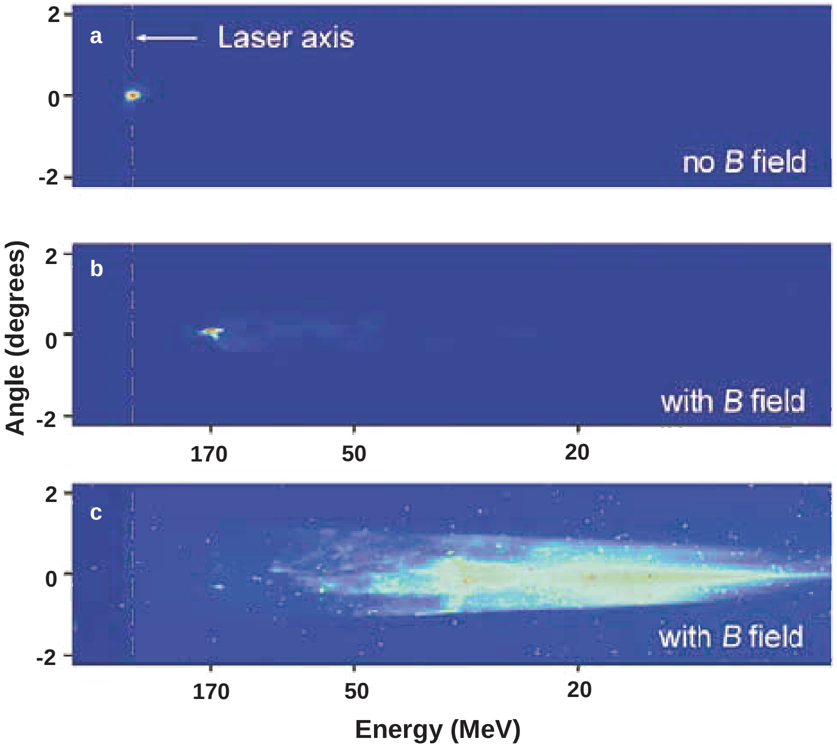

Figure 2.6: Raw images obtained on the LANEX screen (taken from [Faure et al., 2004]). The vertical axis represents the beam angular divergence. When a magnetic field is applied, the horizontal axis represents electron energy. The white vertical dashed line is drawn at the intersection of the laser axis with the LANEX screen. **a**, Image of the electron beam spatial distribution obtained from the LANEX screen when no magnetic field **B** is applied. **b**, Image obtained when the magnetic field is applied, showing that the bulk of the beam is deviated and its position corresponds to $170 MeV$ electrons. The fact that the beam trajectory is displaced when a magnetic field is applied confirms that the signal on the LANEX screen corresponds to electrons and not to photons. **c**, Image obtained with a magnetic field and a higher plasma density ($n_e = 2 \times 10^{19}\ cm^{-3}$). This electron beam has a much larger divergence and a 100% energy spread with few electrons above $100 MeV$.

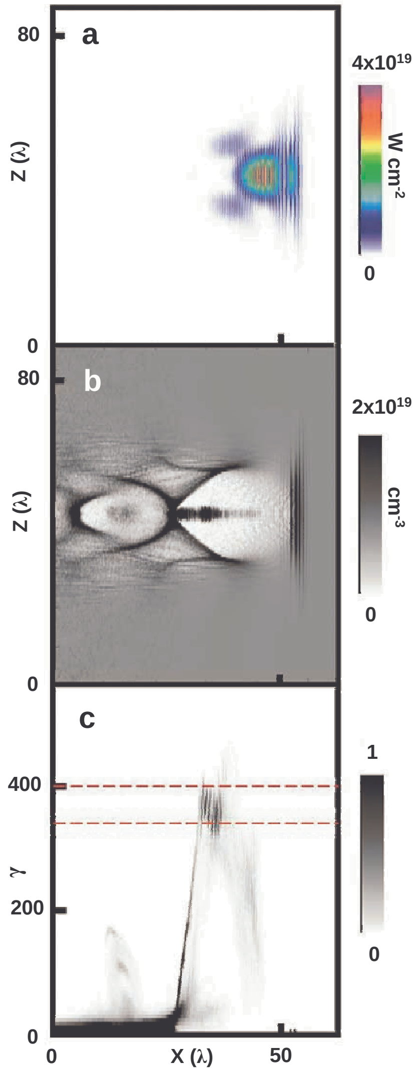

Figure 2.7: 3D PIC simulation results. **a, b**, Distributions of laser intensity (**a**) and electron density (**b**) in the xz plane, which is perpendicular to the polarization direction and passes through the laser axis. The beam of accelerated electrons is seen as the black rod in **b**. These electrons are propagating behind the laser pulse (**a**) and are not disturbed by the laser field. **c**, Electron phase space density $f(x, \gamma)$ in arbitrary units. The red horizontal dashed lines indicate the location of the mono-energetic peak in the phase space.

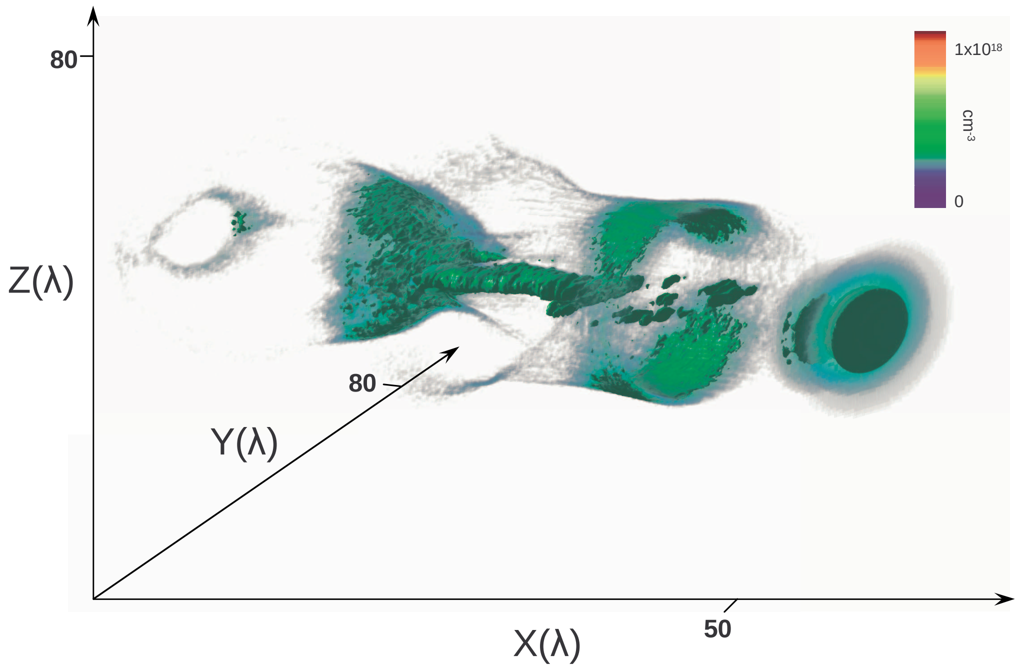

Figure 2.8: 3D PIC simulation results. Distributions of electron density. This 3D picture corresponds to Figure 2.7b. The electrons are propagating behind the laser pulse and are not disturbed by the laser field.

was $ne = 6 \times 10^{18} cm^3$, the laser pulse duration was $30fs$ and the initial laser spot size $21mm$ FWHM. The laser pulse was assumed to be a perfect gaussian containing $1J$ of energy. The plasma profile was chosen to fit the experimental density profile of the gas jet. The simulation results are shown in Fig. 2.7ac and Fig. 2.8. The laser pulse runs from left to right, and has propagated $2mm$ in the plasma. The "bubble" structure is clearly visible. The laser pushes the electron fluid forward at the "bubble" head and creates a density compression there. Behind the laser we see the cavitated region with nearly zero electron density. The radially expelled electrons flow along the cavity boundary and collide at the X-point at the "bubble" base. Some electrons are trapped and accelerated in the "bubble". γ is the relativistic factor of the electron: $\gamma = (1 - v^2/c^2)^{-1/2}$, and v is the electron velocity. We see that the electrons have dephased and have self-bunched in the phase space around $\gamma \gg 350$. This self-bunching results in the mono-energetic peak in the energy spectrum (Fig. 2.9). Our simulation suggests that experimental results can be explained by the following scenario.

1) At the beginning of the simulation, the laser pulse length ($9\mu m$) is nearly resonant with the plasma wave ($\lambda_p = 13.6\mu m$); but its diameter ($21\mu m > \lambda_p$) is larger than the matched diameter.

2) As the pulse propagates in the plateau region of the gas jet, it self-focuses and undergoes longitudinal compression by plasma waves (Fig. 2.7a). This decreases the effective radius of the laser pulse and increases the laser intensity by one order of magnitude.

3) This compressed laser pulse is now resonant with the plasma wave and it drives a highly nonlinear wakefield (Fig. 2.7b): the laser ponderomotive potential expels the plasma electrons radially and leaves a cavitated region behind (this is referred to as the "bubble" regime). In this regime, the 3D structure of the wakefield resembles a plasma "bubble" [Pukhov and Meyer-ter-Vehn, 2002].

4) As the electron density at the walls of the "bubble" becomes large, wave-

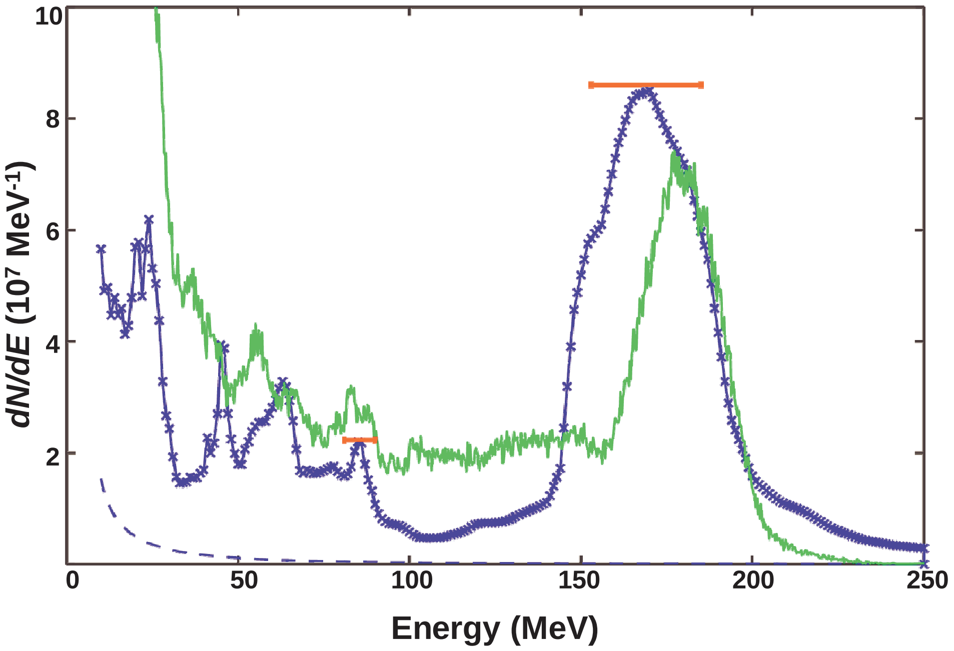

Figure 2.9: Experimental and simulated electron spectra. Blue line with crosses corresponds to Fig. 2.6b after deconvolution. Dashed line denotes estimation of the background level. Red horizontal error bars corresponds to resolution of the spectrometer. Green line corresponds to electron spectrum obtained from 3D PIC simulations. dN/dE is the number of electrons per MeV (E is the electron energy in MeV.)

breaking occurs and electrons are injected and accelerated inside the bubble.

5) As the number of trapped electrons increases, the “bubble” elongates. Its effective group velocity decreases, and electrons start to dephase with respect to the accelerating field. This dephasing causes electron self-bunching in the phase space (Fig. 2.7c). This selfbunching results in the monoenergetic peak in the energy spectrum Fig. 2.9.

Simulations also show that the quality of the electron beam is higher when trapped electrons do not interact with the laser field. If this was to occur, the laser field would cause the electrons to scatter in phase space, degrading the low divergence as well as the monoenergetic distribution. This argument could explain why higher quality beams are obtained experimentally for shorter pulses and lower electron densities.

Figure 2.7a shows that the self-focused and compressed laser pulse stands in front of the trapped electrons (Fig. 2.7b), leaving them almost undisturbed [Malka et al., 2002, Pukhov and Meyer-ter-Vehn, 2002]. The electron energy spectrum obtained from the simulations is shown in Fig. 2.9: it peaks at $175 \pm 25 MeV$, in agreement with the experiment. The divergence of $10 mrad$ is also in agreement with experiment. Simulations also indicate that the electron bunch duration is less than $30 fs$ (here, the term "bunch" refers to the fact that electrons are created in short bursts). Because the electron distribution is quasi-monoenergetic, the bunch will stay short upon propagation: considering a 24% energy spread at $170 MeV$, the bunch stretches by only $50 fs\ m^{-1}$ as it propagates.

Another important point is the apparent robustness of the "bubble" regime. The initial laser parameters for example, the focal spot radius and intensity were far from the final values in the "bubble" (Fig. 2.7). Yet self-focusing led to compression of the laser pulse and to the formation of an electron cavity. The energy of $1J$ for a $30 fs$ laser pulse, used in the experiment, is close to the threshold for this regime. Simulations suggest that with more laser energy and shorter pulses, the formation of the "bubble" will lead to the acceleration of monoenergetic beams at higher energies and higher charges.

The experimental results and our 3D PIC simulations indicate that it is possible to generate a monoenergetic electron beam by carefully selecting laser and plasma parameters. The bunch duration ($< 50 fs$), along with the present improvement in the charge (nC) and the quality of the electron beam (monoenergetic spectrum, low divergence), reinforce the relevance of plasma-based accelerators for many applications (such as high-resolution radiography for non-destructive material inspection, radiotherapy, ultra fast chemistry, radiobiology and material science). With the rapid progress of laser science, we expect that it will soon become possible to generate compact, monoenergetic and high-quality electron beams with a tunable energy range at a reasonable cost. Such a source would be perfectly adapted as an injector for future GeV laserplasma accelerator schemes. It would also be relevant for generating ultra short X-ray sources, using undulators or lasers.

Chapter 3

Betatron Radiation

3.1 Synchrotron emission in an ion channel

3.1.1 Overview

Electron dynamics in plasma-focusing channels has important applications to new plasma technologies, such as advanced accelerators [Esarey et al., 1996], novel radiation sources, new types of lens [Hairapetian et al., 1995]. It is a key phenomenon for ion-channel laser (ICL) [Whittum et al., 1990, Whittum, 1992] and plasma-wiggler free electron laser (FEL) [Joshi et al., 1987], which are perspective candidates for the new type of high brightness X-ray radiation sources. The generation and application of high-brightness X-rays is a fast developing area of science and technology. Diverse demands of research, as well as industrial and medical applications require new more intense and compact X-ray sources [Winick, 1987].

Experiments that explore the interaction of intense 28.5-GeV electron beam with plasma at Stanford Linear Accelerator Center (SLAC) [Wang et al., 2002, Joshi et al., 2002] have shown that the ion channel can be successfully used to produce broadband X-ray radiation.

Moreover, the high density of the ions in the channel provides a much higher wiggler strength than that of a conventional magnet wiggler.

This leads to a more effective generation of X-ray radiation than in the conventional light sources and could be used for the development of the next generation of radiation sources.

To create an ion channel, an electron beam has to interact with plasma in blow-out regime [Rosenzweig et al., 1991], when the electron beam density, n_b, is higher than the plasma density, n_p. In this regime, the electron beam charge quasistatically expels the background plasma electrons out from the beam volume and forms the ion channel. Note that relativistic electrons of the beam are not expelled from the channel because of relativistic compensation of the beam electron charge force by the self-magnetic force [Lawson, 1988]. The channel radius, $r_i \simeq r_0\sqrt{n_b/n_p}$ is much larger than the electron beam radius, r_0, for dense $n_b \gg n_p$ and narrow $k_p r_0 \ll 1$ electron beam [Geraci and Whittum, 2000]. Here $k_p = c/\omega_p$ is the plasma skin depth, $\omega_p = \left(4\pi n_p e^2/m\right)^{1/2}$ is the plasma frequency, e is the electron charge, m is the electron mass and c is the speed of light. If all plasma electrons are expelled from the channel, then the restoring force on the beam electrons due to the ion charge is given by the Gauss law. In the cylindrical geometry it is:

$$\mathbf{F}_{res} = m\omega_p^2\mathbf{r}_\perp/2, \tag{3.1}$$

where $\mathbf{r}_\perp$ is the vector from an electron to the channel axis. The beam electrons in the ion channel undergo betatron oscillations caused by this force. The wavelength for small betatron oscillations is close to $\lambda_b = 2\pi/k_b \simeq 2\pi\sqrt{2\gamma}/k_p$, where γ is the relativistic factor of the electron beam [Clayton et al., 2002].

The relativistic electrons undergoing betatron oscillations in the ion channel emit short-wavelength EM radiation [Jackson, 1975]. Some features of this radiation spectrum have been studied in the recent publications [Wang et al., 2002, Joshi et al., 2002, Esarey et al., 2002]. The wavelength of the radiation is close to $\lambda \simeq \lambda_b/\left(2\gamma^2\right)$ for small-amplitude near-axis betatron oscillations. If the amplitude of the betatron oscillations becomes large, then electron radiates high harmonics. If the plasma wiggler

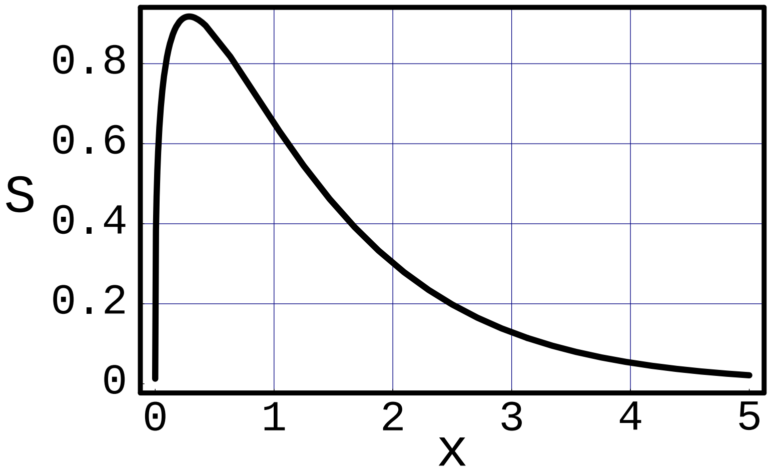

Figure 3.1: The function $S(x)$ versus x.

strength

$$K = \gamma k_b r_0 = 1.33 \times 10^{-10} \sqrt{\gamma n_e \, [\mathrm{cm}^{-3}]} r_0 \, [\mu \mathrm{m}] \tag{3.2}$$

is so high that $K \gg 1$, then the radiation spectrum becomes quasi-continuous broadband. Here r_0 is the amplitude of electron betatron oscillation in the channel. The radiation spectrum becomes similar to the synchrotron one, which is determined by the universal function $S(\omega/\omega_c)$, where

$$S\left(x\right) = x \int_x^\infty K_{5/3}\left(\xi\right) d\xi, \tag{3.3}$$

and ω_c is the critical frequency [Jackson, 1975]. The function $S(x)$ is shown in Fig. 3.1. For frequencies well below the critical frequency ($\omega \ll \omega_c$), the spectrum increases with frequency as $\omega^{2/3}$, reaches a maximum at $\sim 0.29\omega_c$, and then drops exponentially to zero above ω_c. The critical frequency for a relativistic electron in an ion channel is

$$\hbar\omega_c = \frac{3}{2}\gamma^3 \hbar c r_0 k_b^2 \simeq 5 \times 10^{-24} \gamma^2 n_e \left[\mathrm{cm}^{-3}\right] r_0 \, [\mu\mathrm{m}] \, \mathrm{keV}. \tag{3.4}$$

Because of the strongly relativistic motion of the electron, the emitted radiation is confined within a very narrow angle

$$\theta \simeq \frac{K}{\gamma}. \tag{3.5}$$

Synchrotron radiation emitted from an ion channel has been observed in a recent experiment [Wang et al., 2002].

The averaged total power radiated by an electron undergoing betatron oscillations is [Esarey et al., 2002]

$$\langle P_{total} \rangle \simeq \frac{e^2 c}{12} N_0 \gamma^2 k_b^4 r_0^2, \tag{3.6}$$

where N_0 is the number of betatron oscillations performed by the electron. We can introduce also the stopping power of an electron. We define it as the energy loss of an electron per unit distance

$$\begin{aligned} Q &= \frac{\langle P_{total} \rangle}{c} \\ &\simeq 1.5 \times 10^{-45} \left(\gamma n_e \left[\mathrm{cm}^{-3}\right] r_0 \left[\mu\mathrm{m}\right] \right)^2 \frac{\mathrm{MeV}}{\mathrm{cm}}. \end{aligned} \tag{3.7}$$

The averaged number of photons with the mean energy $\hbar\omega_c$ emitted by the electron is

$$\langle N_X \rangle \simeq \frac{2\pi}{9} \frac{e^2}{\hbar c} N_0 K \simeq 5.6 \times 10^{-3} N_0 K. \tag{3.8}$$

It follows from Eq. (3.6) that the radiated power is proportional to the squared density of ions in the channel. This fact has been confirmed in the experiment [Wang et al., 2002].

As it was mentioned above, the ion density in the channel has to be smaller than the electron beam density. This leads to the serious limits on the gain in the radiated power, which is quadratic in plasma density. One of the ways to overcome the limits is to use a laser-produced ion channel. The ion density in such channel can be easily increased to $10^{19} cm^{-3}$ [Key et al., 1998, Wharton et al., 1998, Pukhov and Meyer-ter-Vehn, 2002] that is 5 order higher than the ion density in a channel produced in the simple beam-plasma interaction experiments [Wang et al., 2002]. The use of an ion channel produced by a laser pulse can increase the power of X-ray radiation by 10^{10} times!

We present three-dimensional (3D) particle-in-cell (PIC) simulation of X-ray generation by 25-GeV electron bunch in laser-produced ion channel using Virtual Laser Plasma Laboratory (VLPL) code [Pukhov, 1999]. We observed ultra-high energy γ-quanta (up to several GeV) at high photon flux and brilliance of the radiation.

The spontaneous X-ray emission from an ion channel has been studied in detail in Ref. [Esarey et al., 2002]. The general expression for the spectrum has been derived. It is a complex expression that involves the sum of products of the Bessel function. A numerical evaluation of the spectrum becomes difficult in the limit $K \gg 1$. The simple asymptotic expression for the angular dependence of the radiated spectrum has been derived in this limit only in the plane that is perpendicular to the electron orbit. Here we calculate the general angular dependence of the radiated spectrum.

The resonance interaction between the EM radiation and the betatron oscillations of an electron beam in the ion channel leads to the bunching of the electron beam and then to the amplification (or damping) of EM radiation. It is a stimulated emission (or absorption). The stimulated emission is a basic process in ICLs [Whittum et al., 1990, Whittum, 1992] and FELs [Luchini and Motz, 1990]. The reverse process is the stimulated absorption. It leads to the direct laser acceleration [Pukhov et al., 1999] and to the magnetic field generation [Kostyukov et al., 2002] in relativistic laser channels. Unfortunately, the stimulated emission (absorption) in ion channels has not yet been explored in the limit $K \gg 1$. This is, however, exactly the regime of the ion-channel synchrotron-radiation laser (ICSRL). The general asymptotic expression for the radiation spectrum for arbitrary angular dependencies is derived in the limit $K \gg 1$. The spectrum averaged over the azimuthal angle is calculated for an axially symmetrical electron beam.

3.1.2 Electron dynamics in an ion channel

The relativistic equation of electron motion in a cylindrical ion channel is

$$\frac{d\mathbf{p}}{dt} = \mathbf{F}_{res}, \tag{3.9}$$

where $\mathbf{F}_{res}$ is the restoring force defined by Eq. (3.1). It follows from Eq. (3.9) that the momentum along the channel axis p_z is an integral of motion. First we consider radial betatron oscillations. Assuming that $p_y = 0$ we get the equation for the x-coordinate:

$$\frac{d^2x}{dt^2} = \frac{\gamma_z^2}{2\gamma^3}x, \tag{3.10}$$

Here we introduce the constant of motion $\gamma_z^2 = 1 + p_z^2$. We use dimensionless units, normalizing the time to ω_p^{-1}, the length to c/ω_p, and the momentum to mc.

The Hamiltonian does not depend on time, and thus it is another constant of motion

$$H = \gamma + \frac{x^2}{4} = \text{const} = \gamma_z + \frac{r_0^2}{4}, \tag{3.11}$$

where r_0 is the amplitude of the betatron oscillation. We express γ as a function of x from the obtained relation to resolve Eq. (3.10). Then the transverse motion of the electron can be reduced to oscillations in the effective potential

$$U\left(x\right) = \frac{8\gamma_z^2}{\left(4\gamma_z + r_0^2 - x^2\right)^2}. \tag{3.12}$$

The oscillations can be described in the implicit form:

$$\begin{aligned} t \;=\; & r_0\frac{\sqrt{\nu^2+4}}{\nu}E\left(\arcsin\left(\frac{x}{r_0}\right), \frac{\nu^2}{\nu^2+4}\right) \\ & -\frac{2}{\nu\sqrt{\nu^2+4}}F\left(\arcsin\left(\frac{x}{r_0}\right), \frac{\nu^2}{\nu^2+4}\right). \end{aligned} \tag{3.13}$$

Here $E(x,k)$ and $F(x,k)$ are the elliptic integrals of the first and the second kinds [Abramowitz and Stegun, 1972], respectively, and ν is

$$\nu^2 = r_0^2/2\gamma_z. \tag{3.14}$$

The period of betatron oscillations is

$$\begin{aligned} T_b &= \frac{2\pi}{\omega_b} = 4r_0\frac{\sqrt{\nu^2+4}}{\nu} \\ &\times\left[E\left(\frac{\nu^2}{\nu^2+4}\right) - \frac{2}{\nu^2+4}K\left(\frac{\nu^2}{\nu^2+4}\right)\right], \end{aligned} \tag{3.15}$$

where $K(x)$ and $E(x)$ are the complete elliptic integrals of the first and the second kinds [Abramowitz and Stegun, 1972], respectively. In the limit $\nu^2 \ll 1$, the parameter ν is the ratio of the longitudinal and transversal energy of the electron

$$\nu^2 \simeq p_x^2/\gamma_z^2 \simeq p_\perp^2/p_z^2, \tag{3.16}$$

where p_x is the maximum of the transversal momentum which is at the channel axis $x = 0$. In most applications the transversal moment of the electron is much smaller than the longitudinal one, so we assume $\nu \ll 1$. Now we can use the expansion in ν to describe betatron oscillations:

$$\omega_b = \frac{1}{\sqrt{2\gamma_z}}\left(1 - \frac{3}{8}\nu^2 + ...\right), \tag{3.17}$$

$$x\left(t\right) = r_0 \sin\left(\omega_b t\right) - r_0\frac{3}{64}\nu^2 \sin\left(3\omega_b t\right) + ... \tag{3.18}$$

Using Eq. (3.11) we obtain relations for the electron orbit in the zeroth order in ν that coincides with the ones calculated in Ref. [Esarey et al., 2002]

$$\begin{aligned}
\omega_b &\simeq \frac{1}{\sqrt{2\gamma_z}}, && (3.19)\\
x(t) &\simeq r_0 \sin(\omega_b t), && (3.20)\\
y(t) &\simeq 0, && (3.21)\\
z(t) &\simeq z_0 + \frac{p_z}{\gamma_z}\left(1 - \frac{\nu^2}{4}\right)t - r_0 \frac{p_z}{\gamma_z}\frac{\nu}{8}\sin(2\omega_b t). && (3.22)
\end{aligned}$$

Notice that the parameter ν coincides with the expression $k_b r_0$ introduced in Ref. [Esarey et al., 2002], and the plasma wiggler strength parameter can be expressed through ν as $K \simeq \gamma_z \nu \simeq p_\perp$.

A more general regime of the betatron motion when $p_y \neq 0$ and the electron orbit is not plane has been considered and classified in Ref. [Kostyukov et al., 2002] in the limit $p_z \gg p_\perp$. The electron orbit equation in this case is given by

$$\begin{aligned}
x(t) &\simeq \frac{p_x}{\sqrt{2\gamma_z}}\sin(\omega_b t), && (3.23)\\
y(t) &\simeq \frac{p_y}{\sqrt{2\gamma_z}}\sin(\omega_b t + \psi), && (3.24)\\
z(t) &\simeq z_0 + \frac{p_z}{\gamma_z}\left[1 - \frac{p_x^2 + p_y^2}{4\gamma_z^2} - \frac{p_x^2}{8\gamma_z^2}\sin(2\omega_b t)\right.\\
&\qquad \left. + \frac{p_y^2}{8\gamma_z^2}\sin(2\omega_b t + 2\psi)\right], && (3.25)
\end{aligned}$$

where ψ is the phase difference between oscillations along x-axis and y-axis, p_x and p_y are the maximum of the electron momentum along x-axis and along y-axis, respectively. These maximum momenta are achieved at the channel axis ($x = 0$, $y = 0$). If the angular momentum of an electron, $L = p_y x - p_x y$ is equal to zero, then the electron executes radial harmonic oscillations across the axis with the amplitude $r_0 = 2\sqrt{H}$. If $L = \pm L_{\max} = \pm H/\omega_b$, then the electron motion is circular with the radius r_0. In the general case (an arbitrary value of $-L_{\max} < L < L_{\max}$), the electron trajectory is ellipse-like and is confined between the maximal radius $\sqrt{\left(H+\sqrt{H^2-\omega_b^2L^2}\right)}$, and the minimal radius $\sqrt{\left(H-\sqrt{H^2-\omega_b^2L^2}\right)}$.

3.1.3 Spontaneous synchrotron emission in an ion channel

Using Eqs. (3.23) - (3.25) for the electron trajectory, the energy spectrum radiated by an electron can be calculated [Jackson, 1975, Esarey et al., 2002]. The total radiation flux can be separated in two independent components with polarization in the $\mathbf{e}_\theta$ and $\mathbf{e}_\phi$ directions. Here the unit vectors $\mathbf{e}_\theta$ and $\mathbf{e}_\phi$ correspond to the spherical coordinate system: $x = r\sin\theta\cos\phi$, $y = r\sin\theta\sin\phi$, $z = r\cos\theta$. Then energy radiated per unit frequency interval per unit solid angle in the direction $\mathbf{k} = (\omega/c)\left(\mathbf{e}_x\sin\theta\cos\phi + \mathbf{e}_y\sin\theta\sin\phi + \mathbf{e}_z\cos\theta\right)$ during the interaction time T is [Esarey et al., 2002]:

$$
\begin{aligned}
\frac{dW_{spon,j}}{d\omega d\Omega} &= \frac{e^2}{4\pi^2 c}\eta^2\left|I_j\right|^2, &(3.26)\\
I_\theta &= \int\limits_{-T/2}^{T/2} e^{i\Psi(t)}\left(\frac{dx}{dt}\cos\theta\cos\phi\right.\\
&\qquad \left.+\frac{dy}{dt}\cos\theta\sin\phi-\frac{dz}{dt}\sin\theta\right)dt, &(3.27)\\
I_\phi &= \int\limits_{-T/2}^{T/2}\left(\frac{dx}{dt}\sin\phi-\frac{dy}{dt}\cos\phi\right)e^{i\Psi}dt, &(3.28)
\end{aligned}
$$

$$
\Psi = \eta\left[t - x(t)\sin\theta\cos\phi - y(t)\sin\theta\sin\phi - z(t)\cos\theta\right], \qquad (3.29)
$$

where $j = \theta, \phi$ is the polarization index, the electron trajectory is given by Eqs. (3.23) - (3.25) and $\eta = \omega/\omega_p$. The final results can be expressed

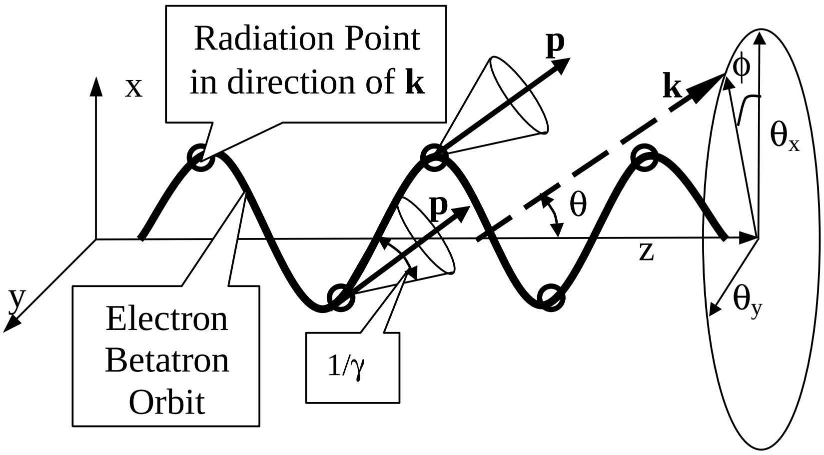

Figure 3.2: Schematic of synchrotron radiation in an ion channel. Open circles show the points on the electron trajectory where the electron emits in the direction of **k**.

as double-infinite series of the Bessel function products (see, for example, Eqs. (32) - (41) in Ref. [Esarey et al., 2002] or can be expressed by the infinite series of the generalized Bessel function introduced in the quantum electrodynamics [Nikishov and Ritus, 1963]).

Unfortunately, the series converge slowly in the limit $K \gg 1$ that makes the numerical evaluation of the radiation spectrum difficult. The energy spectrum and the angular dependence of the radiation have been derived only for directions that are perpendicular to the plane of the betatron oscillation (i. e., for $\phi = \pi/2$) [Esarey et al., 2002]. To extend this result, instead of Bessel function expansion we use here the saddle point method [Morse and Feshbach, 1953] to evaluate the integrals (3.27) and (3.28).

It is well known that the radiation of accelerated relativistic electron is beamed in a very narrow cone in the direction of the electron momentum vector. An observer sees a short pulse of radiation as the searchlight beam sweeps across the observation point [Jackson, 1975] (see Fig. 3.2). So the time moments when the electron momentum, **p**, is directed along wave number,

k, give the main contribution to the integrals (3.27) and (3.28). The pulse duration is very short, and it is necessary to know the electron momentum and the electron position over only a small arc of the trajectory whose tangent points in the direction that is close to the direction of **k**. Then we can expand integrand in Eqs. (3.27) and (3.28) about this time moments and perform the integration. This approach implies that we approximate the part of the electron trajectory near these time moments by arcs of a circular path [Jackson, 1975]. In this case the radiation has the well-known synchrotron-like spectrum. It is noted in Ref. [Landau and Lifshits, 1982] that another necessary condition (the first one is that the electron is relativistic) for use of the synchrotron radiation approach is that the electron deflection angle should be much larger than the simultaneous angle spread of the radiation emission. The electron momentum oscillates within the cone angle $\sim p_\perp/p_z$ (the electron deflection angle). The radiation of the relativistic particle is confined within the angle $1/\gamma$ [Jackson, 1975]. So the validity condition for the synchrotron radiation approach is $p_\perp/p_z \gg 1/\gamma$. This is equivalent to the condition for the high harmonics generation $K \gg 1$. Therefore, the radiation spectrum can be approximated by the synchrotron one if

$$\gamma \gg p_\perp \gg 1. \tag{3.30}$$

This condition is easily satisfied in experiments.

The arguments presented above justify the use of the saddle point method [Morse and Feshbach, 1953] to evaluate the integrals (3.27) and (3.28). We can expand the phase Ψ around the moment of time $\xi_n = \omega_b t_n$ up to the third order:

$$\Psi = \Psi_0 + b_1(\xi - \xi_n) + b_2(\xi - \xi_n)^2 + b_3(\xi - \xi_n)^3, \tag{3.31}$$

$$\begin{aligned} \Psi_0 &= \Psi\left(\xi_n\right) = \alpha_0\xi_n - \alpha_x \sin\left(\xi_n\right) - \alpha_y \sin\left(\xi_n + \psi\right) \\ &\quad + \alpha_{zx} \sin\left(2\xi_n\right) + \alpha_{zy} \sin\left(2\xi_n + 2\psi\right), \end{aligned} \tag{3.32}$$

$$\begin{aligned} b_1 &= \left.\frac{d\Psi}{d\xi}\right|_{\xi=\xi_n} = \alpha_0 - \alpha_x \cos\left(\xi_n\right) - \alpha_y \cos\left(\xi_n + \psi\right) \\ &\quad + 2\alpha_{zx} \cos\left(2\xi_n\right) + 2\alpha_{zy} \cos\left(2\xi_n + 2\psi\right), \end{aligned} \tag{3.33}$$

$$\begin{aligned} b_2 &= \left.\frac{d^2\Psi}{d\xi^2}\right|_{\xi=\xi_n} = \alpha_x \sin\left(\xi_n\right) + \alpha_y \sin\left(\xi_n + \psi\right) \\ &\quad - 4\alpha_{zx} \sin\left(2\xi_n\right) - 4\alpha_{zy} \sin\left(2\xi_n + 2\psi\right), \end{aligned} \tag{3.34}$$

$$\begin{aligned} b_3 &= \left.\frac{d^3\Psi}{d\xi^3}\right|_{\xi=\xi_n} = \alpha_x \cos\left(\xi_n\right) + \alpha_y \cos\left(\xi_n + \psi\right) \\ &\quad - 8\alpha_{zx} \cos\left(2\xi_n\right) - 8\alpha_{zy} \cos\left(2\xi_n + 2\psi\right), \end{aligned} \tag{3.35}$$

where

$$\alpha_0 = \frac{\eta}{\omega_b}\left[1 - \frac{p_z}{\gamma_z}\left(1 - \frac{p_x^2 + p_y^2}{4\gamma_z^2}\sin\theta\cos\phi\right)\right], \tag{3.36}$$

$$\alpha_x = \frac{\eta}{\omega_b}\frac{p_x}{\gamma_z}\sin\theta\cos\phi, \tag{3.37}$$

$$\alpha_y = \frac{\eta}{\omega_b}\frac{p_y}{\gamma_z}\sin\theta\cos\phi, \tag{3.38}$$

$$\alpha_{zx} = \frac{\eta}{\omega_b}\frac{p_z}{\gamma_z}\frac{p_x^2}{8\gamma_z^2}\cos\theta, \tag{3.39}$$

$$\alpha_{zy} = \frac{\eta}{\omega_b}\frac{p_z}{\gamma_z}\frac{p_y^2}{8\gamma_z^2}\cos\theta. \tag{3.40}$$

Now we can expand the pre-exponent factors in Eqs. (3.27) and (3.28) about the moment of time $\xi_n = \omega_b t_n$ to the first order:

$$\begin{aligned} & \frac{dx}{dt}\cos\theta\cos\phi + \frac{dy}{dt}\cos\theta\sin\phi - \frac{dz}{dt}\sin\theta \\ = \; & B_{\theta,n} + D_{\theta,n}(\xi - \xi_n), \end{aligned} \tag{3.41}$$

$$\frac{dx}{dt}\sin\phi - \frac{dy}{dt}\cos\phi = B_{\phi,n} + D_{\phi,n}(\xi - \xi_n), \tag{3.42}$$

where

$$\begin{aligned} B_{\theta,n} \;&=\; \cos\theta\left[\frac{p_x}{\gamma_z}\cos\xi_n\cos\phi + \frac{p_y}{\gamma_z}\cos\left(\xi_n + \psi\right)\sin\phi\right] \\ &\quad -\sin\theta\frac{p_z}{\gamma_z} + \sin\theta\frac{p_z p_x^2}{4\gamma_z^3}\cos\left(2\xi_n\right) \\ &\quad +\sin\theta\frac{p_z p_y^2}{4\gamma_z^3}\cos\left(2\xi_n + 2, \psi\right) \end{aligned} \tag{3.43}$$

$$\begin{aligned} D_{\theta,n} \;&=\; -\cos\theta\left[\frac{p_x}{\gamma_z}\sin\xi_n\cos\phi + \frac{p_y}{\gamma_z}\sin\left(\xi_n + \psi\right)\sin\phi\right] \\ &\quad -\sin\theta\frac{p_z p_x^2}{2\gamma_z^3}\sin\left(2\xi_n\right) \\ &\quad -\sin\theta\frac{p_z p_y^2}{2\gamma_z^3}\sin\left(2\xi_n + 2\psi\right), \end{aligned} \tag{3.44}$$

$$B_{\phi,n} = \frac{p_x}{\gamma_z}\sin\phi\cos\left(\xi_n\right) - \frac{p_y}{\gamma_z}\cos\phi\cos\left(\xi_n + \psi\right), \tag{3.45}$$

$$D_{\phi,n} = -\frac{p_x}{\gamma_z}\sin\phi\sin\left(\xi_n\right) + \frac{p_y}{\gamma_z}\cos\phi\sin\left(\xi_n + \psi\right). \tag{3.46}$$

Notice that it is sufficient to keep the leading term in the pre-exponent factor while the other terms much less than unity can be neglected in the exponent argument.

The main contribution to the integral comes from the neighbourhood of the saddle points specified by $d\Psi/d\xi = 0$ [Morse and Feshbach, 1953]. The first-order term in phase expansion (3.31) can be written as follows

$$\left.\frac{d\Psi}{d\xi}\right|_{\xi=\xi_n} = \frac{\eta}{\omega_b}\left(1 - \frac{\mathbf{k}\cdot\mathbf{p}}{k\gamma}\right) \simeq \frac{\eta}{2\omega_b}\left(\frac{1}{\gamma^2} + \varphi^2\right), \tag{3.47}$$

where φ is the angle between $\mathbf{k}$ and $\mathbf{p}$. It follows from Eq. (3.47) that $d\Psi/d\xi$ is minimal and close to zero at $\varphi = 0$ when the electron momentum is directed along $\mathbf{k}$ that agrees with the qualitative argument presented above.

For the sake of simplicity, we assume that $p_y = 0$, i.e., the electron orbit is plane and the betatron oscillations are radial. It follows from Eq. (3.33) that the values of ξ whose neighborhood gives the main contribution to the integral are defined by the relation

$$\cos\xi_n = \frac{\gamma_z}{p_x}\tan\theta\cos\phi. \tag{3.48}$$

It is seen from Eq. (3.48) and Fig. 3.2 that the number of saddle points is $2N_0 = \omega_b T/\pi$ that is the number of times when the direction of the electron momentum and the direction of the wave number coincides. It can be shown [Jackson, 1975] that the second-order term can be neglected in Eq. (3.31). Then Eqs.(3.27) and (3.28) take the form:

$$I_j = \frac{1}{\omega_b}\sum_{n=1}^{2N_0}\exp\left(i\Psi_{0,n}\right)R_{j,n}, \tag{3.49}$$

$$\begin{aligned} R_{j,n} &= \int_{-\infty}^{+\infty}\left(B_{j,n} + D_{j,n}s_n\right) \\ &\quad \times \exp\left[ib_{1,n}s_n + ib_{3,n}s_n^3\right]ds_n, \end{aligned} \tag{3.50}$$

where $j = \theta, \phi$ is the polarization index, $s_n = \xi_n - \xi_0$, $\Psi_{0,n}$ is the value of phase Ψ in the n-th saddle point.

It follows from the saddle point definition Eq. (3.48) and from Eqs. (3.31)-(3.46) that $R_{j,n} = R_{j,n-1} = R_j$, $B_{j,n} = B_{j,n-1} = B_j$, $D_{j,n} = D_{j,n-1} = D_j$, $b_{m,n} = b_{m,n-1} = b_m$. Accomplishing the integration in Eq. (3.50) we obtain

$$R_j = \sqrt{\frac{8b_1}{3b_3}}\left[B_j K_{1/3}\left(\sqrt{\frac{8b_1^3}{9b_3}}\right)\right.$$
$$\left.+D_j\sqrt{\frac{2b_1}{b_3}}K_{2/3}\left(\sqrt{\frac{8b_1^3}{9b_3}}\right)\right], \tag{3.51}$$

where $K_{1/3}(x)$ and $K_{2/3}(x)$ are the modified Bessel functions [Abramowitz and Stegun, 1972]. In the synchrotron regime of radiation $\omega \sim \omega_c \gg \omega_p$ and $\Psi_{0,n} \gg 1$ then we can write for large number of the betatron periods ($N_0 \gg 1$)

$$\left|\sum_{n=1}^{2N_0}\exp\left(i\Psi_{0,n}\right)\right|^2 \simeq 2N_0. \tag{3.52}$$

Using Eqs. (3.16), (3.26), (3.51) and condition (3.30) we finally get

$$\frac{d^2W_{spon,\theta}}{d\omega d\Omega} = 2N_0\frac{e^2\eta^2\rho^2\chi^2\cos^2\phi}{3\pi^2 c} \times\left[\frac{\sin\theta\sin^2\phi}{\sqrt{\chi}}K_{1/3}(q)+K_{2/3}(q)\right]^2 \tag{3.53}$$

$$\frac{d^2W_{spon,\phi}}{d\omega d\Omega} = 2N_0\frac{e^2\eta^2\rho^2\chi^2\sin^2\phi}{3\pi^2 c} \times\left[\frac{\sin\theta\cos\phi}{\sqrt{\chi}}K_{1/3}(q)-K_{2/3}(q)\right]^2, \tag{3.54}$$

where

$$\rho = \sqrt{\frac{2\gamma_z}{p_x^2/\gamma_z^2-\sin^2\theta\cos^2\phi}} \tag{3.55}$$

is the curvature radius of the circular path that is used to approximate the part of the electron trajectory where the electron emits in the direction of **k**,

$$\chi = \gamma_z^{-2}+\sin^2\theta\sin^2\phi, \tag{3.56}$$

$$q = \frac{1}{3}\eta\rho\chi^{3/2}. \tag{3.57}$$

The total radiation of the spontaneous emission from the electron in the channel is

$$\begin{aligned} \frac{d^2W_{spon}}{d\omega d\Omega} &= \frac{d^2W_{spon,\theta}}{d\omega d\Omega} + \frac{d^2W_{spon,\phi}}{d\omega d\Omega} \\ &= 2N_0\frac{e^2\eta^2\rho^2\chi^2}{3\pi^2 c}\left[\frac{\sin^2\theta\sin^2\phi}{\chi}K_{1/3}^2(q) + K_{2/3}^2(q)\right]. \end{aligned} \tag{3.58}$$

This is the general expression for the angular distribution of the radiation emitted by an a relativistic electron in the ion channel.

Let us consider some limiting cases. It follows from the condition (3.30) that $\theta \ll 1$. Then in the limit $\phi = \pi/2$ Eq. (3.58) takes the form

$$\frac{d^2W_{spon}}{d\omega d\Omega} = N_0\frac{6e^2}{\pi^2 c}\frac{\gamma_z^2 q^2}{(1+\gamma_z^2\theta^2)}\left[\frac{\gamma_z^2\theta^2}{(1+\gamma_z^2\theta^2)}K_{1/3}^2(q) + K_{2/3}^2(q)\right], \tag{3.59}$$

that coincides with the asymptotic spectrum emitted by the relativistic electron in the channel for $\phi = \pi/2$ (see Eq. (64) in Ref. [Esarey et al., 2002]). It was discussed above that in the limit $K \gg 1$ the radiation emitted by an electron at a given moment of time is similar to the synchrotron radiation emitted from an electron in an instantaneously circular motion with the same curvature radius. Indeed, introducing the notation $\varphi = \sin\theta\sin\phi$ and using relation $\gamma \simeq \gamma_z \simeq p_z$ we can reduce Eq. (3.58) to the known form

$$\begin{aligned} \frac{d^2W_{spon}}{d\omega d\Omega} &= 2N_0\frac{e^2\left(\eta\rho\right)^2}{3\pi^2 c}\left(\frac{1}{\gamma^2}+\varphi^2\right)^2 \\ &\quad\times\left[K_{2/3}^2(q) + \frac{\varphi^2}{1/\gamma^2+\varphi^2}K_{1/3}^2(q)\right], \end{aligned} \tag{3.60}$$

that coincides with the expression for energy radiated by a relativistic electron in instantaneously circular motion with radius ρ per unit frequency

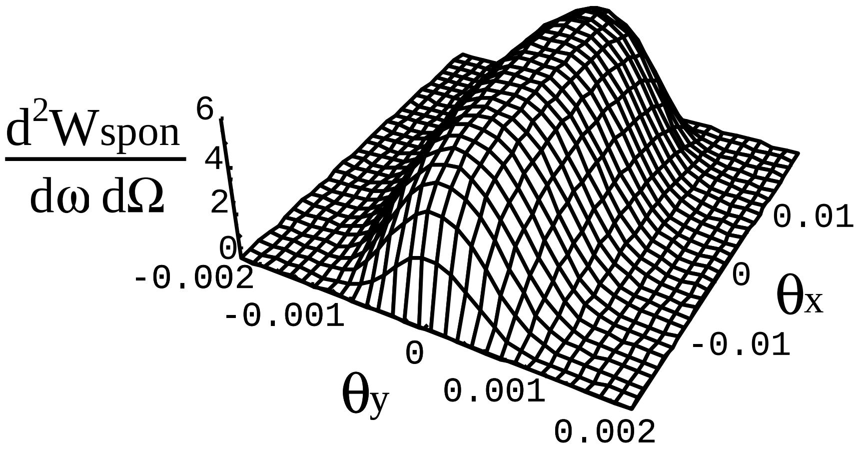

Figure 3.3: Angular distribution of the spontaneous emission spectrum $\frac{d^2W_{spon}}{d\omega d\Omega}$ (arbitrary units) versus angles θ_x and θ_y from a single electron with $\gamma_z = 1000$, $K = p_x = 20$ for $\omega = 0.5\omega_c$.

per unit solid angle $2\pi \cos\varphi d\varphi$ after $2N_0$ revolutions (see, for example, Eq. (14.83) in Ref. [Jackson, 1975]).

To visualize our results we use new angle coordinates $\theta_x = \sin\theta\cos\phi$, $\theta_y = \sin\theta\sin\phi$ instead of the spherical one (θ, φ) (see Fig. 3.2 and Fig. 3.3). It is seen from Fig. 3.3 that there is no radiation for $\theta_x > \theta_{\max}$ because the argument of the Bessel function in Eq. (3.58) goes to infinity and the Bessel function goes to zero for $\theta_x = \theta_{\max}$. Therefore in our approximation the emission angle along x-axis is confined to the electron deflection angle $\theta_{\max} = p_x/p_z$. However it is evident that electrons with maximal deflection angle p_x/p_z emit radiation up to the angle $\theta = \pm(\theta_{\max} + \gamma^{-1})$. The emission angle is confined within the angle $\sim 1/\gamma$ in the direction of y-axis which is normal to the electron orbit plane. Hence our results agree with the qualitative analysis in Ref. [Esarey et al., 2002].

Averaging Eq. (3.58) over θ_y we obtain

$$\int_{-1}^{1}\frac{d^2W_{spon}}{d\omega d\Omega}d\theta_y=\frac{\sqrt{3}}{2}N_0\frac{e^2\gamma_z}{\pi c}S\left(\frac{2}{3}\frac{\sqrt{2}\eta}{\gamma_z^{3/2}\sqrt{p_x^2-\gamma_z^2\theta_x^2}}\right),\qquad(3.61)$$

where $S\left(x\right)$ is the universal function mentioned in Introduction. Using Eqs. (3.4), (3.14) and (3.16) the argument of the function $S(x)$ can be reduced to the ω/ω_c in the limit $\theta_x=0$ that corresponds the spectrum of the synchrotron radiation of the relativistic electron. The expression (3.61) can be considered as a radiation power emitted by a flow of electrons uniformly distributed along the y-axis. The $y-$axis is directed normally to the betatron oscillation plane. The electrons are moving along the z-axis. The ion channel in this slab geometry is an ion layer perpendicular to the x-axis.

Let us now consider a monoenergetic, axisymmetric electron beam. Radiation spectrum from electron beam with electron distribution function $f\left(\mathbf{p}\right)$ is defined by the relation:

$$\left\langle\frac{d^2W_{spon}}{d\omega d\Omega}\right\rangle=\int_0^{2\pi}\frac{d\phi}{2\pi}\int_{-\infty}^{+\infty}d\mathbf{p}f\left(\mathbf{p}\right)\frac{d^2W_{spon}}{d\omega d\Omega}\left(\mathbf{k},\mathbf{p}\right).\qquad(3.62)$$

Let all electrons have the same longitudinal and transversal energy before interaction and the electron distribution function is

$$f\left(\mathbf{p}\right)=\delta(p_z-\gamma_z)\delta(\sqrt{p_x^2+p_y^2}-p_\perp).\qquad(3.63)$$

Then the radiation spectrum from the beam takes the form

$$\left\langle\frac{d^2W_{spon}}{d\omega d\Omega}\right\rangle=\int_0^{2\pi}\frac{d\phi}{2\pi}\frac{d^2W_{spon}}{d\omega d\Omega}.\qquad(3.64)$$

In the limit of near-axis radiation $\theta\ll 1/\gamma_z$, the radiation spectrum is

$$\left\langle\frac{d^2W_{spon}}{d\omega d\Omega}\right\rangle\simeq 2N_0\frac{3e^2}{\pi^2c}\left(\frac{\sqrt{2}\eta}{3p_x\gamma_z^{3/2}}\right)^2K_{2/3}^2\left(\frac{\sqrt{2}\eta}{3p_x\gamma_z^{3/2}}\right).\qquad(3.65)$$

In the opposite limit, $\theta\gg 1/\gamma_z$, the main contribution to Eq. (3.64) is given by the small values of $\phi\ll 1$ that correspond to the minimum of q. The radiation spectrum in this limit is

$$\left\langle \frac{d^2W_{spon}}{d\omega d\Omega} \right\rangle \simeq \frac{\sqrt{3}}{2} N_0 \frac{e^2\gamma_z}{\pi c\theta} S\left(\frac{2}{3} \frac{\sqrt{2}\eta}{\gamma_z^{3/2}\sqrt{p_x^2-\gamma_z^2\theta^2}} \right). \tag{3.66}$$

Notice that the obtained expression coincides with Eq. (3.61).

3.1.4 Ion channel synchrotron radiation laser

When an EM wave of approximately the same frequency as the spontaneous emission propagates through the ion channel simultaneously with the electron beam, a significant exchange of energy between the beam and the wave can occur and lead to the coherent efficient amplification of the wave energy. This amplification can be explained in terms of the stimulated emission processes that determines the operation of ICL. Unlike the ICL theory [Whittum et al., 1990, Whittum, 1992], here we consider the regime of a strong wiggler field ($K \gg 1$), when the emission process is close to the synchrotron one. This is the regime of the ion-channel synchrotron-radiation laser.

The difference between the spontaneous and stimulated emissions is the following. The radiation fields generated by an electron undergoing betatron oscillations has a phase which depends on the time of arrival of the electrons at the channel entrance. The fields produced by different electrons in a uniform input beam have a random phase relation to each other and sum up incoherently. This leads to the incoherent spontaneous radiation. Contrary to the spontaneous emission, electrons in the ion channel can be driven by an external EM wave in synchronous oscillation, the phase of which is no longer random, but locked to the phase of the wave. As a result, the external wave causes the bunching of the electron beam and the more efficient interaction between the beam and the wave. Then the radiation fields of different electrons sum up coherently to each other and to the external wave leading either to a decrease or to an increase of the power. The wave amplification or absorption depends on whether the interference is constructive or destructive. In quantum approach the amplification/absorption can be viewed as a transition between the quantum states of the electron in the ion channel with photon absorption/emission forced by the external wave. An amplification process of this kind is called stimulated emission. It is known from the laser physics that the stimulated emission can be much more efficient and powerful than the spontaneous one.

As it is known in the quantum physics [Heitler, 1954], there is a relation between the spontaneous and stimulated emission. Using this fact the elementary quantum methods based on the Einstein coefficients have been used to study the instability of EM waves in cosmic plasmas [Twiss, 1958, Ginzburg and Zhelenyakov, 1958]. Particularly, the synchrotron instability in a cold magnetoactive plasmas has been identified [Zheleznyakov, 1967, Fung, 1969]. The relation between the spontaneous and stimulated emission of electrons in undulators is called Madey's theorem in the theory of FELs [Madey, 1979]. It can be considered as an extension of the Einstein coefficients method to the classical limit. The generalized Madey theorem [Luchini and Motz, 1990, Fraiman and Kostyukov, 1995] enables us to reduce the problem of ICSRL gain to the problem solved in Sec. III that is the calculation of the power of spontaneous emission in an ion channel.

To use Madey's theorem we should formulate the problem within the Hamiltonian approach. An electron motion in an ion channel and in the EM wave can be described by a relativistic Hamiltonian

$$H = \sqrt{1 + (\mathbf{p}_\perp + \mathbf{A}_i)^2 + p_z^2} + \frac{x^2 + y^2}{4}, \tag{3.67}$$

where $\mathbf{A}_i$ is the vector potential of the wave with θ or ϕ polarizations ($i = \theta, \phi$):

$$\begin{aligned} \mathbf{A}_\theta &= A_0 \left(\mathbf{e}_x \cos\theta \cos\phi + \mathbf{e}_y \cos\theta \sin\phi - \mathbf{e}_z \sin\theta\right) \\ &\quad \times \exp\left[i\eta t - i\eta \left(\mathbf{k}\cdot\mathbf{r}\right)/k\right], \end{aligned} \tag{3.68}$$

$$\mathbf{A}_\phi = A_0 \left(\mathbf{e}_x \sin\phi - \mathbf{e}_y \cos\phi\right) \exp\left[i\eta t - i\eta \left(\mathbf{k}\cdot\mathbf{r}\right)/k\right]. \tag{3.69}$$

Hamiltonian (3.67) is again written in dimensionless units, normalizing the time to ω_p^{-1}, the length to c/ω_p, the momentum to mc, the vector potential to mc^2/e. As usual, we assume that the time of arrival of the electrons at the channel entrance is random. Assuming that the external EM wave is weak we can consider it as a perturbation and use the perturbation theory to calculate the work done upon the electron beam by an EM wave with j-polarization. It follows from the generalized Madey theorem (see, for example, Eq. (5.52) in Ref. [Luchini and Motz, 1990]) that this work per beam electron is

$$\langle W_j \rangle = \frac{1}{2}\frac{\partial \left\langle \gamma_{1,j}^2 \right\rangle}{\partial \gamma_0} + \frac{1}{2}\frac{\mathbf{k}_\perp}{k} \cdot \frac{\partial \left\langle \gamma_{1,j}^2 \right\rangle}{\partial \mathbf{p}_\perp}, \tag{3.70}$$

where $\gamma_{1,j}$ is the first-order work done upon a single electron moving along the unperturbed electron trajectory $\mathbf{r}^0(t)$ by EM wave with j-polarization

$$\gamma_{1,j} = \int_{-\infty}^{+\infty} dt \frac{d\mathbf{r}^0(t)}{dt} \cdot \mathbf{A}_i \left[t, \mathbf{r}^0(t)\right], \tag{3.71}$$

where γ_0 and $\mathbf{p}_\perp$ are the electron energy and the transversal momentum of the electron before the interaction. The unperturbed electron trajectory $\mathbf{r}^0(t)$ is determined by Eqs. (3.23) - (3.25). Averaging in Eq. (3.70) implies the averaging over the time of arrival of the electrons at the channel entrance. Mathematical statement of the Madey theorem is that the second-order quantity, $\langle W_j \rangle$, is proportional to the average squared first-order quantities, $\gamma_{1,j}$. Therefore Madey's theorem essentially simplifies calculations in the framework of the perturbation theory. Using instead of the variables γ_0 and $\mathbf{p}_\perp$ the initial value of the electron momentum $\mathbf{p} = (\mathbf{p}_\perp, p_z)$, Eq. (3.70) can be also rewritten in a more symmetric form

$$\langle W_j \rangle = \frac{1}{2}\frac{\mathbf{k}}{k} \cdot \frac{\partial \left\langle \gamma_{1,j}^2 \right\rangle}{\partial \mathbf{p}}. \tag{3.72}$$

Similar to the FEL theory we introduce the incremental gain of ICSRL as a ratio between the power generated by the electron beam and the incoming EM wave power

$$\Gamma_j = \frac{2\lambda^2 r_e n_b \langle W_j \rangle}{\pi A_0^2}, \tag{3.73}$$

where n_b is the density of the electron beam, $r_e = mc^2/e^2$ is the classical electron radius, $\lambda = 2\pi c/\omega$ is the wavelength of the EM wave. It should be noted that in order to calculate $\langle W_j \rangle$ we take the given EM wave and do not consider the dynamics of EM wave during the interaction. Hence, our calculations are valid for $\Gamma \ll 1$. This regime of interaction is called in the FEL theory as a small-signal small-gain regime [Luchini and Motz, 1990].

It follows from Eqs. (3.27), (3.28) and (3.71) that $\gamma_{1,j}$ is proportional to I_j. That is the particular case of the general reciprocity relation between the far field of the moving electron and the work done by the plane EM wave on it [Luchini and Motz, 1990]. Therefore we can express the quantity $\left\langle \gamma_{1,j}^2 \right\rangle$ through the energy of the spontaneous emission energy radiated per frequency per solid angle

$$\left\langle \gamma_{1,j}^2 \right\rangle = A_0^2 \left(\frac{e^2}{4\pi^2 c} \frac{\omega^2}{\omega_p^2} \right)^{-1} \frac{d^2 W_{spon,j}}{d\omega d\Omega}. \tag{3.74}$$

and we express the gain in term of $\frac{d^2 W_{spon,j}}{d\omega d\Omega}$

$$\Gamma_j = \frac{\lambda^2 r_e n_e}{\pi} \left(\frac{e^2}{4\pi^2 c} \frac{\omega^2}{\omega_p^2} \right)^{-1} \left(\frac{\mathbf{k}}{k} \cdot \frac{\partial}{\partial \mathbf{p}} \right) \frac{d^2 W_{spon,j}}{d\omega d\Omega}. \tag{3.75}$$

It has been noted in the previous Section that the efficient spontaneous emission in the direction $\mathbf{k}$ takes place only at a short moment of time when the electron moment is directed along $\mathbf{k}$. Therefore we can conclude from Eq. (3.75) that the interaction with an EM wave propagating in the direction of $\mathbf{k}$ is only possible at the same moments of time. It was mentioned in Sec. 3.1.3 (see Fig. 3.2) that the number of the interactions moments is $2N_0$. The number of electron oscillations in the EM wave between the interaction moments is extremely large. So we can suppose that the electron phases are random at the interaction moments and can consider the interaction moments independently. Using this fact Eq. (3.75) can be rewritten as follows

$$\begin{aligned}\Gamma_j &= 2N_0 \frac{\lambda^2 r_e n_e}{\pi} \left(\frac{e^2}{4\pi^2 c} \frac{\omega^2}{\omega_p^2} \right)^{-1} \\ &\times \left(\frac{\mathbf{k}}{k} \cdot \frac{\partial}{\partial \mathbf{p}} \right) \left(\frac{d^2 W_{spon,j}}{d\omega d\Omega} \frac{1}{N_0} \right). \end{aligned} \tag{3.76}$$

For simplicity we assume that $p_y = 0$. To take derivatives in Eq. (3.76) we should present $\frac{d^2 W_{spon,j}}{d\omega d\Omega}$ as a function of the momentum, $\mathbf{p}$, and use the simplifying assumptions $p_y = 0$ only after performing the differentiation in Eq. (3.76). This is because the electron motion in the ion channel and in the EM wave is no longer plane. Although the unperturbed betatron oscillation is in the plane $y = 0$, the action of the EM wave leads to small oscillations along y-axis in the first-order of perturbation theory.

It follows from Eqs. (3.26), (3.49) and (3.52) that

$$\left(\frac{e^2}{4\pi^2 c} \frac{\omega^2}{\omega_p^2} \right)^{-1} \frac{d^2 W_{spon,j}}{d\omega d\Omega} \frac{1}{N_0} = \frac{2}{\omega_b^2} \eta^2 \left| R_j \right|^2. \tag{3.77}$$

Then using Eqs. (3.33)-(3.51) we can perform the differentiation in Eq. (3.75). To do it we have to take into account that γ_z, ω_b are functions of p_z: $\gamma_z(p_z) = \sqrt{1 + p_z^2}$, $\omega_b(p_z) = 1/\sqrt{2\gamma_z(p_z)}$. Having performed the differentiation we can put $p_y = 0$. Then we simplify the obtained expression with the help of MATHEMATICA [Wolfram, 1991] and derive the gain of ICSRL:

$$\begin{aligned}
\Gamma_\phi &= N_0 \frac{\sqrt{2}\lambda^2 r_e n_e}{9\pi} \frac{\rho^4 \sin^2\phi}{\gamma_z^3 p_x} \\
&\quad \times \left[\sin\theta\cos\phi K_{1/3}(q) - \sqrt{\chi} K_{2/3}(q)\right] \\
&\quad \times \left[\sqrt{\chi}\left(3qT_0 + \sin\theta\sqrt{\chi}T_1\right) K_{1/3}(q)\right. \\
&\quad \left. - \left(3q\sin\theta\cos\phi T_0 + \chi^{3/2}T_2\right) K_{2/3}(q)\right], \qquad (3.78) \\
T_0 &= -3p_x^3 + \sin^2\theta\cos^2\phi\left[3p_x^3 - 8p_x^2\gamma_z\sin\theta\cos\phi\right. \\
&\quad \left. +2\gamma_z^3\sin^3\theta\cos\phi\left(1+2\cos^2\phi\right) - p_x\gamma_z^2\sin^2\theta\cos^2\phi\right], \\
T_1 &= 6p_x^3\cos\phi - 2\gamma_z^3\sin^3\theta\cos^2\phi(1-4\cos^2\phi) \\
&\quad +2p_x^2\gamma_z\sin\theta\left(3-8\cos^2\phi\right) - 2p_x\gamma_z^2\sin^2\theta\cos^3\phi, \\
T_2 &= 3p_x^3 - 8p_x^2\gamma_z\sin\theta\cos\phi - p_x\gamma_z^2\sin^2\theta\cos^2\phi \\
&\quad +2\gamma_z^3\sin^3\theta\cos\phi(1+2\cos^2\phi),
\end{aligned}$$

$$\begin{aligned}
\Gamma_\theta &= N_0 \frac{\sqrt{2}\lambda^2 r_e n_e}{9\pi} \frac{\rho^4}{\gamma_z^3 p_x} \\
&\quad \times \left[\sin\theta\sin^2\phi K_{1/3}(q) + \sqrt{\chi}\cos\phi K_{2/3}(q)\right] \\
&\quad \times \left[\sqrt{\chi}\left(3q\cos\phi T_0 + \sin\theta\sqrt{\chi}T_3\right) K_{1/3}(q)\right. \\
&\quad \left. + \left(3q\sin\theta\sin^2\phi T_0 + \chi^{3/2}T_4\right) K_{2/3}(q)\right], \qquad (3.79) \\
T_3 &= 6p_x^3 - 16p_x^2\gamma_z\sin\theta\cos\phi - 2p_x\gamma_z^2\sin^2\theta\cos^2\phi \\
&\quad +4\gamma_z^3\sin^3\theta\cos\phi\left(1+2\cos^2\phi\right), \\
T_4 &= 3p_x^3\cos\phi + 2p_x^2\gamma_z\sin\theta\left(3-4\cos^2\phi\right) \\
&\quad +p_x\gamma_z^2\sin^2\theta\cos^3\phi - 4\gamma_z^3\sin^3\theta\cos^2\phi\sin^2\phi.
\end{aligned}$$

We have also checked the obtained results by the numerical differentiation for some values of parameters. It follows from Eqs. (3.78) and (3.79) that the EM wave can be amplified if the wave propagates at a small angle to the axis z. It is seen from Fig. 3.4 that there is no amplification of EM wave when the wave propagates exactly along the channel axis.

Eqs. (3.54) and (3.53) have been derived under assumption that all the electrons have the same momentum before interaction. Now we consider a monoenergetic, axisymmetric electron beam with the electron distribution function given by Eq. (3.63). The ICSRL gain for such electron beam is defined by the relation

$$\langle \Gamma_j \rangle = \int_0^{2\pi} \frac{d\phi}{2\pi} \Gamma_j \left(\mathbf{p}, \phi \right). \tag{3.80}$$

We have performed the integration in Eq. (3.80) numerically (Chapter 3.2). We are not able to find the wave amplification by the axisymmetric electron beam at least for the considered beam parameters.

3.1.5 Summary

To summarize, we calculate the period of nonlinear betatron oscillations. The method based on the Bessel function expansion has been used in Ref. [Esarey et al., 2002] to calculate the spectrum of the spontaneous emission in ion channel. We have extended that result to the emission at arbitrary directions. The generalized Madey theorem was used to calculate the electron energy gain of ICSRL. The calculation shows that the amplification takes place when the EM wave propagates at small angles with respect to the channel axis. To calculate the radiation spectrum and the gain of ICSRL, we have used a very simple distribution function. Further investigations should include more realistic electron distribution functions. The gain of the ICSRL was calculated in the small-signal small-gain limit. Further investigations are needed to explore the large-gain regime of the ICSRL.

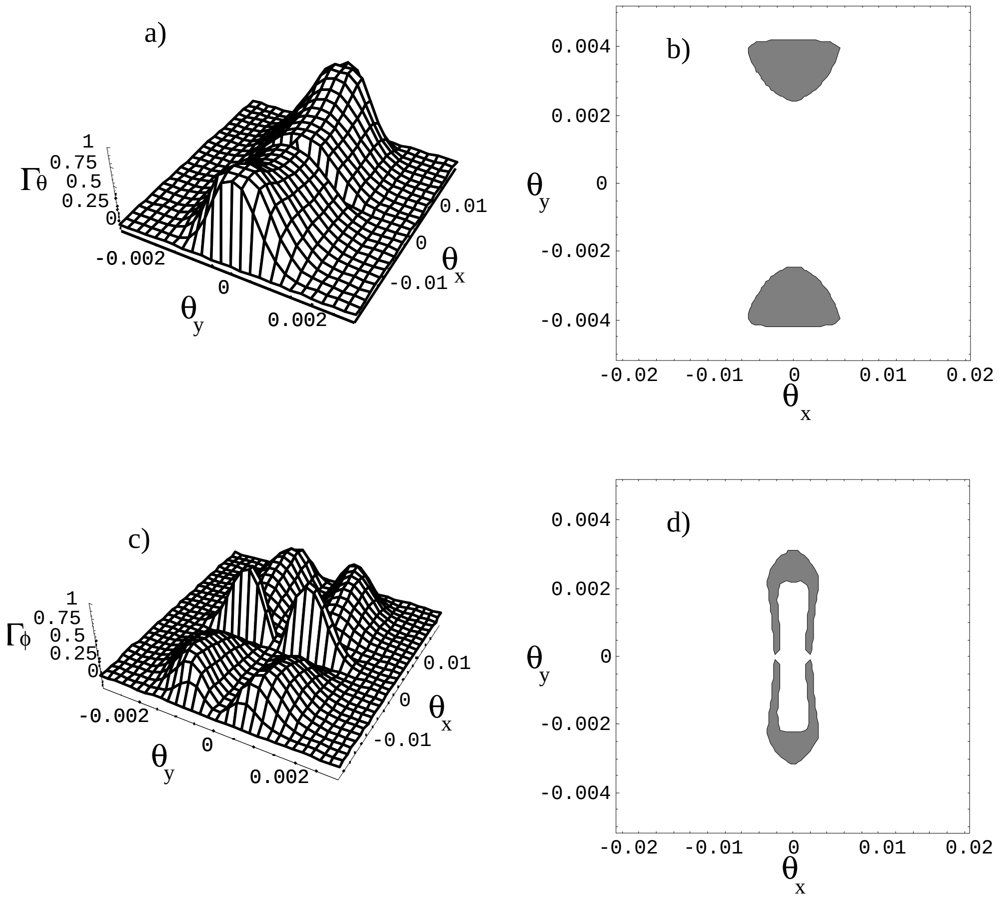

Figure 3.4: **a)** Γ_θ (arbitrary units), for θ-polarized EM wave with $\omega = \omega_c$ versus angles θ_x and θ_y for electrons with $\gamma_z = 500$, $K = p_x = 10$. **b)** The domains of the angles θ_x and θ_y where θ-polarized EM wave with $\omega = \omega_c$ is amplified by the electrons $\Gamma_\theta < 0$, grey region) and where the EM wave is absorbed by the electrons ($\Gamma_\theta > 0$, white region) for $\gamma_z = 500$, $K = p_x = 10$. The angles are given in radians. **c)** Γ_ϕ (arbitrary units), for ϕ-polarized EM wave with $\omega = \omega_c$ versus angles θ_x and θ_y for electrons with $\gamma_z = 500$, $K = p_x = 10$. **d)** The domains of the angles θ_x and θ_y where ϕ-polarized EM wave with $\omega = \omega_c$ is amplified by the electrons ($\Gamma_\phi < 0$, grey region) and where the EM wave is absorbed by the electrons ($\Gamma_\phi > 0$, white region) for $\gamma_z = 500$, $K = p_x = 10$. The angles are given in radians.

3.2 Numerical simulation

3.2.1 Overview

The development of novel high-brightness compact X-ray sources is important for many applications in industry and medicine. Synchrotron light sources (SLSs) are the most intense X-ray sources today. In SLS, the radiation is generated as a result of relativistic electrons scattering by a bending magnet, magnetic undulators or wigglers [Kim, 1989], or by high-power laser pulses (Compton scattering) [Leemans et al., 1997, Schoenlein et al., 2000, Esarey et al., 1993, Pogorelsky, 1998].

The high density of the ions in the channel provides a much higher wiggler strength than that of a conventional magnet wiggler. This leads to a more effective generation of X-ray radiation than in the conventional light sources and could be used for the development of next generation of radiation sources.

An ion channel in plasma can be produced by an electron beam itself. However in this case the plasma density has to be less than the beam density. Unfortunately, the density of a relativistic electron beam cannot be very high because of the technology reasons. This leads to a serious limitation on the gain in the radiated power. The use of a high-power laser could overcome this limitation.

3.2.2 Numerical simulation

The high-power laser pulse can expel plasma electrons by its ponderomotive force and create the ion channel [Key et al., 1998]. Moreover, a strongly nonlinear "bubble" regime has been recently observed in 3D PIC simulations [Pukhov and Meyer-ter-Vehn, 2002]. In this "bubble" regime, the background electrons are completely evacuated from the first half-plasma wave excited behind the laser pulse. The ion density in this "bubble" is many orders of magnitude higher than that in a simple beam-plasma interaction. For example, the ion density in the "bubble" can be as high

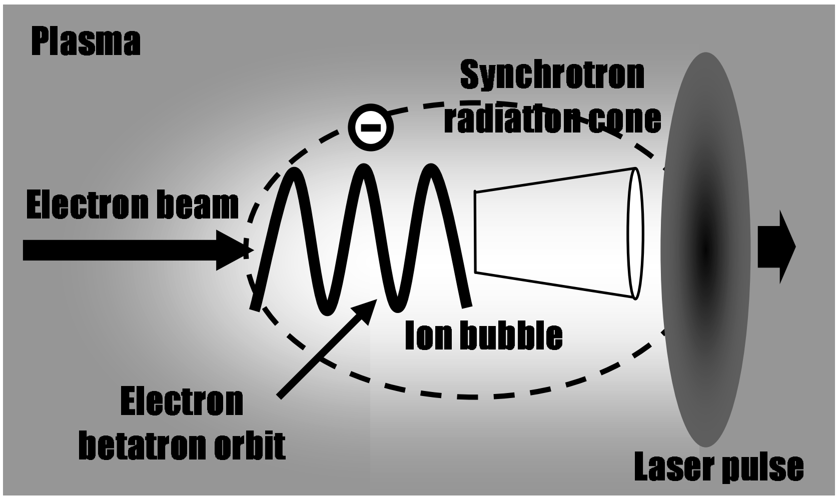

Figure 3.5: Schematic of the spontaneous emission from an electron bunch undergoing betatron oscillations in a laser-produced ion channel.

as $10^{19} cm^{-3}$ [Pukhov and Meyer-ter-Vehn, 2002, Key et al., 1998]. It is 10^5 times higher than that in the beam-plasma experiment recently reported [Wang et al., 2002]. Therefore the radiated power in the laser-produced channel can be 10^{10} times higher. The “bubble” moves with the group velocity of the laser pulse, which is close to the speed of light. A relativistic electron bunch injected into the “bubble” can propagate inside the “bubble” over a very long distance. Hence, in spite of the small length of the “bubble”, the electrons can oscillate in the “bubble” for a long time (see Fig. 3.5, Fig. 3.9).

It has been recently shown by three-dimensional particle-in-cell (PIC) simulations that a dense quasi-monoenergetic bunch of relativistic electrons, collected from the background plasma, can be generated inside the “bubble” [Pukhov and Meyer-ter-Vehn, 2002]. Because of the bubble focusing the bunch has a much higher density than the background plasma. In the present work we show that betatron oscillations of the bunch in the transverse fields of the “bubble” lead to the efficient X-ray generation, which can be used for the developing of table-top high-brightness X-ray radiation sources.

We perform a numerical simulation of the X-ray generation in laser-plasma interactions for the strongly nonlinear broken-wave regime when the "bubble" is formed behind the laser pulse. The incident laser pulse is circularly polarized, has the Gaussian envelope

$$a(t,r) = a_0 \exp\left(-\frac{r_\perp^2}{r_L^2} - \frac{t^2}{T_L^2}\right). \tag{3.81}$$

Here $a = eA/mc^2$ is the relativistic laser amplitude. The wavelength $\lambda = 0.82\mu m$, $r_L = 8.2\mu m$, $T_L = 22fs$, $a_0 = 10$. The laser pulse propagates in a plasma with the density $n_e = 10^{19}cm^{-3}$.

Fig. 3.6 presents snapshots of the laser pulse (the coloured scale) and the electron density (the black/white scale) at different distances. We observed that laser pulse has passed 14 Rayleigh lengths ($Z_R = \pi r_L^2/\lambda$) after the interaction time $T_{int} = 4500\lambda/c$ and lifetime of the "bubble" is about $3500\lambda/c \simeq 10ps$. Electrons, trapped in the "bubble", form the relativistic bunch. We observe as the "bubble" stretches and the bunch elongates with time. Despite the fact that the bunch density is higher than the background ion density, the transverse force acting on the accelerated electrons,

$$F_\perp^2 = F_x^2 + F_y^2, \tag{3.82}$$

is mainly determined by the electrostatic focusing force from the ions, see Fig. 3.7a. This is because the charge force of relativistic electrons and the self-generated magnetic force almost cancel each other [Lawson, 1988]. The energy spectrum of the electron bunch is shown in Fig. 3.7b. We observe formation of the quasi-monoenergetic peak [Pukhov and Meyer-ter-Vehn, 2002]. At $ct = 4000\lambda$ the peak is located at $360MeV$. We calculate the corresponding wiggler strength of $K \simeq 89 \gg 1$. Thus, the electrons emit X-rays in the synchrotron regime. The number of electrons in the bunch is about 6.5×10^{10} at this time. The total energy of electrons of the bunch is about 3.3 J that is about 20% of the laser pulse energy. The number of betatron oscillations experienced by the electrons up

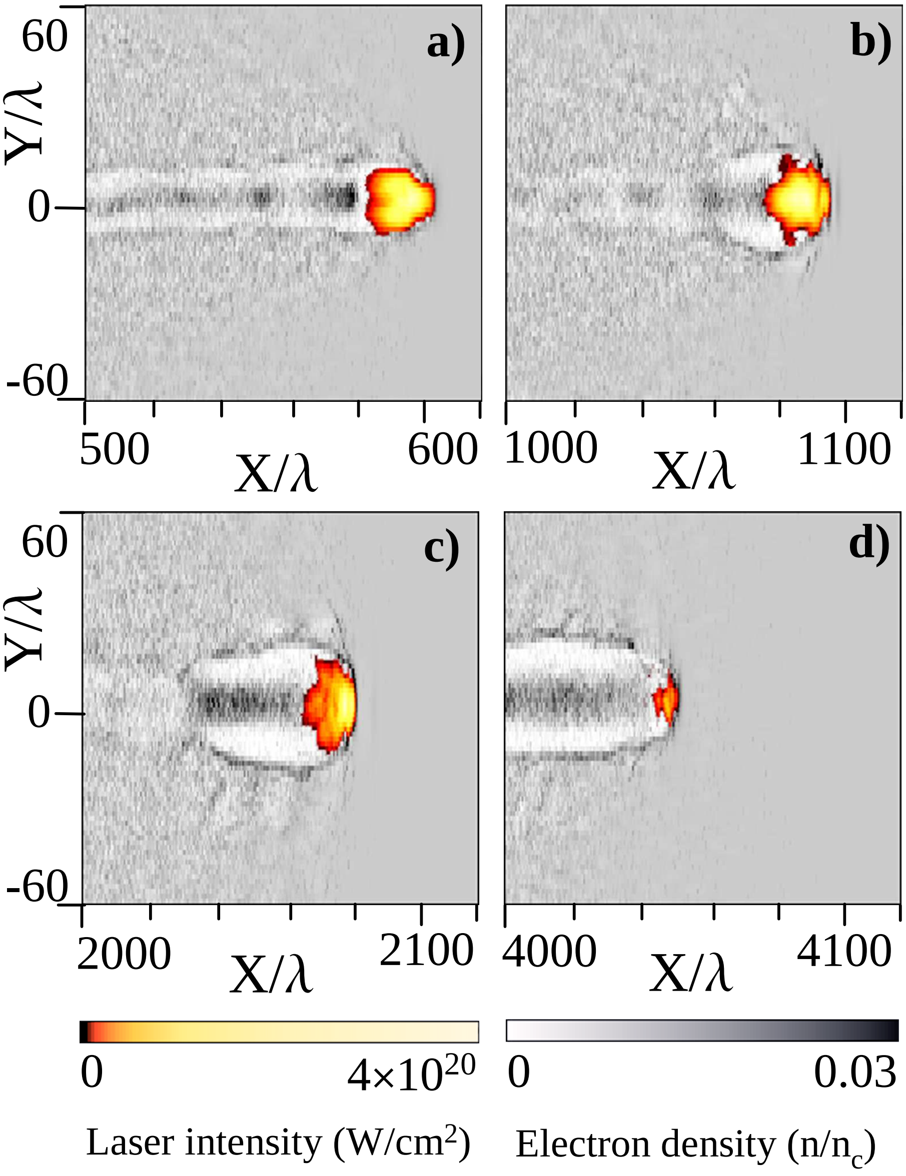

Figure 3.6: The evolution of the laser pulse intensity (the coloured scale) and the “bubble” (the electron density is given in the black/white scale) in the strongly nonlinear broken-wave regime. The laser pulse propagates in a plasma layer from left to right. The plasma density and the laser intensity at **a)** $ct/\lambda = 500$, **b)** $ct/\lambda = 1000$, **c)** $ct/\lambda = 2000$, **d)** $ct/\lambda = 4000$.

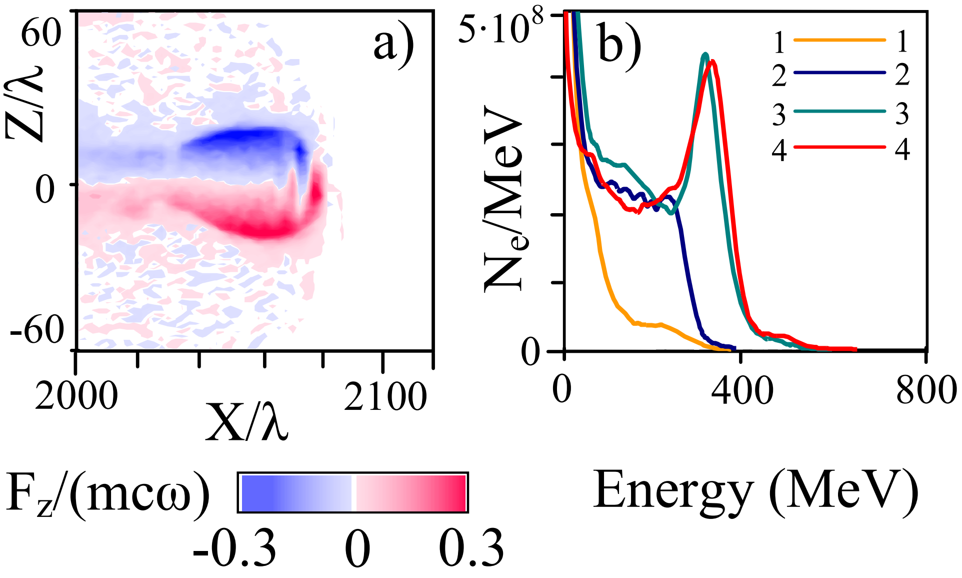

Figure 3.7: **a)** The transversal force acting on the relativistic electrons moving in the x-direction at $ct/\lambda = 2000$. **b)** Temporal variation of the energy spectrum of the electron bunch: (1) $ct/\lambda = 1000$, (2) $ct/\lambda = 2000$, (3) $ct/\lambda = 3000$, (4) $ct/\lambda = 4000$.

to this time was $N_0 = cT_{int}/\lambda_b \simeq 8.6$. To simulate the X-ray generation we suppose that at any given moment of time, the electron emits along its momentum, and the radiation spectrum is defined by $S(\omega/\omega_c)$ (3.1). The critical frequency ω_c is given by

$$\omega_c = \frac{3}{2}\gamma^2\frac{|F_\perp|}{mc}. \tag{3.83}$$

In our PIC code, we follow trajectories of each electron and calculate the emission during the interaction. The emitted radiation exerts a recoil on the electron [Jackson, 1975]. The recoil force (3.7) was included into the equations of electron motion in our simulations.

The synchrotron spectra at $ct = 1000\lambda$ and $ct = 4500\lambda$ are presented in Figs. 3.8 (a, b). The surfaces shown in Figs. 3.8 (a, b) give the number of photons within 0.1% of the bandwidth ($\Delta\hbar\omega = 10^{-3}\hbar\omega$) per solid angle, $2\pi\sin\theta d\theta$: $\tilde{N}_X = \Delta\omega d^2N_X/(2\pi\sin\theta d\omega d\theta)$. It is seen from Fig. 3.8 (b) that the relativistic bunch radiates highly energetic photons within a very narrow cone. The maximum of the radiation spectrum is located at about $50keV$. The analytical estimates for electron energy predict the maximum of $S(x) \simeq 0.3\hbar\omega_c \simeq 55keV$ that is in a good agreement with the numerical simulation data. It is seen from Fig. 3.8 that the radiation from the bunch is confined within the angle $\theta \simeq 0.1rad$ and the theoretical estimate is about $0.2rad$. The photon flux (the number of photons per second in 0.1% bandwidth) and the spectral brilliance of the source at $ct = 1000\lambda$ and $ct = 4500\lambda$ are shown in Figs. 3.8 (c, d). We can estimate the flux and the brilliance using the following formulas.

$$F_X \simeq \frac{S(1)}{S}\left(\frac{\Delta\hbar\omega_c}{\hbar\omega_c}\right)N_X\frac{c}{L_b}, \tag{3.84}$$

where L_b is the bunch length and $S = \int_0^\infty S(x)dx = 8\pi/3^{7/3}$ [Schwinger, 1949]. Assuming that the effective source size of the radiation can be approximated as

$$S_R \simeq \pi\left[r_b^2 + c^2T_{int}^2\theta^2/(4\pi^2)\right] \tag{3.85}$$

where r_b is the bunch radius, we estimate the peak spectral brilliance at

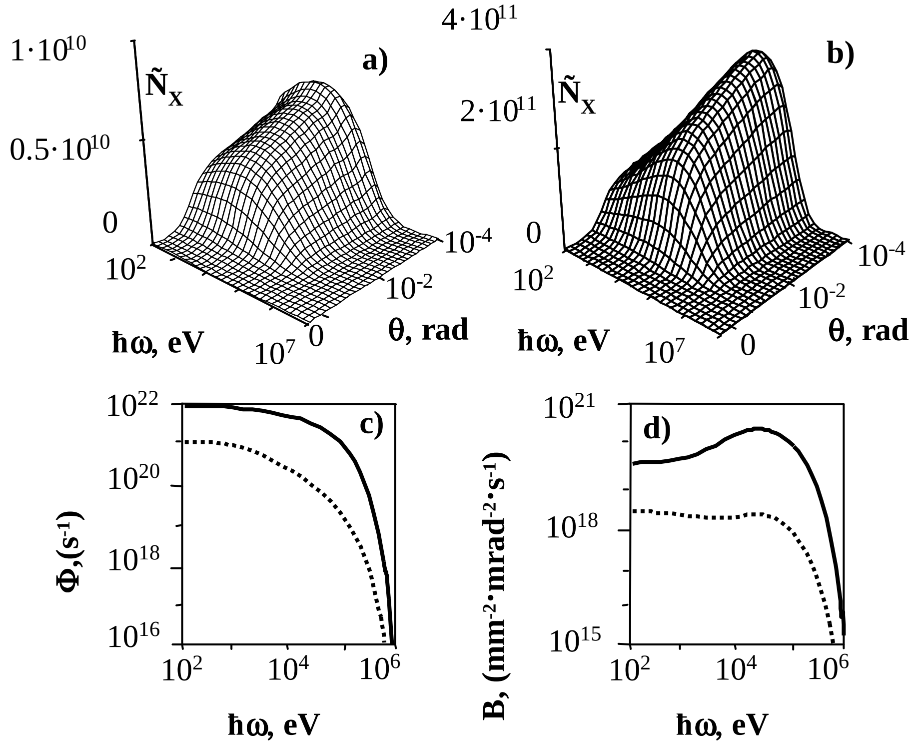

Figure 3.8: **a)** The synchrotron spectrum from the plasma at $ct/\lambda = 1000$, **b)** at $ct/\lambda = 4500$, **c)** the photon flux (the number of photons per second in 0.1% bandwidth), **d)** the spectral brilliance. The dashed line in frames **c)** and **d)** corresponds to $ct/\lambda = 1000$, the solid line corresponds to $ct/\lambda = 4500$.

$\hbar\omega = \hbar\omega_c$ as [Esarey et al., 1993]

$$B_X \simeq \frac{F_X}{4\pi^2\theta^2 S_R^2}. \tag{3.86}$$

To emphasize the advantage of the X-ray generation in the laser-produced ion channel in comparison with that in the self-generated channel, we perform a numerical simulation of the X-ray emission from an external 28.5-GeV electron bunch. The bunch has a diameter $2r_0 = 24.6\mu m$ and a length $L_b = 82\mu m$ with the total charge $Q_b = 5.4nC$. The plasma and laser pulse parameters are the same as in the previous simulation. The electron beam density was much smaller than that of the background plasma, so

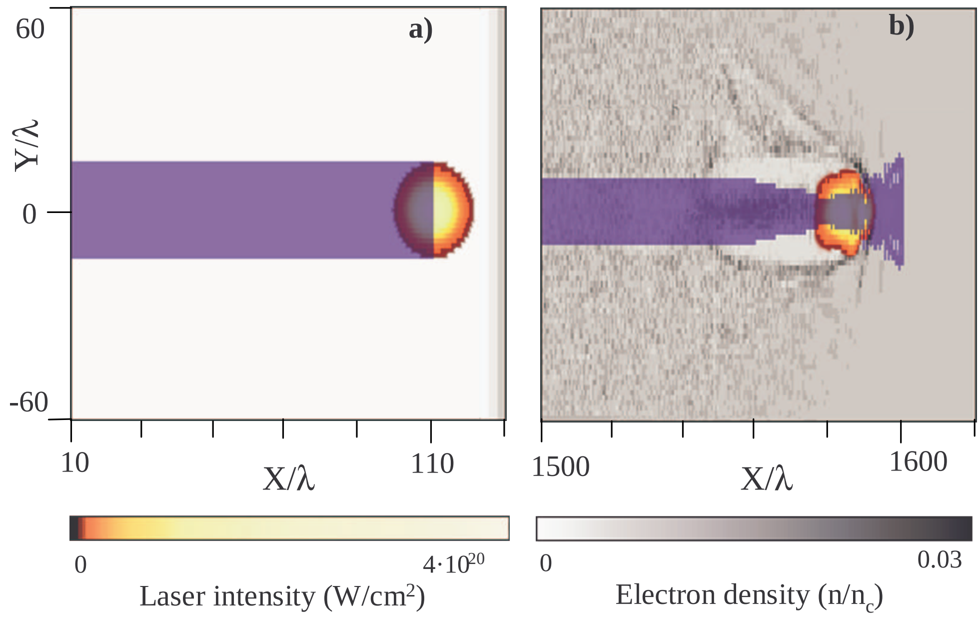

Figure 3.9: Temporal evolution of the plasma density, laser intensity and the envelope of the external 28.5-GeV electron bunch (blue): **a)** at the beginning of interaction and **b)** at $ct/\lambda = 1500$.

that the laser pulse and "bubble" dynamics is not strongly affected by the external electron bunch. At the beginning of interaction the front of the electron bunch is close to the center of the laser pulse (see Figs. 3.9 (a)). The head of the bunch has overtaken the laser center by some 46λ after the interaction time $T_{int} = 4500\lambda/c$. The number of betatron oscillations during the interaction time was $N_0 = cT_{int}/\lambda_b \simeq 1.1$. It is seen from Fig. 3.9 (b) that the laser pulse and the "bubble" remain structurally stable during the full interaction and the bunch is focused at this moment of time.

The synchrotron spectrum after the interaction time $T_{int} = 4500\lambda/c$ is presented in Fig. 3.10 (a). In the present simulation we do not consider the emission from the background plasma electrons. At the given plasma density, the plasma wiggler strength parameter is about $K \simeq 817$. It is seen from Fig. 3.10 (a) that the relativistic bunch radiates highly energetic

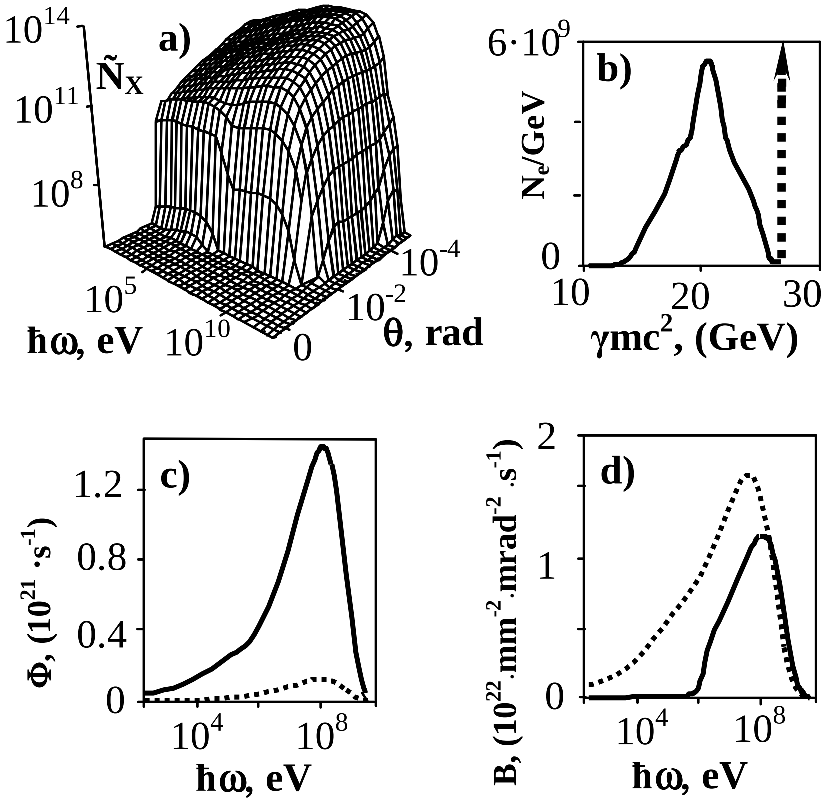

Figure 3.10: **a)** Synchrotron spectrum from the external 28.5-GeV electron bunch at $ct/\lambda = 4500$; **b)** energy distribution of the bunch electrons: the solid line corresponds to $ct/\lambda = 4500$, the dashed arrow marks the initial energy of the electron bunch; **c)** photon flux and **d)** spectral brilliance. The dashed line in frames **c)** and **d)** corresponds to $ct/\lambda = 500$, the solid line corresponds to $ct/\lambda = 4500$.

photons within a very narrow cone. The maximum of the bunch radiation spectrum is located at about $210MeV$. The analytical estimates predict the maximum of $S(x) \simeq 0.3\hbar\omega_c \simeq 385MeV$. The disagreement is caused by the bunch stopping because of the radiation damping force. We also observe a significant photon flux up to the energy of $10GeV$. The radiation from the bunch is confined within the angle $\theta \simeq 10mrad$ that is close to the theoretical estimate $15mrad$. The total number of photons emitted by the bunch are about 2×10^{11}. This means that every electron of the bunch emits about 6 photons. The estimation for the photon number with the critical frequency ω_c is $N_X = N_e \langle N_X \rangle$, where N_e is the number of electrons in the bunch. The estimation is in a good agreement with the numerical simulation results. The bunch lost about one third of its energy after T_{int}. The energy distribution of the bunch electrons after the interaction is shown in Fig. 3.10 (b). The photon flux and the brilliance versus the photon energy are shown in Figs. 3.10 (c,d). The brilliance at the beginning of interaction is slightly higher than at the end because, at the beginning, the bunch is not yet focused and, therefore, emits at small angles. It follows from the Figs. 3.10 (c,d) that the photon energy, flux and brilliance of the X-ray emission from laser-produced ion channel are several orders of magnitude higher than the ones observed in the self-generated ion channel [Wang et al., 2002].

To summarize, we propose compact x-ray radiation source based on the strongly nonlinear broken-wave laser-plasma interaction. While the large size (hundreds meters) of modern x-ray source makes the use of them in industry and medical applications almost impossible, broadband spectrum and small size (several meters) offer outstanding possibilities for the proposed source in of the industry and medicine. The size of the laser-proposed plasma wiggler is in three orders of magnitude less than size of conventional magnetic undulators in proposed schemes of x-ray free electron lasers (FELs) [TESLA, 2001]. The high ion density in the such wiggler provides in several orders of magnitudes larger energies of the x-rays than that of designed FELs and in the recent experiment with self-generated ion channel [Wang et al., 2002]. We also note that the dense relativistic electrons produced by intense laser pulses in the strongly nonlinear regime can be used for X-ray generation via Compton scattering. The incident laser pulse can be split in two pulses. The first pulse can be used to produce the “bubble” and the relativistic bunch, and the second one can collide with the bunch to generate high energetic photons via direct Compton scattering.

3.3 Comparison with an experiment

3.3.1 The Laboratoire d’Optique Appliquée (LOA) experiment

The experiment was done by Kim Ta Phuoc, Fréderic Burgy, Jean-Philippe Rousseau, Victor Malka, and Antoine Rousse. Here has been shown experimentally that synchrotron radiation, based on betatron oscillation of relativistic electrons, can be produced efficiently from the interaction of an intense laser and a plasma both used to accelerate and wiggler the electron bunch (Fig. 3.11). Three important conditions must be achieved simultaneously in the plasma for that purpose. First, the electrons must be accelerated at relativistic energies for which $\gamma \gg 1$, where γ is the Lorentz relativistic factor of the electron. Second, they must propagate in an ion channel (plasma wiggler) over large distances (few millimeters). And third, the strength parameter K of the plasma wiggler must exceed unity to reach the synchrotron regime. Those conditions are satisfied in the strongly non-linear broken wave regime observed recently from 3D Particle In Cell (PIC) simulations [Pukhov and Meyer-ter-Vehn, 2002]. In this regime, the plasma wave excited behind the laser pulse transforms into a “bubble” moving forward with the group velocity of the laser pulse close to the speed of light. Inside the “bubble”, almost free from background electrons and where the ion density is as high as $10^{19} cm^{-3}$, a dense bunch of electrons can be trapped and accelerated up to 100 MeV. These relativistic electrons

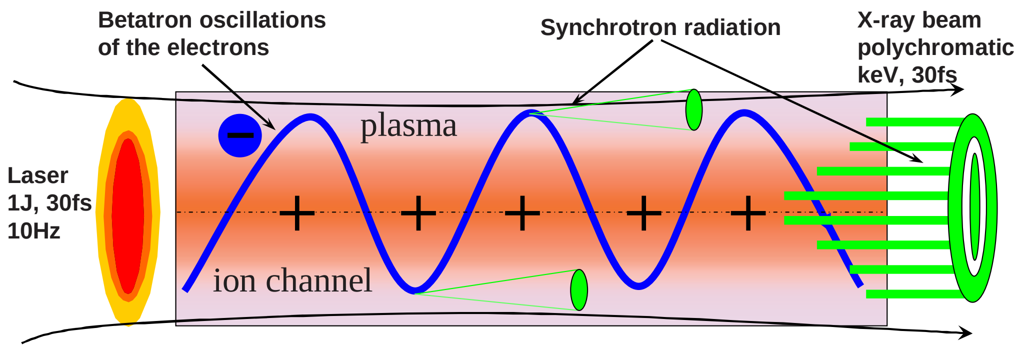

Figure 3.11: Schematic representation of the synchrotron x-ray source based on the betatron oscillation of relativistic electrons in a laser-produced plasma channel. At the laser focus, where the intensity is $I \sim 10^{19} W/cm^2$, the ponderomotive force of the laser expels the electrons from the axis. This results in the generation of an ion channel in the wake of the laser pulse. Inside the channel, a bunch of electrons is trapped and accelerated up to $100 MeV$. While the electrons experience the transverse electrostatic field, they make betatron oscillations and emit a femtosecond and collimated beam of synchrotron radiation in the x-ray region.

make betatron oscillations in the transverse field of the "bubble" and emit synchrotron radiation. The characteristics of the radiation strongly depend on the amplitude r_0 of the betatron oscillation. For small amplitude and near axis oscillations, the radiation is emitted at the fundamental wavelength given by

$$\lambda = \lambda_b / \left(2\gamma^2\right), \tag{3.87}$$

where λ_b is the betatron wavelength. When the amplitude of the betatron oscillation becomes large, high harmonics are radiated and the resulting broadband spectrum is extended up to a critical energy

$$\hbar\omega_c \,[\mathrm{keV}] = 5 \times 10^{24} \gamma^2 n_e \left[\mathrm{cm}^{-3}\right] r_0 \,[\mu\mathrm{m}] \tag{3.88}$$

after which it drops exponentially. n_e is the electron density of the plasma and ω_c is the critical frequency. The radiation is emitted in the forward direction within a cone of angle K/γ, where

$$K = 2\pi \left(\gamma r_0\right) / \lambda_b = 1.33 \times 10^{-10} \gamma^{0.5} n_e^{0.5} \left[\mathrm{cm}^{-3}\right] r_0 \,[\mu\mathrm{m}]\,. \tag{3.89}$$

The average number of photons with the mean energy $\hbar\omega_c$ emitted by one electron is

$$N_\times = 5.6 \times 10^{-3} N_0 K, \tag{3.90}$$

where N_0 is the number of betatron oscillations accomplished by the electron.

The experiment was performed at the LOA using a titanium-doped sapphire (Ti:Sa) laser operating at 10 Hz with a wavelength λ_0 of 820 nm in chirped-pulse amplification mode [Pittman et al., 2002]. The laser delivered energies up to 1 J on target in 30-fs full width at half-maximum (FWHM) pulses, with a linear horizontal polarization. The laser beam was focused with an f/18 off-axis parabolic mirror onto the edge of a supersonic helium gas jet (diameter 3 mm). The neutral-density profile jet was characterized by interferometry and shows high uniformity throughout the jet as well as sharp edge. The laser distribution at full energy in the focal plane was a Gaussian with a waist w_0 of $18\mu m$ containing 50% of the total laser energy. This produces vacuum-focused intensities I_L on the order of $3 \times 10^{18} W/cm^2$, for

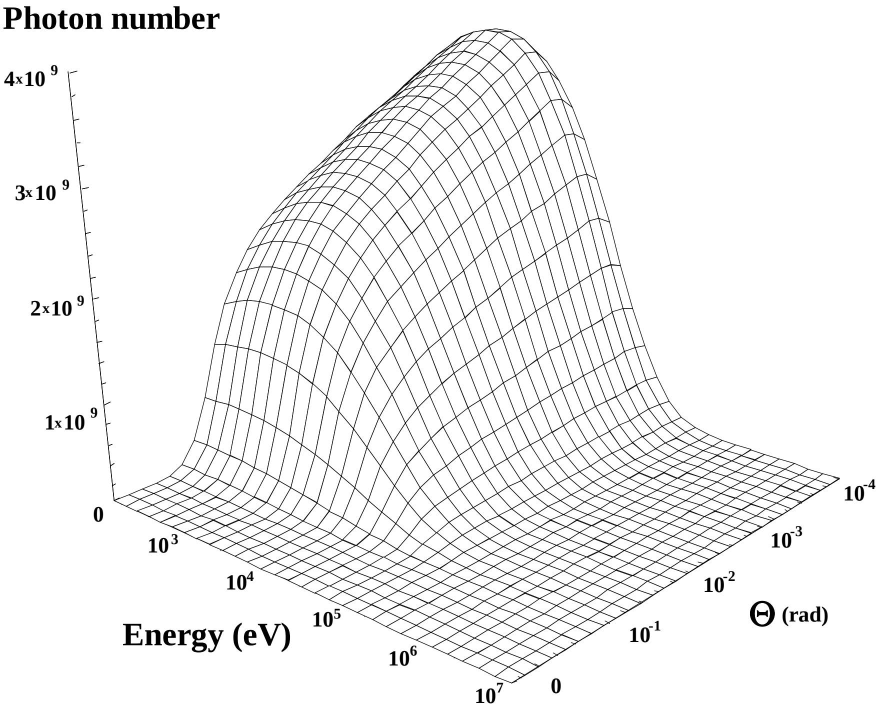

Figure 3.12: The numerically predicted synchrotron spectrum from the plasma with density $n_e = 1 \times 10^{19} W/cm^2$ after $3mm$ propagation distance. The distribution gives the number of x-ray photons emitted within 0.1% of the energy bandwidth ($\Delta\hbar\omega = 10^{-3}\hbar\omega$) per solid angle, $2\pi \sin\theta d\theta$.

which the corresponding normalized vector potential a_0 is 1.2. The electron plasma density was varied between $2\times10^{18}cm^{-3}$ and $6\times10^{19}cm^{-3}$, which was achieved by varying the backing pressure on the gas jet. In this experiment, the electrons accelerated in the forward direction were characterized using a magnetic electron spectrometer covering energies from 0 to 217 MeV. Finally, the interaction and the laser propagation in the plasma were characterized using side, top, and 45° Thomson scattering imaging as well as time resolved shadowgraphy.

The x-ray radiation produced in the plasma was measured using a cooled x-ray CCD camera placed directly on axis without any focusing x-ray optic (Fig. 3.13). For all the measurement a $25\mu m$ Beryllium filter, blocking any radiation below 0.8 keV, was placed in front of the CCD camera. In order to minimize the noise level on the detector, 0.5 Tesla permanent magnets were placed along 20 centimeters between the plasma and the x-ray CCD to deviate the accelerated charged particles on-axis. In addition, a 5 cm lead shielding with a few millimeters vertical aperture for the x-ray signal was used to isolate the CCD camera from radiation coming from any sources but the plasma. A Nickel mesh with $41\mu m$ wire diameter and 80% open area was placed in the x-ray beam to discriminate the x-ray signal from the residual noise. Indeed, this mesh is transparent for the electrons with energy above 100 keV (electrons with energy below 100 keV are deviated by the permanent magnet and can not be detected on the CCD camera) and blocks the x-rays with energy below 10 keV. In addition, the mesh was used as a knife edge to perform a transverse source size measurement. Careful tests were done with magnets (orientation) and reflecting x-ray optics (metallic Nickel mirror at grazing incidence) to rule out the electrons as the origin of the observed signal. The spectrum of the radiation was estimated using an additional set of Aluminium, Nickel and Copper filters.

In the experiment, x-rays from 1 keV to 4 keV have been detected. The back-illuminated CCD which is not sensitive to x-rays energies above 8 keV did not allow a full spectral characterization of the radiation. The

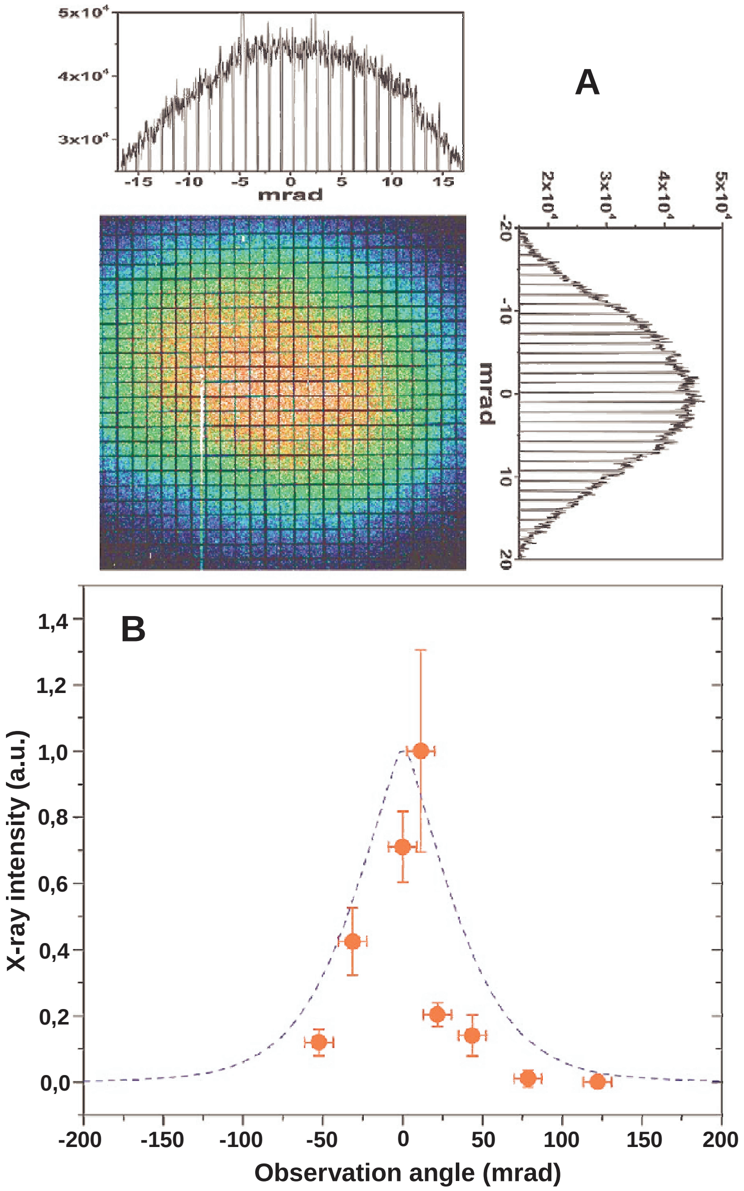

Figure 3.13: Angular distribution of the radiation for x-ray integrated energies beyond 1 keV (taken from [Phuoc et al., 2005]). (A) Beam profile of the x-ray beam at $n_e = 8 \times 10^{18} cm^{-3}$ and the corresponding lineout graphics. (B) Angular distribution of the x-ray intensity for $n_e = 1.1 \times 10^{19} cm^{-3}$ (dashed line). The x-ray intensity has been normalized.

total number of photons integrated over the bandwidth of the filters is more than 10^8 photons per shot and integrated over all angles, which is in close agreement with the result expected from the simulation (Fig. 3.12). Thanks to the vertical aperture made in the lead shielding, the spatial distribution of the x-ray beam in the vertical plane was obtained at each shot. The CCD image on Fig. 3.13 clearly shows that the radiation is collimated in a narrow cone centered on the laser axis. Large fluctuations of the divergence of the beam shot to shot (40%) were observed during the experiment. The most collimated x-ray beam was recorded at $20\,mrad$ at full width at the half-maximum (FWHM). On the other hand, the horizontal angular distribution was obtained by rotating the x-ray CCD as well as the lead shielding around the gas jet. In both planes the x-ray beam divergence, averaged over more than 10 shots, is found to be $\Delta\theta = 50 \pm 20\,mrad$ at FWHM. These experimental results are in a good agreement with the angular widths expected from the numerical simulations (Fig. 3.12).

The intensity of the x-ray signal is sharply peaked at an electron density of $5 \pm 1 \times 10^{18}\,\mathrm{cm}^{-3}$ (Fig. 3.14). Below this critical density, the x-ray signal vanishes mainly because the number of trapped electrons is too low. This is confirmed in the experiment for which no electrons were detected by the spectrometer in that case. At larger densities up to $1.2 \times 10^{19}\,\mathrm{cm}^{-3}$, the x-ray signal drops down and a plateau is reached. For these experimental conditions, the resulting plasma wave is too weak because the plasma period becomes non-resonant with the temporal laser pulse length. The pulse must be first modulated and additional laser energy would be needed. The numerical simulations clearly reproduce this experimental behavior (Fig. 3.14): a sharp increase of the x-ray intensity followed by a smoother decrease of the signal. However, we can note that the critical density is found to be four times higher than in the experiments. The most plausible explanation is a mismatch between the expected and experimental laser pulse duration.

As it is usually the case in plasma physics, other radiative processes

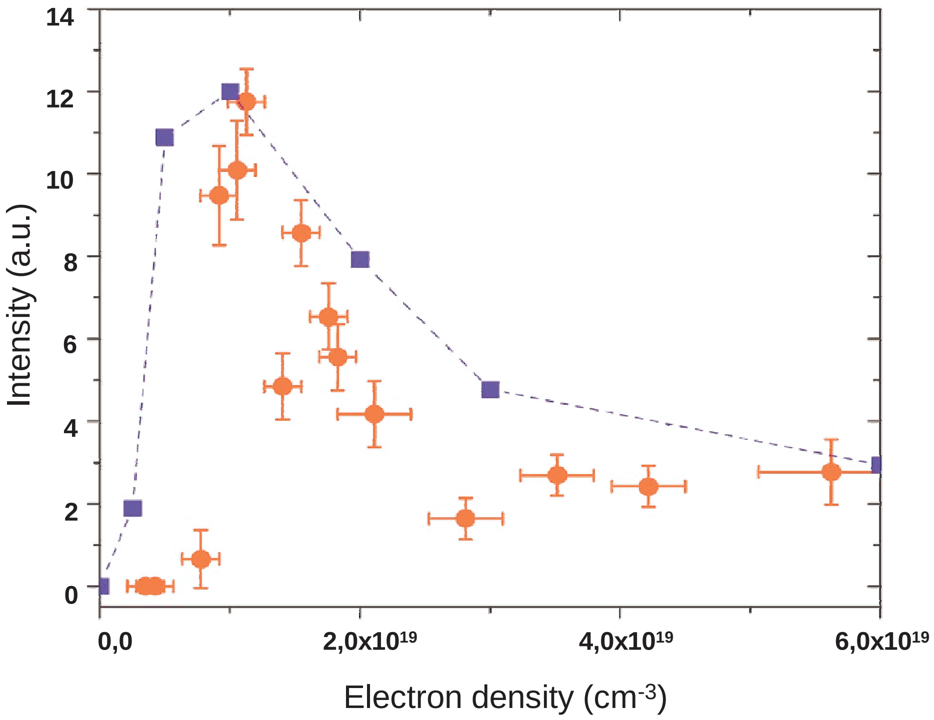

Figure 3.14: X-ray signal as a function of the plasma electron density for x-ray energies beyond $1\,keV$. Each data point corresponds to an average value over ten shots. The square along the dotted line corresponds to the results obtained using a 3D PIC simulation.

having similar characteristics, like the nonlinear Thomson scattering or the relativistic Bremsstrahlung radiation could contribute to the overall x-ray emission. The nonlinear Thomson scattering of relativistic electrons oscillating in the laser field and accelerated in the forward direction is expected to be peaked close to 100 eV. This radiative process can not produce efficient keV radiation unless $a_0 \sim 10$ can be reached, which is far above the laser intensity used in our experiment. We have also shown in a previous study that the expected collimation should be one order of magnitude broader in that case. On the other hand, the relativistic Bremsstrahlung could generate a collimated angular distribution as well. However, it is expected to produce less than 10^6 photons/shot in the full x-ray spectrum extending up to a few MeVs. Those processes can safely be ruled out as participating to the hard x-ray radiation observed in the present parameter regime.

This compact laser-produced plasma synchrotron source provides unique capabilities: a beam of x-rays, a broad spectrum and an ultrashort pulse duration. The pulse duration must be in the order of the electron bunch duration, which is close or less than the laser pulse duration (30 fs). The transverse size of the radiation source coming from the plasma, measured with a knife edge technique, is $20\mu m \times 20\mu m$. The average brightness is then found to be $5 \times 10^6 ph/s/mm^{-2}/mrad^{-2}/0.1\%BW$ while the peak spectral brightness is $2 \times 10^{20} ph/s/mm^{-2}/mrad^{-2}/0.1\%BW$. The x-ray flux could be further enhanced by increasing the propagation length of the "bubble" and therefore the number N_0 of betatron oscillations experienced by the accelerated electrons. In this experiment, the simulation shows that the "bubble" subsists in only 1 mm within the 3 mm of the gas jet which allows the accelerated electrons to experience 5 betatron oscillations. The x-ray energy can be extended to harder x-rays by increasing the strength parameter K of the plasma wiggler (K=21 in the experiment). Higher laser energy as well as more energetic electrons will be required for those purposes. Like every all-optical schemes, such radiation is perfectly synchronized with the laser system to do visible pump-x-ray probe experiments with no timejitter. Its reasonable flux ($5 \times 10^6 photons/pulse/s/0.1\%BW$) makes possible multiple-Bragg and absorption x-ray experiments which will significantly extend the first x-ray diffraction studies already demonstrated in ultrafast x-ray science [Rischel et al., 1997, Rousse et al., 2001].

Chapter 4

Electron Beam Filamentation

4.1 Overview

The understanding of the transport of high energy electrons through matter is of fundamental importance, in particular for the fast ignitor concept relevant for laser fusion. In this scheme the ignition of the pre-compressed pellet of the fusion fuel is initiated by laser produced electrons with energies in the MeV range [Tabak et al., 1994]. The main advantage of fast ignition in contrary to direct or indirect drive is significantly relaxed symmetry requirements on the implosion and the achievement of higher gain [Tabak et al., 1994, Kidder, 1976, Atzeni and Ciampi, 1997, Kodama et al., 2001]. It is crucial for this scheme that the energy of the ignition laser is efficiently converted into an electron beam that can propagate through the high density overcritical plasma and initiate the thermonuclear burn in the pre-compressed core [Deutsch et al., 1996]. Measurements show that up to 50% of the laser energy can be transferred into kinetic energy of fast electrons [Hatchett et al., 2000].

The transport of the electrons to the pre-compressed core involves currents of the order of 100-1000 MA through regions of overdense plasma. These currents exceed the critical Alfvén limit given by

$$J_A = 17.1\beta\gamma\,[kA]\,, \tag{4.1}$$

where $\beta = v/c$ and γ is the relativistic Lorentz factor [Alfvén, 1939]. This is only possible when return currents which are formed by the thermal background electrons of the plasma play a significant role in neutralization.

Under these conditions, i.e. in presence of a large flow of fast electrons and a counter-streaming flow of cold electrons, kinetic instabilities like the Weibel instability [Weibel, 1959] can grow. 3D PIC simulations have clearly predicted that the transport of the relativistic electron beam is not homogeneous, but filamentary structures will occur and magnetic fields up to 100 MG surround the filaments [Taguchi et al., 2001, Pukhov, 2003]. The arrangement of the filaments propagating through the region of overdense plasma is of great interest because it determines the amount of energy that can be deposited in the fuel. It has however been predicted that processes like collective stopping of the hot electrons, coalescence of the current filaments and energy dissipation due to heating of the surrounding plasma can play a significant role and are connected to the electric and magnetic fields of the current filaments [Honda et al., 2000, Sentoku et al., 2002]. Therefore the understanding of the underlying propagation mechanisms of the relativistic electrons through overdense plasma is essential for the success of the fast ignitor scheme.

4.2 Numerical simulation and comparison with an experiment

A number of experiments investigating the propagation and filamentation of laser produced relativistic electron beams have been performed using metal and plastic foils or glass slabs [Tatarakis et al., 1998, Zheng et al., 2004, Hall et al., 1998, Teng et al., 2003, Fuchs et al., 2003, Santos et al., 2002]. In such experiments with solid targets it is difficult to create homogeneous plasmas by pre-ionization before the main interaction. Furthermore, present PIC-simulations are inadequate to simulate electron propagation through solid densities since these plasmas are highly collisional and the transport is over long distances, typically hundreds of microns. Foam targets offer a different approach where electron beam propagation can be studied over relatively long distances at lower densities.

Here we make a comparison an experimental data and simulations. We use one tenth of solid density pre-ionized CH-foam targets. This approach provides well controlled conditions for electron beam propagation through dense, homogeneous plasmas over long distances. The electrons exiting the rear surface of the target were diagnosed by imaging the optical transition radiation (OTR) and synchrotron radiation with high spatial resolution. The images show filamentary structures with a scale length of a few microns. These filaments are organized in a ring like structure of larger filaments around the center, surrounded by a cloud of several smaller filaments. A detailed analysis has been performed using 3D PIC simulations to calculate the electron energy distribution. The propagation of the electron beam through the dense plasma was then simulated. The numerical results clearly show filamentary structures and are in good agreement with the experimental data.

The experimental measurements were carried out at the Vulcan Petawatt Laser Facility at the Rutherford Appleton Laboratory. A $350J$ laser pulse at $1053nm$ and $750fs$ in duration was focussed with an $f/3.2$ parabola onto low density foam targets with various thicknesses incident at 45 degrees, obtaining a reproducible focal spot of $6\mu m$ in diameter that contains about 75% of the laser energy. The rear side of the target was imaged with an $f/2$ lens system with a focal length of $f = 100mm$ onto two cameras with Ilford HP5 film. The magnification was 40×. Spectra of the light emitted were recorded with an optical spectrometer operating at the central wavelength of $527nm$ and detected with a 16-bit CCD camera. Stray light of the Petawatt infrared laser beam was blocked using KG5 filters. The spectral sensitivity range of the imaging system was 400 to $700nm$. To achieve high resolution, the spectral window of one of the two cameras used was limited to a bandwidth of $\Delta\lambda = 10nm$ around the central wavelength of the second harmonic of the laser at $527nm$ using an interference filter. The second camera integrated over the visible spectral range.

Multilayered foam targets with a cell size of $1\mu m$ were used. The density was chosen as 100 and $200mg/cm^3$. The thicknesses were 250, 500 and $750\mu m$. The front side of the foams was overcoated with a layer of $75nm$ of gold to produce x-ray radiation for pre-ionization by the leading edge of the laser pulse. The rear side of the targets was overcoated with $200nm$ of aluminium to obtain a sharp density gradient important for the OTR technique [Ginzburg and Tsytovich, 1990] and blocked the light emitted by the pre-plasma. The direct propagation of optical radiation of the laser beam was effectively prevented by the density of the plasma and the long target thicknesses as well as the additional aluminium coating at the rear side.

In addition, the energies of the electrons emitted at the rear side of the target were measured with a permanent-magnet electron spectrometer [Norreys et al., 2004] along the axis of the laser beam. The distance from the target to the $5mm$ diameter collimator is $3.7m$, resulting in a solid angle of $1.4 \cdot 10^{-6} sr$. The electron spectra were recorded on Fujifilm image plates.

Fig. 4.1 shows typical electron spectra obtained for different target conditions. A two temperature Boltzmann distribution was seen with a “hot” temperature of around $T_h \approx 9MeV$ and a “cold” temperature of $T_c \approx 3MeV$.

The optical spectra and the comparison of the images with and without the bandpass filter showed that the emission collected by the optics is peaked significantly around the second harmonic of the laser frequency due to coherent transition radiation or coherent synchrotron radiation. The bandwidth of the peak is $\Delta\lambda_p = 4nm$ (FWHM) (in comparison the laser spectral bandwidth is $\Delta\lambda_L = 2.2nm$). The coherence of the emission is also confirmed as in some of the images an interference pattern is observed. This indicates that the electrons are basically accelerated in bunches twice per optical cycle ω_0 of the Petawatt laser pulse. This is in agreement with observations by other experiments [Santos et al., 2002, Baton et al., 2003, Cowan et al., 2000]. Thus the bunches of electrons producing the filamentary

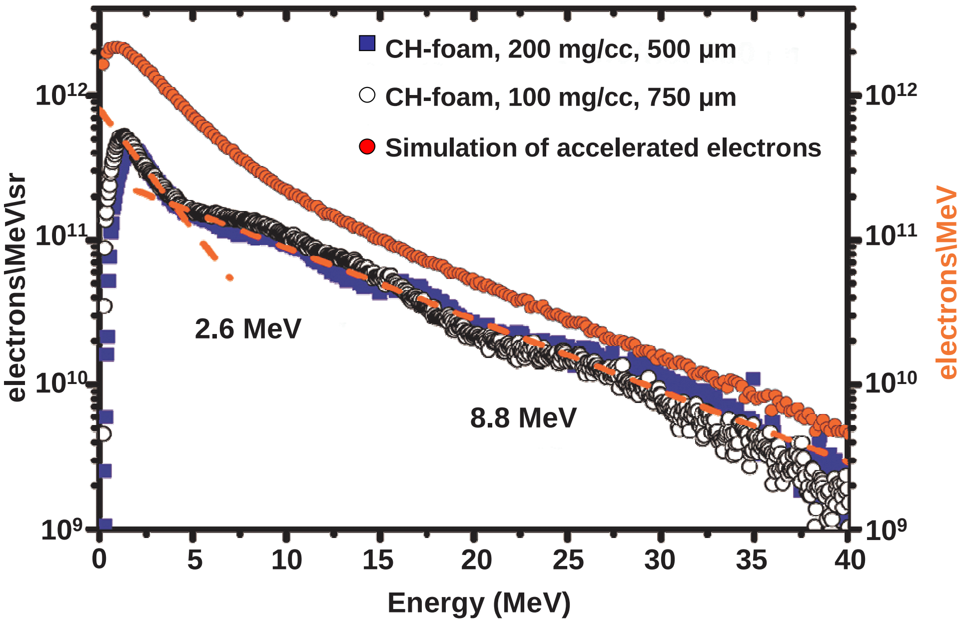

Figure 4.1: Electron spectra measured for different foam target conditions and spectrum obtained from the simulation for similar target and laser conditions (total number per MeV).

structures are supposed to be accelerated by the laser ponderomotive force. At high relativistic intensities the Lorenz force $-e\vec{v} \times \vec{B}$ acting on electrons quivering in the laser field expels them in the longitudinal direction.

Since further acceleration mechanisms such as resonant absorption and direct laser acceleration are known to accelerate electrons to high relativistic energies, we calculated the effective temperatures for the conditions defined by our laser parameters. According to the model given by [Wilks et al., 1992] the laser ponderomotive force will lead to an effective temperature of

$$T_{pm} = 0.511 \cdot \left[\left(1 + I_{18} \lambda_L^2 / 1.37 \right)^{1/2} - 1 \right] \text{MeV} \tag{4.2}$$

while resonance absorption will contribute to a Boltzmann distribution with a temperature given by [Beg et al., 1997]

$$T_{res} = 0.1 \cdot \left(I_{17} \cdot \lambda_L^2 \right)^{1/3} \text{MeV} \tag{4.3}$$

with λ_L as the wavelength of the accelerating laser pulse (in μm, I_{17} and I_{18} denotes the intensity in terms of 10^{17} and $10^{18} W/cm^2$ respectively). The latter equation is only valid for $p-$polarized radiation (as was the case in the experiment). The difference between both mechanisms is basically that the oscillating component of the ponderomotive force will accelerate bunches of electrons twice every laser cycle, while only once per cycle in resonance absorption. Also it is well known that electrons accelerated by resonance absorption of the laser pulse will be directed perpendicular to the target surface (due to the direction of the density gradient), while the laser ponderomotive force at high intensities accelerates electrons along the laser propagation axis [Beg et al., 1997, Malka and Miquel, 1996, Santala et al., 2000]. Because of the spectral window of the imaging optics, the light observed can be ascribed to electrons undergone ponderomotive laser acceleration. We compared the temperatures measured with those predicted according to equation (4.2) and (4.3): The intensity on the different targets was between 3.5 and $5 \cdot 10^{20} W/cm^2$, that leads to T_h between 7.5 and $9.3 MeV$ and $T_c \approx 2 MeV$. The measured values are close to the estimated ones. This is again an indication that the “hot” electrons are accelerated by ponderomotive forces of the laser pulse.

A typical optical image taken on a foam target is shown in Fig. 4.2(a). The thickness was $250\mu m$. A filamentary spot like-structure is clearly observed. A central bright spot is surrounded by a cloud of smaller filamentary structures. As shown in the inset, in the center larger spots forming one half of a ring are found. The ellipticity of the rings observed can be explained by taking into account the oblique incidence of the laser pulse while the diagnostics imaged normal to the target’s surface. This gives further evidence that the filaments observed are basically produced by electrons pushed in the laser direction by the laser ponderomotive force. Under the assumption that the electrons are emitted under an angle of 42 to 45 degree [Sheng et al., 2000], the widths of the images have to be rescaled using a factor of $\sim 0,75$. This results that the inner and outer ring form concentric circles. This is shown in Fig. 4.2(b). The diameter of the inner ring is about $60\mu m$ with spot sizes of $\sim 10\mu m$ in diameter (FWHM). The outer ring has a diameter of $\sim 140\mu m$ and the size of smallest observable filaments is $< 3\mu m$. An analysis of the divergence of the inner and the outer structure reveals that the global spot size diverges under a full opening angle of $\sim 17^o$ with increasing target thickness.

The experimental data were simulated with the 3D PIC code Virtual Laser Plasma Laboratory (VLPL) [Pukhov, 1999]. In a first step we have used a laser pulse with the Gaussian profile

$$a = a_0 \exp(-(t/T)^2 - (r/R)^2) \cos[\omega_0(t - cz)], \tag{4.4}$$

where $a_0 = 15$, $T = 314\omega_0^{-1}$ and $R = 63c/\omega_0$. The laser was normally incident onto a plasma layer with a linear density ramp reaching the maximum $N_{\max} = 20N_c$ over the distance $L = 300c/\omega_0$, where $N_c = \omega_0^2 m/4\pi e^2$ is the critical density. The linear density ramp was used to mimic the pre-plasma at the target surface. The spectrum of accelerated electrons is shown in Fig. 4.1. The calculated spectrum consists of two Boltzmann-like energy distributions with $T_{eff} \approx 8MeV$ and $3.5MeV$.

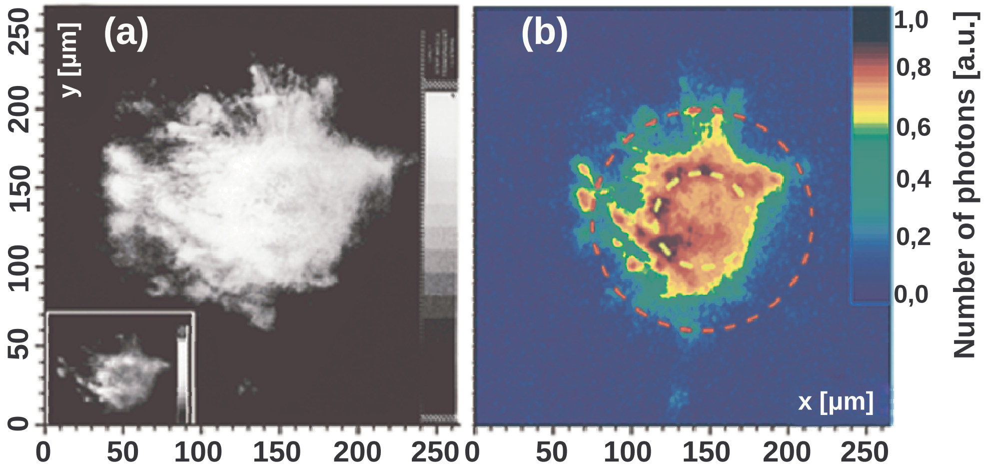

Figure 4.2: Data obtained using 250μm foam target [Jung et al., 2005]. (a) Picture of optical emission with 2ω bandpass filter used. The inset shows a picture recorded with the second camera without bandpass but gray filters. As the optical density is different, the substructure of the inner circle is clearly revealed. (b) Reprocessed data. Two concentric rings with 140μm (red) and 60μm (yellow) are drawn.

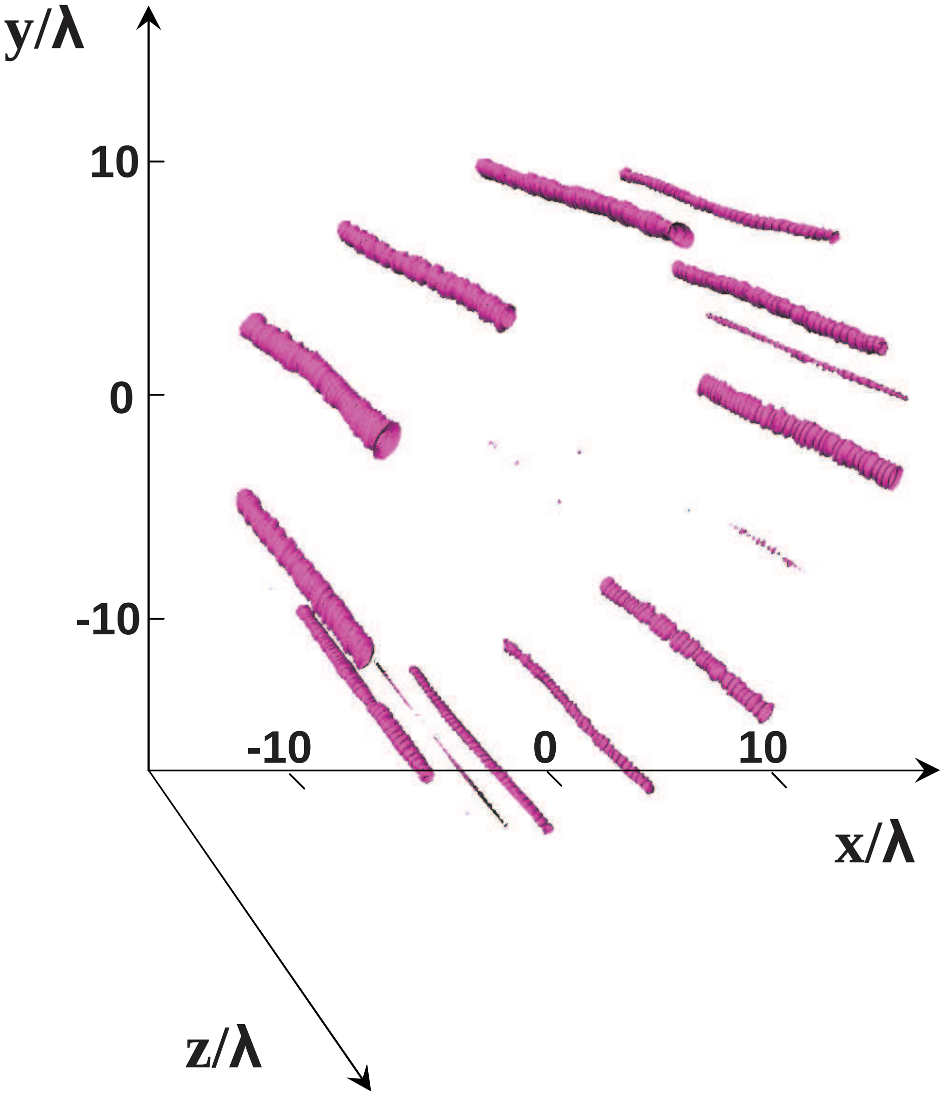

Figure 4.3: 3D PIC simulation result of electron density after $100\mu m$ propagation. A dozen of dense filaments can be observed.

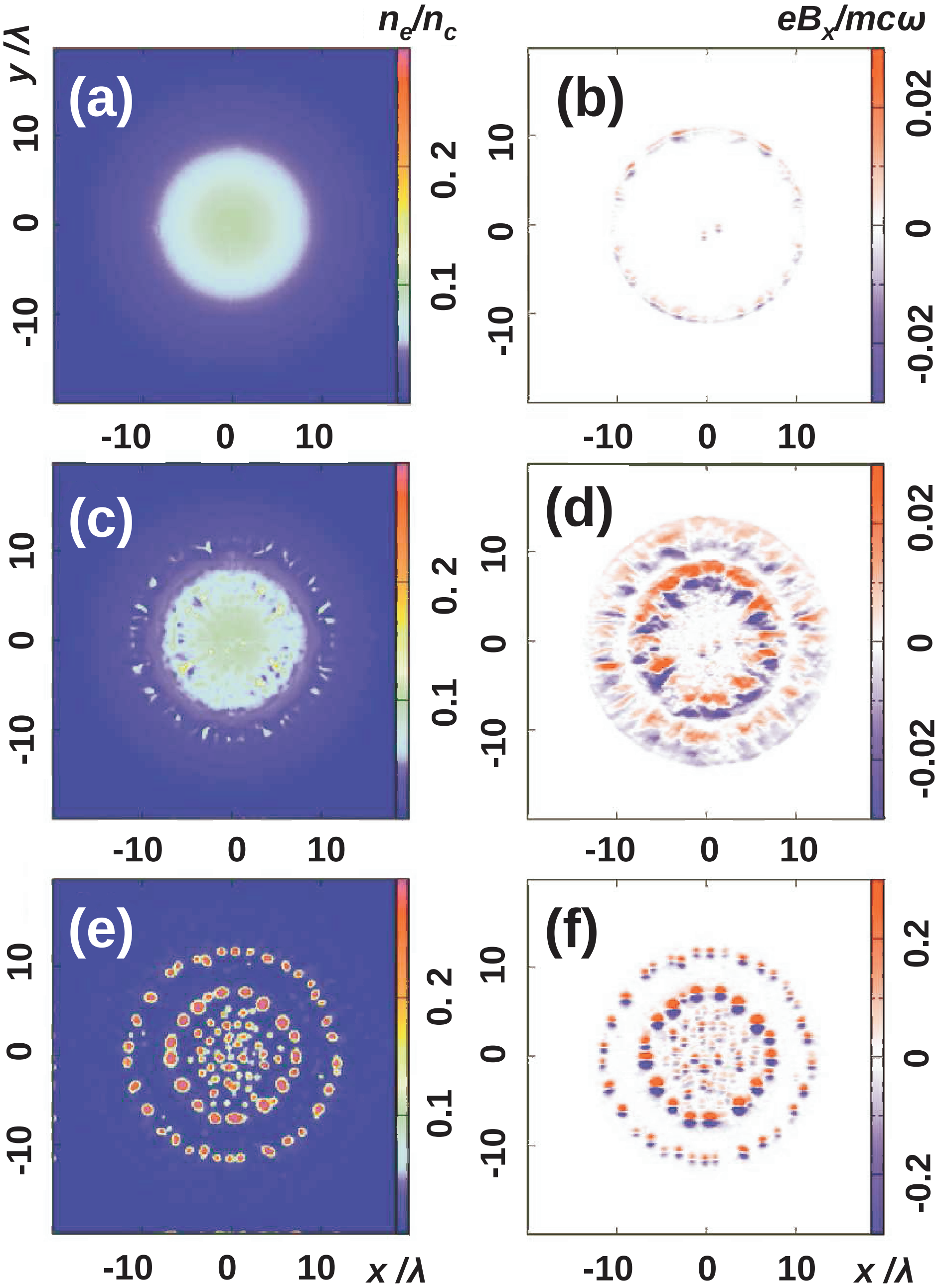

Figure 4.4: Simulation of electron density of hot electrons after 10, 20 and $100\mu m$ propagation ((a), (c) and (e)) and x-component of magnetic field surrounding the filaments ((b), (d) and (f)).

In a second step, an electron beam with a Boltzmann energy distribution ($T_{eff} \approx 7.5MeV$) was injected into a plasma with $N_e = 30N_c$ and its propagation was studied. The transverse electron beam temperature was set to zero to avoid the beam divergence and to keep the beam within the simulation box. The size of the simulation box is limited because of the computational power restrictions. Initially, the electron beam had a smooth Gaussian transverse density profile with radius $R_b = 10\mu m$ and a peak density of $N_b = 0.1N_c$. This beam transports the power

$$P_b = \gamma N_b mc^3 \cdot \pi R_b^2 \approx 14[\mathrm{TW}] \tag{4.5}$$

and the current

$$J = N_b ec \cdot \pi R_b^2 \approx 10J_A \approx 2[\mathrm{MA}]. \tag{4.6}$$

The electron beam current is significantly above the Alfvén limit and the beam quickly begins to filament. 3D PIC simulation result presents on Fig. 4.3. It can be observed a dozen of dense filaments. Each of them carries an Alfvén current. Fig. 4.4 show transverse cuts of the electron density and the $x-$component of the quasi-static magnetic field after the beam has propagated 10, 20 and $100\mu m$ through the foam plasma. The onset of the filamentation is observed at a radius $\sim R_b$ after the beam has propagated about $10\mu m$ (Fig. 4.4(a) and (b)). This can be explained with small perturbations in the magnetic repulsion of the counter-streaming beams. At $20\mu m$, strong magnetic fields at a radius $r \approx 7\mu m$ are observed and cause the inner part of the beam also to filament (Fig. 4.4(c) and (d)). This leads to the occurrence of the inner current filaments observed. Then some of the filaments begin to merge while the ring like geometry survives. The ring like structure is clearly revealed in Fig. 4.4(e) and (f). Here the beam has propagated over $100\mu m$. Note that a similar ring structure has been observed in the experiment.

According to analytical predictions, filamentation due to the Weibel instability is expected to grow on a time scale of the plasma frequency of the relativistic electron beam,ω_{be}, and the growth rate of the instability,

$$\gamma_{inst} \approx \omega_{be}\,[N_b/(\gamma N_e)]\,v/c,$$

scales with the beam contrast N_b/N_e, where N_e is the density of the surrounding plasma [Honda et al., 2000]. Using $N_b = 0.1N_c, N_e = 30N_c$, and $v \sim c$, and estimating the growth rate of the Weibel instability, one obtains $\gamma_{inst}^{-1} \sim 130\,fs$. This corresponds to a beam propagation distance of about $40\,\mu m$ which is of the same order as that observed in the simulation. Each small filament in Fig. 4.4(e) and Fig. 4.3 carries a current smaller than the limiting Alfven current J_A and is surrounded by the self-generated magnetic field. The B_x-field reaches $30MG$ (Fig. 4.4(f)). Thus we assume that it is this magnetic field that leads to beam filamentation due to the Weibel instability.

To summarize, we have studied the electron beam propagation through overdense plasmas using one tenth of solid density pre-ionized CH-foam targets. High resolution images of the optical radiation emitted by MeV electrons at the rear side have been taken. The optical emission is ascribed either to coherent transition radiation or coherent synchrotron radiation produced by electron bunches generated by the laser ponderomotive force twice per optical cycle. The measured electron temperatures correlate strongly with the acceleration mechanisms discussed. It is observed that the electron beam breaks up into filaments. The filaments form two concentric rings. Comparison with the 3D-PIC simulations show that filamentation is due to the Weibel instability.

Chapter 5

Conclusions

5.1 Electron acceleration in the "bubble" regime

We have studied the electron trapping and acceleration in the "bubble" regime of laser-plasma interaction. Because of the very complex nature of the ultra-relativistic laser-plasma interactions, our analysis was a phenomenological one. Yet, we were able to calculate electromagnetic fields inside the spherical cavity moving in plasma with a relativistic velocity. The cavity runs in the plasma with velocity that is close to the speed of light while the ions inside the cavity are immobile. The calculated fields are in a good agreement with the ones obtained in the direct numerical simulation. At the beginning of the interaction the "bubble" shape is determined by the laser pulse. However, the length and the transverse radius of the "bubble" are determined by the electron bunch, when the bunch charge becomes large. We provide estimates for the "bubble" size in the both regimes.

A plasma cavity which has the potential (2.34) with $R > \gamma_0$ can trap plasma electrons. This is an essentially multidimensional effect because the electron has to reach the large transverse momentum $p_\perp \sim \gamma_0$ to be trapped. A small cavity generated by the laser pulse can trap the plasma electrons because of the wavebreaking. Wavebreaking occurs in the region where

$0 < \Phi < 1$. Only a small fraction of the sheath electrons, which reach the wavebreaking region, can be trapped. The estimate for the trapping cross-section is obtained in terms of the "bubble" radius and the electron sheath width. The estimate is close to the value of the trapping cross-section observed in the PIC simulation.

The electron dynamics of the electron bunch in the "bubble" is studied. It is shown that the cavity elongation has to be taken into account in order to estimate the maximum energy gain of the electron bunch. The adiabatic description can be used to describe the transversal dynamics of the bunch electron. Making use of the trapping cross-section the bunch density is estimated.

Finally, we have developed a phenomenological theory of the ultrarelativistic laser-plasma interaction in the "bubble" regime. Of course, it contains a number of fitting parameters. Yet, it helps to understand deeper the very complex physics of this new regime.

5.2 Betatron radiation

We have studied spontaneous and stimulated emission from electrons undergoing betatron motion in ion channel. We calculate the period of nonlinear betatron oscillations. The method based on the Bessel function expansion has been used in Ref. [Esarey et al., 2002] to calculate the spectrum of the spontaneous emission in ion channel. We have extended that result to the emission at arbitrary directions. The generalized Madey theorem was used to calculate the electron energy gain of ICSRL. The calculation shows that the amplification takes place when the EM wave propagates at small angles with respect to the channel axis.

Our analysis shows that the radiation amplification may be possible for appropriately tailored electron beams. Particularly, a narrow electron beam could be injected off-axis such that all the beam electrons execute approximately the same betatron orbit. To calculate the radiation spectrum and the gain of ICSRL, we have used a very simple distribution function. Further investigations should include more realistic electron distribution functions. The gain of the ICSRL was calculated in the small-signal small-gain limit. Further investigations are needed to explore the large-gain regime of the ICSRL.

We propose an X-ray radiation source based on the laser-produced ion channel. The high ion density in the channel leads to a much higher power of the X-ray spontaneous emission than that in a self-generated channel.

5.3 Electron beam filamentation

We have studied the electron beam propagation through overdense plasmas using one tenth of solid density pre-ionized CH-foam targets. High resolution images of the optical radiation emitted by MeV electrons at the rear side have been taken. The optical emission is ascribed either to coherent transition radiation or coherent synchrotron radiation produced by electron bunches generated by the laser ponderomotive force twice per optical cycle. The measured electron temperatures correlate strongly with the acceleration mechanisms discussed. It is observed that the electron beam breaks up into filaments. The filaments form two concentric rings. Comparison with the 3D-PIC simulations show that filamentation is due to the Weibel instability.

Appendix A

Size of the Wavebreaking Pattern

At the beginning of the interaction (see Chapter 2, Sec. 2.1.6, Fig. 2.4) the wavebreaking region is located exactly on the x-axis. The laser ponderomotive potential is low here and can be neglected. We use the one-dimensional cold fluid approximation to estimate the scale of this region. The one-dimensional approach as an estimation can be used here because $p_\perp \approx \partial p_\perp / \partial r_\perp \approx E_\perp \approx \partial E_\perp \partial r_\perp \approx 0$ at the $x-$axis. The hydrodynamic approach fails when the wavebreaking occurs. However we assume that the structure of the nonlinear plasma wave is not yet strongly destroyed at the beginning of the interaction, as it is seen in the PIC simulation, Fig. 2.4c. The equation for the potential of the one-dimensional nonlinear plasma wave is [Akhiezer and Polovin, 1956, Sprangle et al., 1990, Teychenne et al., 1993]

$$\frac{d^2\Phi}{d\xi^2} = \frac{v_0 - \Phi\sqrt{\Phi^2 - \gamma_0^{-2}}}{v_0\left(\Phi^2 - \gamma_0^{-2}\right) + \Phi\sqrt{\Phi^2 - \gamma_0^{-2}}}, \tag{A.1}$$

where $p_\perp = p_y = 0$ is assumed.

An analysis of Eq. (A.1) shows that $\Phi_{\min} < \Phi < \Phi_{\max}$, where $\Phi_{\min} \simeq \Phi_{\max}^{-1}$ in the limit $\Phi_{\max} \gg 1$ [Teychenne et al., 1993]. The singularity appears in the right-hand side of Eq. (A.1) in the limit $\Phi_{\max} = \gamma_0$. This means the plasma wavebreaking and the failure of the cold fluid approach [Teychenne et al., 1993, Sprangle et al., 1990]. We assume that the “bubble” velocity is close to the group velocity of the laser pulse $\gamma_0 \simeq 13$ at the beginning of interaction. It follows from Eq. (2.16) that $\Phi_{\max} \simeq R^2/4$. The first integral given by Eq. (A.1) in the limit $1 \ll 1/\Phi_{\min} \simeq \Phi_{\max}$ and $\Phi < 1$, $\gamma_0 \gg 1$ reduces to the form

$$\left(\frac{d\Phi}{d\xi}\right)^2 \simeq \frac{1}{\Phi_{\min}} - \frac{1}{\Phi}. \tag{A.2}$$

Integrating Eq. (A.1) from 1 to $\Phi_{\min}$ we find the width of the wavebreaking region

$$D/2 \simeq \Phi_{\max}^{-1/2}. \tag{A.3}$$

We get $D \simeq 0.6$ for $R \simeq 7$ from Eq. (A.3) that is about two times smaller than the value of the pattern width observed in the PIC simulation at $l_{int} = 25$. It follows from the Hamiltonian (2.30) that

$$\gamma \simeq \gamma_0^2 \Phi_{\max}^{-1} \left(1 - \sqrt{1 - \Phi_{\max}^2 \gamma_0^{-2}}\right). \tag{A.4}$$

Eq. (A.1) gives $\gamma \simeq 7$ that is two time smaller than $\gamma_0 \simeq 13$. To derive a more accurate estimation for D and γ one needs a solution of a three-dimensional nonlinear equation on the plasma wave [Lotov, 1998].

Appendix B

Trajectory Divergence

The potential Φ is almost constant in the electron sheath and we use the equipotential approximation to analyse the electron motion in the sheath. We get from Eq. (2.30)

$$\gamma - v_0 p_x = \Phi \simeq const. \tag{B.1}$$

Then, Eqs. (2.25) and (2.27) reduces to the form

$$\frac{dP_x}{dt} \simeq \frac{dp_x}{dt} \simeq -\frac{\xi}{2}, \tag{B.2}$$

$$\frac{d\xi}{dt} = \frac{p_x}{\Phi + v_0 p_x} - v_0 \simeq -\frac{v_0 \Phi}{\Phi + v_0 p_x}, \tag{B.3}$$

where we the Lorentz force is taken in the form (2.33) and $p_x \ll \gamma_0^2$ is assumed. The obtained system of equations has the first integral

$$\frac{\xi^2 - \xi_0^2}{4} \simeq \Phi \ln \left(\Phi + v_0 p_x\right), \tag{B.4}$$

where the initial conditions $-\xi = -\xi_0 \gg 1$, $y = y_0$ and $p_x = 0$ are assumed and Φ is of the order of unity in the electron sheath and outside of the wavebreaking pattern.

The return current ends at the point $\xi = \xi_0$ within the electron sheath (see Fig. B.1).

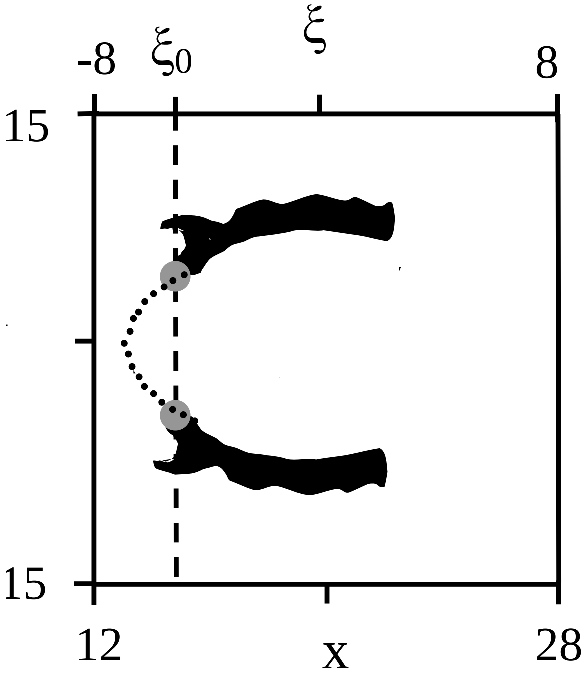

Figure B.1: Results of the PIC simulation when the laser pulse has passed about $25c/\omega_p$. The dark-shaded regions show the return current location (the places, where $p_x < 0$) in the plane $z = 0$. The cavity boundary is shown by the dashed line. The gray circles are the region where $p_x \simeq 0$. The coordinates are given in c/ω_p.

Using Eqs. (B.1) and (B.4) we get

$$\gamma \simeq \exp\left(\frac{\xi^2-\xi_0^2}{4\Phi}\right), \quad p_y \simeq -\sqrt{2\Phi\gamma}, \tag{B.5}$$

where $\gamma \gg 1$ is assumed. Eq. (2.28) can be rewritten in the form

$$\frac{dy}{d\xi} = \frac{dy}{dt}\left(\frac{d\xi}{dt}\right)^{-1} = \frac{p_y}{p_x - v_0\gamma} \simeq \sqrt{\frac{2\gamma}{\Phi}}. \tag{B.6}$$

Integrating the obtained equation in the limit $|\xi_f - \xi_0| \ll |\xi_0|$ we find the shape of plasma cavity from the point, where the return current is over ($\xi = \xi_0$), to the cavity base ($\xi = \xi_f$) in the limit $\gamma \gg 1$

$$\ln\left[\frac{\xi_0\,(y-y_0)}{4\sqrt{2\Phi}}\right] \simeq \frac{\xi_0\,(\xi-\xi_0)}{4\Phi}. \tag{B.7}$$

Making use of Eq. (B.7) the distance between two electrons can be evaluated

$$\delta R \simeq \frac{4\sqrt{2\gamma}}{\xi_0}\left(\frac{1}{2\sqrt{\Phi}} - \frac{\xi_f-\xi_0}{4\Phi^2}\right)\frac{\partial\Phi}{\partial y}\delta\rho, \tag{B.8}$$

where $\delta\rho \ll 1$ is the initial distance between the two electrons. As $\Phi \sim 1$ and $\partial\Phi/\partial y = F \sim -\xi_0$ the trajectory divergence can be estimated as

$$\eta = \left|\frac{\delta R}{\partial\rho}\right| \simeq 4\sqrt{2\gamma}\,(\ln\sqrt{\gamma} - 1/2)\,. \tag{B.9}$$

Then the trajectory divergence between the point $\xi = \xi_0$ in the electron sheath, where $p_x = 0$, and the wavebreaking pattern ($\xi = \xi_f$) is

$$\eta \simeq 2R\ln\left(\frac{R}{2\sqrt{2}}\right). \tag{B.10}$$

Here we have used $\gamma \simeq \Phi_{\max}/2 \simeq R^2/8$. This follows from Eq. (A.4) in the limit $\Phi_{\max}^2\gamma_0^2 \ll 1$.

Index

Bibliography

[Abramowitz and Stegun, 1972] Abramowitz, M. and Stegun, I., eds (1972). Handbook of Mathematical Functions. New York: Dover.

[Akhiezer and Polovin, 1956] Akhiezer, A. and Polovin, R. (1956). Zhurnal Eksperimental'noi i Teoreticheskoi Fiziki 30, 915. Sov. Phys. JETP 3, 696 (1956).

[Alfvén, 1939] Alfvén, H. (1939). Physical Review 55, 425.

[Amiranoff et al., 1998a] Amiranoff, F., Baton, S., Bernard, D., Cros, B., Descamps, D., Dorchies, F., Jacquet, F., Malka, V., Marques, J. R., Matthieussent, G., Mine, P., Modena, A., Mora, P., Morillo, J., and Najmudin, Z. (1998a). Physical Review Letters 81 (5), 995–998.

[Amiranoff et al., 1998b] Amiranoff, F., Bernard, D., Cros, B., Dorchies, F., Jacquet, F., Malka, V., Marques, J., Matthieussent, G., Mine, P., Modena, A., Morillo, J., and Najmudin, Z. (1998b). Nuclear Instruments and Methods in Physics Research 410A, 364.

[Amiranoff et al., 1992] Amiranoff, F., Laberge, M., Marques, J. R., Moulin, F., Fabre, E., Cros, B., Matthieussent, G., Benkheiri, P., Jacquet, F., Meyer, J., Mine, P., Stenz, C., and Mora, P. (1992). Physical Review Letters 68 (25), 3710–3713.

[Andreev et al., 1992] Andreev, N., Gorbunov, L., Kirsanov, V., Pogosova, A., and Ramazashvili, R. (1992). Pis'ma v Zhurnal Eksperimental'noi i Teoreticheskoi Fiziki 55, 551. JETP Lett. 55, 571-576(1992).

[Antonsen and Mora, 1992] Antonsen, T. M. and Mora, J. P. (1992). Physical Review Letters 69 (15), 2204–2207.

[Atzeni and Ciampi, 1997] Atzeni, S. and Ciampi, M. (1997). Nuclear Fusion 37, 1665.

[Baton et al., 2003] Baton, S. D., Santos, J. J., Amiranoff, F., Popescu, H., Gremillet, L., Koenig, M., Martinolli, E., Guilbaud, O., Rousseaux, C., Gloahec, M. R. L., Hall, T., Batani, D., Perelli, E., Scianitti, F., and Cowan, T. E. (2003). Physical Review Letters 91 (10), 105001.

[Bauer et al., 1995] Bauer, D., Mulser, P., and Steeb, W.-H. (1995). Physical Review Letters 75 (25), 4622–4625.

[Beg et al., 1997] Beg, F. N., Bell, A. R., Dangor, A. E., Danson, C. N., Fews, A. P., Glinsky, M. E., Hammel, B. A., Lee, P., Norreys, P. A., and Tatarakis, M. (1997). Physics of Plasmas 4 (2), 447–457.

[Clayton et al., 2002] Clayton, C. E., Blue, B. E., Dodd, E. S., Joshi, C., Marsh, K. A., Mori, W. B., Wang, S., Catravas, P., Chattopadhyay, S., Esarey, E., Leemans, W. P., Assmann, R., Decker, F. J., Hogan, M. J., Iverson, R., Raimondi, P., Siemann, R. H., Walz, D., Katsouleas, T., Lee, S., and Muggli, P. (2002). Physical Review Letters 88 (15), 154801.

[Clayton et al., 1985] Clayton, C. E., Joshi, C., Darrow, C., and Umstadter, D. (1985). Physical Review Letters 54 (21), 2343–2346.

[Cowan et al., 2000] Cowan, T. E., Hunt, A. W., Phillips, T. W., Wilks, S. C., Perry, M. D., Brown, C., Fountain, W., Hatchett, S., Johnson, J., Key, M. H., Parnell, T., Pennington, D. M., Snavely, R. A., and Takahashi, Y. (2000). Physical Review Letters 84 (5), 903–906.

[Davidson, 2001] Davidson, R. (2001). Physics of Nonneutral Plasmas. London: Imperial College Press.

[Deutsch et al., 1996] Deutsch, C., Furukawa, H., Mima, K., Murakami, M., and Nishihara, K. (1996). Physical Review Letters 77 (12), 2483–2486.

[Dodin and Fisch, 2003] Dodin, I. Y. and Fisch, N. J. (2003). Physical Review E (Statistical, Nonlinear, and Soft Matter Physics) 68 (5), 056402.

[Esarey et al., 1997] Esarey, E., Hubbard, R. F., Leemans, W. P., Ting, A., and Sprangle, P. (1997). Physical Review Letters 79 (14), 2682–2685.

[Esarey and Pilloff, 1995] Esarey, E. and Pilloff, M. (1995). Physics of Plasmas 2 (5), 1432–1436.

[Esarey et al., 1993] Esarey, E., Ride, S. K., and Sprangle, P. (1993). Physical Review E (Statistical Physics, Plasmas, Fluids, and Related Interdisciplinary Topics) 48 (4), 3003–3021.

[Esarey et al., 2002] Esarey, E., Shadwick, B. A., Catravas, P., and Leemans, W. P. (2002). Physical Review E (Statistical, Nonlinear, and Soft Matter Physics) 65 (5), 056505.

[Esarey et al., 1996] Esarey, E., Sprangle, P., Krall, J., and Ting, A. (1996). IEEE Transactions on Plasma Science 24, 252.

[Everett et al., 1994] Everett, M., Lal, A., Gordon, D., Clayton, C., Marsh, K., and Joshi, C. (1994). Nature 368, 527.

[Faure et al., 2004] Faure, J., Glinec, Y., Pukhov, A., Kiselev, S., Gordienko, S., Lefebvre, E., Rousseau, J., Burgy, F., and Malka, V. (2004). Nature 431 (7008), 541 – 544.

[Fraiman and Kostyukov, 1995] Fraiman, G. M. and Kostyukov, I. Y. (1995). Physics of Plasmas 2 (3), 923–934.

[Fuchs et al., 2003] Fuchs, J., Cowan, T. E., Audebert, P., Ruhl, H., Gremillet, L., Kemp, A., Allen, M., Blazevic, A., Gauthier, J.-C., Geissel, M., Hegelich, M., Karsch, S., Parks, P., Roth, M., Sentoku, Y., Stephens, R., and Campbell, E. M. (2003). Physical Review Letters 91 (25), 255002.

[Fung, 1969] Fung, P. (1969). Plasma Physics 11, 285.

[Gahn et al., 1999] Gahn, C., Tsakiris, G. D., Pukhov, A., ter Vehn, J. M., Pretzler, G., Thirolf, P., Habs, D., and Witte, K. J. (1999). Physical Review Letters 83 (23), 4772–4775.

[Geraci and Whittum, 2000] Geraci, A. A. and Whittum, D. H. (2000). Physics of Plasmas 7 (8), 3431–3440.

[Ginzburg and Tsytovich, 1990] Ginzburg, V. and Tsytovich, V. (1990). Transition Radiation and Transition Scattering. Bristol: Hilger.

[Ginzburg and Zhelenyakov, 1958] Ginzburg, V. and Zhelenyakov, V. (1958). Astron. Zh. 35, 694.

[Hairapetian et al., 1995] Hairapetian, G., Davis, P., Clayton, C. E., Joshi, C., Hartman, S. C., Pellegrini, C., and Katsouleas, T. (1995). Physical Review Letters 72, 2403.

[Hall et al., 1998] Hall, T. A., Ellwi, S., Batani, D., Bernardinello, A., Masella, V., Koenig, M., Benuzzi, A., Krishnan, J., Pisani, F., Djaoui, A., Norreys, P., Neely, D., Rose, S., Key, M. H., and Fews, P. (1998). Physical Review Letters 81 (5), 1003–1006.

[Hatchett et al., 2000] Hatchett, S. P., Brown, C. G., Cowan, T. E., Henry, E. A., Johnson, J. S., Key, M. H., Koch, J. A., Langdon, A. B., Lasinski, B. F., Lee, R. W., Mackinnon, A. J., Pennington, D. M., Perry, M. D., Phillips, T. W., Roth, M., Sangster, T. C., Singh, M. S., Snavely, R. A., Stoyer, M. A., Wilks, S. C., and Yasuike, K. (2000). In: Electron, photon, and ion beams from the relativistic interaction of Petawatt laser pulses with solid targets volume 7 pp. 2076–2082, Seattle, Washington (USA): AIP.

[Heitler, 1954] Heitler, W. (1954). The Quantum Theory of Radiation. London: Oxford University Press.

[Honda et al., 2000] Honda, M., Meyer-ter-Vehn, J., and Pukhov, A. (2000). Physical Review Letters 85 (10), 2128–2131.

[Jackson, 1975] Jackson, J. (1975). Classical Electrodynamics. New York: Wiley.

[Joshi et al., 2002] Joshi, C., Blue, B., Clayton, C. E., Dodd, E., Huang, C., Marsh, K. A., Mori, W. B., Wang, S., Hogan, M. J., O'Connell, C., Siemann, R., Watz, D., Muggli, P., Katsouleas, T., and Lee, S. (2002). In: High energy density plasma science with an ultrarelativistic electron beam volume 9 pp. 1845–1855, Long Beach, California (USA): AIP.

[Joshi et al., 1987] Joshi, C., Katsouleas, T., Dawson, J., Yan, Y., and Slater, J. (1987). IEEE Journal of Quantum Electronics 23, 1571.

[Jung et al., 2005] Jung, R., Osterholz, J., Lowenbruck, K., Kiselev, S., Pretzler, G., Pukhov, A., Willi, O., Kar, S., Borghesi, M., Nazarov, W., Karsch, S., Clarke, R., and Neely, D. (2005). Physical Review Letters 94 (19), 195001.

[Key et al., 1998] Key, M. H., Cable, M. D., Cowan, T. E., Estabrook, K. G., Hammel, B. A., Hatchett, S. P., Henry, E. A., Hinkel, D. E., Kilkenny, J. D., Koch, J. A., Kruer, W. L., Langdon, A. B., Lasinski, B. F., Lee, R. W., MacGowan, B. J., MacKinnon, A., Moody, J. D., Moran, M. J., Offenberger, A. A., Pennington, D. M., Perry, M. D., Phillips, T. J., Sangster, T. C., Singh, M. S., Stoyer, M. A., Tabak, M., Tietbohl, G. L., Tsukamoto, M., Wharton, K., and Wilks, S. C. (1998). In: Hot electron production and heating by hot electrons in fast ignitor research volume 5 pp. 1966–1972, Pittsburgh, Pennsylvania (USA): AIP.

[Kidder, 1976] Kidder, R. (1976). Nuclear Fusion 16, 405.

[Kim, 1989] Kim, K. (1989). In: Physics of Particle Accelerators, (Month, M. and Dienes, M., eds) p. 565, AIP New York: AIP.

[Kiselev et al., 2004] Kiselev, S., Pukhov, A., and Kostyukov, I. (2004). Physical Review Letters 93 (13), 135004.

[Kitagawa et al., 1992] Kitagawa, Y., Matsumoto, T., Minamihata, T., Sawai, K., Matsuo, K., Mima, K., Nishihara, K., Azechi, H., Tanaka, K. A., Takabe, H., and Nakai, S. (1992). Physical Review Letters 68 (1), 48–51.

[Kodama et al., 2001] Kodama, R., Norreys, P. A., Mima, K., Dangor, A. E., Evans, R. G., Fujita, H., Kitagawa, Y., Krushelnick, K., Miyakoshi, T., Miyanaga, N., Norimatsu, T., Rose, S. J., Shozaki, T., Shigemori, K., Sunahara, A., Tampo, M., Tanaka, K. A., Toyama, Y., Yamanaka, T., and Zepf, M. (2001). Nature 412 (6849), 798–802.

[Kostyukov et al., 2002] Kostyukov, I. Y., Shvets, G., Fisch, N. J., and Rax, J. M. (2002). Physics of Plasmas 9 (2), 636–648.

[Landau and Lifshits, 1982] Landau, L. and Lifshits, E. (1982). The Classical Theory of Fields. New York: Pergamon, 3rd revised english edition.

[Lawson, 1988] Lawson, J. (1988). The Physics of Charged Particle Beams. London: Oxford University Press.

[Leemans et al., 1997] Leemans, W., Schoenlein, R., Volfbeyn, P., Chin, A., Glover, T., Balling, P., Zolotorev, M., Kim, K.-J., Chattopadhyay, S., and Shank, C. (1997). IEEE Journal of Quantum Electronics 33, 1925.

[Leemans et al., 2002] Leemans, W. P., Catravas, P., Esarey, E., Geddes, C. G. R., Toth, C., Trines, R., Schroeder, C. B., Shadwick, B. A., van Tilborg, J., and Faure, J. (2002). Physical Review Letters 89 (17), 174802.

[Lifshitz and Landau, 1981] Lifshitz, E. and Landau, L. (1981). Quantum Mechanics-Nonrelativistic Theory. New York: Pergamon Press, 3rd edition.

[Lotov, 1998] Lotov, K. V. (1998). Physics of Plasmas 5 (3), 785–791.

[Luchini and Motz, 1990] Luchini, P. and Motz, H. (1990). Undulators and Free-Electron Lasers. Oxford: Clarendon Press.

[Madey, 1979] Madey, J. (1979). Nuovo Cimento 50B, 64.

[Malka and Miquel, 1996] Malka, G. and Miquel, J. L. (1996). Physical Review Letters 77 (1), 75–78.

[Malka et al., 2001] Malka, V., Faure, J., Marques, J. R., Amiranoff, F., Rousseau, J. P., Ranc, S., Chambaret, J. P., Najmudin, Z., Walton, B., Mora, P., and Solodov, A. (2001). Physics of Plasmas 8 (6), 2605–2608.

[Malka et al., 2002] Malka, V., Fritzler, S., Lefebvre, E., Aleonard, M.-M., Burgy, F., Chambaret, J.-P., Chemin, J.-F., Krushelnick, K., Malka, G., Mangles, S. P. D., Najmudin, Z., Pittman, M., Rousseau, J.-P., Scheurer, J.-N., Walton, B., and Dangor, A. E. (2002). Science 298 (5598), 1596–1600.

[Modena et al., 1995] Modena, A., Najmudin, Z., Dangor, A., Clayton, C., Marsh, K., Joshi, C., Malka, V., Darrow, C., Danson, C., Neely, D., and Walsh, F. (1995). Natur 377, 606.

[Moore et al., 1997] Moore, C. I., Ting, A., Krushelnick, K., Esarey, E., Hubbard, R. F., Hafizi, B., Burris, H. R., Manka, C., and Sprangle, P. (1997). Physical Review Letters 79 (20), 3909–3912.

[Morse and Feshbach, 1953] Morse, P. and Feshbach, H. (1953). Methods of Theoretical Physics, volume I. New York: McGraw-Hill Book Company.

[Nikishov and Ritus, 1963] Nikishov, A. and Ritus, V. (1963). Zhurnal Eksperimental'noi i Teoreticheskoi Fiziki 46, 776. Sov. Phys. JETP 19, 529 (1964).

[Norreys et al., 2004] Norreys, P. A., Lancaster, K. L., Murphy, C. D., Habara, H., Karsch, S., Clarke, R. J., Collier, J., Heathcote, R., Hemandez-Gomez, C., Hawkes, S., Neely, D., Hutchinson, M. H. R., Evans, R. G., Borghesi, M., Romagnani, L., Zepf, M., Akli, K., King, J. A., Zhang, B., Freeman, R. R., MacKinnon, A. J., Hatchett, S. P., Patel, P., Snavely, R., Key, M. H., Nikroo, A., Stephens, R., Stoeckl, C., Tanaka, K. A., Norimatsu, T., Toyama, Y., and Kodama, R. (2004). In: Integrated implosion/heating studies for advanced fast ignition volume 11 pp. 2746–2753, Albuquerque, New Mexico (USA): AIP.

[Phuoc et al., 2005] Phuoc, K. T., Burgy, F., Rousseau, J.-P., Malka, V., Rousse, A., Shah, R., Umstadter, D., Pukhov, A., and Kiselev, S. (2005). Physics of Plasmas 12 (2), 023101.

[Pittman et al., 2002] Pittman, M., Rousseau, S. F. J., Notebaert, L., Chambaret, J., and Chériaux, G. (2002). Applied Physics B: Lasers and Optics 74, 529–535.

[Pogorelsky, 1998] Pogorelsky, I. (1998). Nuclear Instruments and Methods in Physics Research 411, 172.

[Pukhov, 1999] Pukhov, A. (1999). Journal of Plasma Physics 61, 425.

[Pukhov, 2003] Pukhov, A. (2003). Reports on Progress in Physics 66, 47.

[Pukhov et al., 2003] Pukhov, A., Kiselev, S., Kostyukov, I., and ter Vehn, J. M. (2003). volume 5228 pp. 345–352, SPIE.

[Pukhov and Meyer-ter-Vehn, 1996] Pukhov, A. and Meyer-ter-Vehn, J. (1996). Physical Review Letters 76 (21), 3975–3978.

[Pukhov and Meyer-ter-Vehn, 2002] Pukhov, A. and Meyer-ter-Vehn, J. (2002). Applied Physics B 74, 355–361.

[Pukhov et al., 1999] Pukhov, A., Sheng, Z.-M., and Meyer-ter-Vehn, J. (1999). Physics of Plasmas 6 (7), 2847–2854.

[Quesnel and Mora, 1998] Quesnel, B. and Mora, P. (1998). Physical Review E (Statistical Physics, Plasmas, Fluids, and Related Interdisciplinary Topics) 58 (3), 3719–3732.

[Rischel et al., 1997] Rischel, C., Rousse, A., Uschmann, I., Albouy, P., Geindre, J., Audebert, P., Gauthier, J., Froster, E., Martin, J., and Antonetti, A. (1997). Nature 390, 490.

[Rosenzweig et al., 1991] Rosenzweig, J. B., Breizman, B., Katsouleas, T., and Su, J. J. (1991). Physical Review A (Atomic, Molecular, and Optical Physics) 44 (10), R6189–R6192.

[Rousse et al., 2004] Rousse, A., Phuoc, K. T., Shah, R., Pukhov, A., Lefebvre, E., Malka, V., Kiselev, S., Burgy, F., Rousseau, J., Umstadter, D., and Hulin, D. (2004). Physical Review Letters 93 (13), 135005.

[Rousse et al., 2001] Rousse, A., Rischel, C., Fourmaux, S., Uschmann, I., Sebban, S., Grillon, G., Balcou, P., Forster, E., Geindre, J., Audebert, P., Gauthier, J., and Hulin, D. (2001). Nature 410 (6824), 65–68.

[Santala et al., 2001] Santala, M. I. K., Najmudin, Z., Clark, E. L., Tatarakis, M., Krushelnick, K., Dangor, A. E., Malka, V., Faure, J., Allott, R., and Clarke, R. J. (2001). Physical Review Letters 86 (7), 1227–1230.

[Santala et al., 2000] Santala, M. I. K., Zepf, M., Watts, I., Beg, F. N., Clark, E., Tatarakis, M., Krushelnick, K., Dangor, A. E., McCanny, T., Spencer, I., Singhal, R. P., Ledingham, K. W. D., Wilks, S. C., Machacek, A. C., Wark, J. S., Allott, R., Clarke, R. J., and Norreys, P. A. (2000). Physical Review Letters 84 (7), 1459–1462.

[Santos et al., 2002] Santos, J. J., Amiranoff, F., Baton, S. D., Gremillet, L., Koenig, M., Martinolli, E., Gloahec, M. R. L., Rousseaux, C., Batani, D., Bernardinello, A., Greison, G., and Hall, T. (2002). Physical Review Letters 89 (2), 025001.

[Schoenlein et al., 2000] Schoenlein, R., Chattopadhyay, S., Chong, H., Glover, T., Heimann, P., Shank, C., Zholents, A., and Zolotorev, M. (2000). Applied Physics B 71, 1.

[Schwinger, 1949] Schwinger, J. (1949). Physical Review 75, 1912.

[Sentoku et al., 2002] Sentoku, Y., Mima, K., Sheng, Z. M., Kaw, P., Nishihara, K., and Nishikawa, K. (2002). Physical Review E (Statistical, Nonlinear, and Soft Matter Physics) 65 (4), 046408.

[Sheng et al., 2000] Sheng, Z.-M., Sentoku, Y., Mima, K., Zhang, J., Yu, W., and Meyer-ter-Vehn, J. (2000). Physical Review Letters 85 (25), 5340–5343.

[Smith, 1959] Smith, R. (1959). Semiconductors. Cambridge: Cambridge University Press.

[Sprangle et al., 1992] Sprangle, P., Esarey, E., Krall, J., and Joyce, G. (1992). Physical Review Letters 69 (15), 2200–2203.

[Sprangle et al., 1990] Sprangle, P., Esarey, E., and Ting, A. (1990). Physical Review A (Atomic, Molecular, and Optical Physics) 41 (8), 4463–4469.

[Strickland and Mourou, 1985] Strickland, D. and Mourou, G. (1985). Optics Communications 56, 219–221.

[Tabak et al., 1994] Tabak, M., Hammer, J., Glinsky, M., Kruer, W., Wilks, S., Woodworth, J., Campbell, E., Perry, M., and Mason, R. (1994). Physics of Plasmas 1, 1626.

[Taguchi et al., 2001] Taguchi, T., Antonsen, T. M., Jr., Liu, C. S., and Mima, K. (2001). Physical Review Letters 86 (22), 5055–5058.

[Tatarakis et al., 1998] Tatarakis, M., Davies, J. R., Lee, P., Norreys, P. A., Kassapakis, N. G., Beg, F. N., Bell, A. R., Haines, M. G., and Dangor, A. E. (1998). Physical Review Letters 81 (5), 999–1002.

[Teng et al., 2003] Teng, H., Zhang, J., Chen, Z. L., Li, Y. T., Li, K., Peng, X. Y., and Ma, J. X. (2003). Physical Review E (Statistical, Nonlinear, and Soft Matter Physics) 67 (2), 026408.

[TESLA, 2001] TESLA (2001). Technical Report DESY 2001-011, ECFA 2001-209 TESLA.

[Teychenne et al., 1993] Teychenne, D., Bonnaud, G., and Bobin, J.-L. (1993). Physical Review E (Statistical Physics, Plasmas, Fluids, and Related Interdisciplinary Topics) 48 (5), R3248–R3251.

[Twiss, 1958] Twiss, R. (1958). Australian Journal of Physics 2, 564.

[Umstadter et al., 1996a] Umstadter, D., Chen, S.-Y., Maksimchuk, A., Mourou, G., and Wagner, R. (1996a). Science 273 (5274), 472–475.

[Umstadter et al., 1996b] Umstadter, D., Kim, J. K., and Dodd, E. (1996b). Physical Review Letters 76 (12), 2073–2076.

[Wang et al., 2002] Wang, S., Clayton, C. E., Blue, B. E., Dodd, E. S., Marsh, K. A., Mori, W. B., Joshi, C., Lee, S., Muggli, P., Katsouleas, T., Decker, F. J., Hogan, M. J., Iverson, R. H., Raimondi, P., Walz, D., Siemann, R., and Assmann, R. (2002). Physical Review Letters 88 (13), 135004.

[Weibel, 1959] Weibel, E. (1959). Physical Review Letters 2, 83.

[Wharton et al., 1998] Wharton, K. B., Hatchett, S. P., Wilks, S. C., Key, M. H., Moody, J. D., Yanovsky, V., Offenberger, A. A., Hammel, B. A., Perry, M. D., and Joshi, C. (1998). Physical Review Letters 81 (4), 822–825.

[Whittum, 1992] Whittum, D. H. (1992). Physics of Fluids B: Plasma Physics 4 (3), 730–739.

[Whittum et al., 1990] Whittum, D. H., Sessler, A. M., and Dawson, J. M. (1990). Physical Review Letters 64 (21), 2511–2514.

[Wilks et al., 1992] Wilks, S. C., Kruer, W. L., Tabak, M., and Langdon, A. B. (1992). Physical Review Letters 69 (9), 1383–1386.

[Winick, 1987] Winick, H. (1987). Scientific American 88, 11.

[Wolfram, 1991] Wolfram, S. (1991). MATHEMATICA. New-York: Addison - Wesley, 2nd edition.

[Zheleznyakov, 1967] Zheleznyakov, V. (1967). Soviet Phys. JETP 24, 381.

[Zheng et al., 2004] Zheng, J., Tanaka, K. A., Sato, T., Yabuuchi, T., Kurahashi, T., Kitagawa, Y., Kodama, R., Norimatsu, T., and Yamanaka, T. (2004). Physical Review Letters 92 (16), 165001.

Acknowledgements

I would like to express the deepest gratitude to my supervisor Prof. Dr. A. Pukhov for his permanent interest and support of my research and for numerous valuable and insightful remarks, to Prof. Dr. K.-H. Spatschek for his wise leadership of Institut für Theoretische Physik I, to Dr. I. Kostyukov for many helpful comments, productive work and useful critiques.

I would like to thank the research group “Computational Plasma Physics” of the University of Düsseldorf for the creative atmosphere. My special thanks to Dr. Serguei Gordienko for interesting philosophic discussions in various areas of knowledge, to Teodora Baeva for enthusiasm and openness for talk. I thank the nearest colleague Dr. Oleg Shorokhov for his patience from my numerous questions and for all his time.

I would like to thank my colleagues from the Institut für Theoretische Physik I of Düsseldorf University: Akad. Direktor Dr. Herbert Wenk for help with computer and administrative problems, Eckhard Zügge for technical support and help with hardware problems, Rosemarie Gerardi and Elvira Gröters for help with organizational problems, Dr. Ernst Wolfgang Laedke, Dr. Jan Alexander Posth, Dr. Sylvie Rijkers Defrasne, Götz Lehmann, Marcus Neuer, Andreas Wingen for friendly work atmosphere. My special thanks to Christoph Karle for wide knowledge in computer systems and for wise way of the solving problems.

I would like to thank my experimentalists colleagues from the Institut für Laser- und Plasmaphysik of Düsseldorf University: Prof. Dr. Oswald Willi, Dr. Jens Osterholz for the interesting discussion and new ideas. My special thanks to Ralph Jung for very friendly communications and for his tendency to perfection in physics.

I would like to thank Dr. Björn Manuel Hegelich and Dr. Stefan Karsch for friendly discussions and enjoyable time.

My special thanks to Dr. Helena Kovilyanskaya for critical discussions, the best English language knowledge and countenance in many different situations. Without this support the work could never be done.

And I thank my parents, who pointed out this way for me.

Erklärung

Mit meiner Unterschrift versichere ich an Eidesstatt, dass ich die vordelegte Dissertation selbst und ohne unerlaubte Hilfe angefertigt habe und dass ich diese in der jetzigen oder einer ähnlichen Form moch keiner anderen Fakultät eingereicht habe. Ich erkläre ferner, dass die Dissertation noch nicht veröffentlicht wurde (Veröffentlichungen nach §4(3) der Promotionsordnung bleiben hiervon ausgenommen).
Der Promotionsordnung ist mir bekannt.

Düsseldorf, im April 2005